BIOPHYSICAL INVESTIGATION OF THE 'IRONOME' OF JURKAT CELLS AND *SACCHAROMYCES CEREVISIAE*

A Dissertation

by

NEMA DEVI JHURRY

Submitted to the Office of Graduate and Professional Studies of
Texas A&M University
in partial fulfillment of the requirements for the degree of

DOCTOR OF PHILOSOPHY

Chair of Committee,	Paul A. Lindahl
Committee Members,	David P. Barondeau
	Michael Polymenis
	Gregory Reinhart
Head of Department,	Gregory Reinhart

December 2013

Major Subject: Biochemistry

ABSTRACT

The speciation of iron in intact Jurkat cells and their isolated mitochondria was assessed using biophysical methods. $[Fe_4S_4]^{2+}$ clusters, low-spin (LS) Fe^{II} heme centers, non-heme high-spin (NHHS) Fe^{II} species, ferritin-like material and Fe^{III} oxyhydroxide nanoparticles were detected, via Mössbauer, in intact Jurkat cells and their isolated mitochondria. EPR spectroscopy was used to quantify Fe-containing species in the respiratory complexes. Contributions from heme *a*, *b* and *c* centers were quantified using electronic absorption spectroscopy. Results were collectively assessed to estimate the first "ironome" profile of a human cell.

The Fe content of Jurkat cells grown on transferrin-bound iron (TBI) and Fe^{III} citrate (FC), and of isolated mitochondria therefrom, was characterized. On average, only 400 ± 100 Fe's loaded per ferritin complex, regardless of the medium Fe concentration. The extent of nanoparticle formation scaled nonlinearly with the concentration of FC in the medium. Nanoparticle formation was not strongly correlated with ROS damage. Cells could utilize nanoparticles Fe, converting them into essential Fe forms. Cells grown on galactose rather than glucose respired faster, grew slower, exhibited more ROS damage, and generally contained more nanoparticles. Cells grown with TBI rather than FC contained lower Fe concentrations, more ferritin and fewer nanoparticles. Frataxin-deficient cells contained more nanoparticles than comparable WT cells. Data were analyzed by a chemically-based mathematical model.

Fermenting *Saccharomyces cerevisiae* cells grown with varying [Fe] were also studied. The high-affinity Fe import pathway was active only in Fe-deficient cells. Whether Fe-deficient cells were grown under fermenting or respirofermenting conditions had no effect on Fe content; such cells prioritized their use of Fe to essential forms devoid of nanoparticles and vacuolar Fe. Fermenting cells grown on Fe-sufficient and Fe-overloaded medium contained 400 – 450 μM Fe. In these cells the concentration of nonmitochondrial NHHS Fe^{II} declined 3-fold, relative to in Fe-deficient cells, whereas the concentration of vacuolar NHHS Fe^{III} increased to a limiting cellular concentration of ~ 300 μM. Isolated mitochondria contained more NHHS Fe^{II} ions and substantial amounts of Fe^{III} nanoparticles. The Fe contents of cells grown with excessive Fe in the medium were similar over a 250-fold change of nutrient Fe levels.

DEDICATION

I dedicate this work to my husband, Tyrone Fernando, who has provided me with great support, love and encouragement at every step in my endeavors as a graduate student, and without whom, I would not have succeeded. I also dedicate this work to my parents Mr. Rajendranath Jhurry, and Mrs. Lilawanee Jhurry, and my sister, Mrs. Sooreshwaree Danny, whose help and support were primordial in my success.

ACKNOWLEDGEMENTS

I am deeply grateful to each and every person who has helped me during my career as a graduate student. First and foremost, my deepest thanks go to my advisor, Dr. Paul A. Lindahl, who has always provided utmost support, optimism, guidance, and encouragement, ensuring successful completion of my research projects. I would also like to thank my committee members: Dr. Gregory Reinhart, Dr. David P. Barondeau, and Dr. Michael Polymenis for their time and valuable advice regarding my research.

I would also like to express my gratitude for all of the former and current members of Dr. Lindahl's lab whose help and input has been crucial for my research, and whose collaborations were essential for completion of my research project: Jessica, Greg, Ren, Allison, Mrinmoy, Sean, Jinkyu, and Mike. I also wish to thank our collaborators, namely Hansoo Kim and E. Ann Ellis for help with microscopy sample preparation and analysis, and Dr. Vishal Gohil for help with running metabolic assays. I also wish to extend a special thanks to the administrative staff of the Department of Biochemistry, namely Pat Swigert, Juanita Withem, Betty Cotton, Deborah Gau, Carren Hopkins, Tillie Rausch, and Daisy Wilbert. I am deeply grateful to Dr. Janet Grimsley for helping me with my initial experiences as a scientist, and Dr. Edward Funkhouser for his recommendation when I was in search of employment.

Finally, I would like to express my deepest gratitude to my parents, my husband, and my friends, for their love, continuous support, and encouragement, without which I would not have succeeded.

TABLE OF CONTENTS

CHAPTER Page

CHAPTER Page

LIST OF FIGURES

FIGURE Page

LIST OF TABLES

CHAPTER I

INTRODUCTION

Iron is an essential transition metal for cellular function and viability of almost all organisms. Iron can assume multiple oxidation states, which makes it ideal for electron transfer processes, and for binding various biological ligands [1]. The most common biological oxidation states of iron are the divalent and trivalent iron (Fe^{2+} and Fe^{3+}), although the tetravalent Fe^{4+} and the pentavalent Fe^{5+} also occur transiently during certain iron-catalyzed redox reactions [1].

Iron participates in cellular functions as various cofactors to proteins and enzymes, most commonly in the form of iron-sulfur (Fe/S) clusters and hemes. Heme iron is essential for numerous biological functions such as oxygen binding and transport (e.g. myoglobin and hemoglobin) [2], inactivation of reactive oxygen species (e.g. catalases and peroxidases) [3, 4], mitochondrial respiration (Complexes II, III and IV, and cytochromes, and Complex I in most organisms) [5-8] . Fe/S clusters are essential prosthetic groups for a number of proteins involved in processes such as glucose metabolism (mitochondrial aconitase) [9]. Other types of iron-containing centers exist, such as the di-nuclear iron center of ribonucleotide reductase [10], and these are also important for cellular function. In mammalian cells, excess iron is normally stored in ferritin as a crystalline ferric oxyhydroxide core [11]. Iron deficiency can be detrimental to cells, leading to cell growth inhibition, and eventually cell death. However, iron

overload can be harmful as well. Iron overload in cells can lead to an increase in ferrous iron, which can participate in Fenton chemistry, resulting in the formation of hydroxyl radicals from hydrogen peroxide, according to the following equation [12]:

$$Fe^{2+} + H_2O_2 \Leftrightarrow Fe^{3+} + HO\bullet + HO^-$$

Furthermore, ferrous iron can reduce molecular oxygen to generate superoxide anions according to the following reaction:

$$Fe^{2+} + O_2 \Leftrightarrow Fe^{3+} + O^-_2\bullet$$

Hydroxyl radicals and superoxide anions are highly damaging to lipids, proteins and nuclei acids [13]. Therefore, the iron status of the cell is tightly controlled via regulation of the expression of proteins involved in iron uptake, efflux, storage, and utilization.

Iron uptake in the majority of mammalian cell types is mediated via the transferrin pathway [14]. Transferrin (Tf) is an 80 kD soluble blood-plasma glycoprotein. At physiological pH, it binds two ferric ions per molecule with high affinity ($K_d \sim 10^{-23}$ M) [14]. However, transferrin is normally only ~30% saturated with iron under physiological conditions. The plasma concentration of diferric transferrin is ~ 5-20 μM (i.e. ~ 10-40 μM transferrin-bound iron, TBI) [1, 15, 16]. The abundance of apo-transferrin in blood plasma provides a buffering effect, whereby sufficient apo-transferrin is available to bind free iron in the event of an increase in plasma iron concentration. This prevents the build-up, in blood plasma, of non-transferrin-bound iron (NTBI), which has been implicated in cellular iron overload and oxidative damage [17].

Diferric transferrin binds to transferrin receptors 1 and 2 (TfR1 and TfR2) [18] located at the cell membrane, which triggers clathrin-mediated endocytosis of the Tf-TfR complex. TfR1, a transmembrane glycoprotein, forms a homodimer of 180 kD. This protein is the major transferrin-receptor utilized by most cells for TBI uptake [19], whereas select cell types, such as liver cells, also express TfR2 [20]. Each receptor can bind up to two diferric transferrin molecules. The endosome containing the transferrin-receptor complex is subsequently acidified via uptake of H^+ through a v-ATPase proton pump located on the endosomal membrane. Endosomal acidification decreases the affinity of transferrin for ferric iron, and causes the release of Fe^{3+} from the transferrin molecules [21]. A ferrireductase (STEAP3) located on the endosomal membrane reduces Fe^{3+} to Fe^{2+}, which is then exported from the endosome via the membrane-bound divalent metal transporter 1, called DMT1 [22]. Fe^{2+} exits into the cytosol and presumably becomes part of the cytosolic labile iron pool. Iron in this pool can be trafficked to various destinations for use, storage, or efflux (in certain cell types) [23]. The endosome containing the apo-transferrin-TfR1 complex is cycled back to the cell membrane, releasing the apo-transferrin into the blood plasma to bind more iron, and making available the transferrin receptors at the cell membrane to bind more diferric transferrin (Figure 1-1) [24].

Iron uptake can also occur through a transferrin-independent pathway, which involves the uptake of non-transferrin-bound iron (NTBI) [25]. Plasma concentrations of NTBI are generally < 1 μM under normal physiological conditions but increases drastically in a variety of iron overload diseases, such as hereditary hemochromatosis

and β-thalassemia [26, 27]. The uptake mechanisms of NTBI are not fully understood, but a number of transport proteins, such as L-type voltage gated calcium channels [28], DMT1 (divalent metal transporter 1) [29], and Zip14 (a zinc transporter protein) [30] have been found to facilitate NTBI uptake. The chemical nature of NTBI is also not well characterized, but ferric citrate is hypothesized to be the major form of NTBI in the blood plasma. Other iron-binding proteins and iron-containing species, such as lipocalin 24p3 [31], serum ferritin [32] and hemes [33], are also possible sources of NTBI that can be taken up by cells. The uptake of NTBI may involve a plasma-membrane bound ferrireductase, such as the duodenal cytochrome b_{561} (DCytb) [34] (Figure 1-2). This enzyme reduces Fe^{3+} to Fe^{2+} before uptake of ferrous iron via a plasma-membrane bound divalent metal transporter such as DMT1. Recent evidence also suggests that extracellular Fe^{3+} can be reduced by ascorbate [35], independent of a ferrireductase. NTBI may also penetrate cells non-specifically via fluid-phase endocytosis or pinocytosis [36]. Iron taken up by mammalian cells presumably enters the cytosol's *labile iron pool* (LIP), which is described as a pool of iron, both Fe^{2+} and Fe^{3+}, bound weakly to low-molecular-weight (LMW) ligands. This pool represents a small percentage of the total cellular iron (3-5%) [37]. The LIP is also known as the *chelatable iron pool* in some literature due to being loosely bound to biological ligands and hence being easily chelated. In addition to being fed with iron via the transferrin pathway, the LIP can also be replenished as a result of degradation of iron-containing proteins. This process occurs primarily in the lysosomes [38].

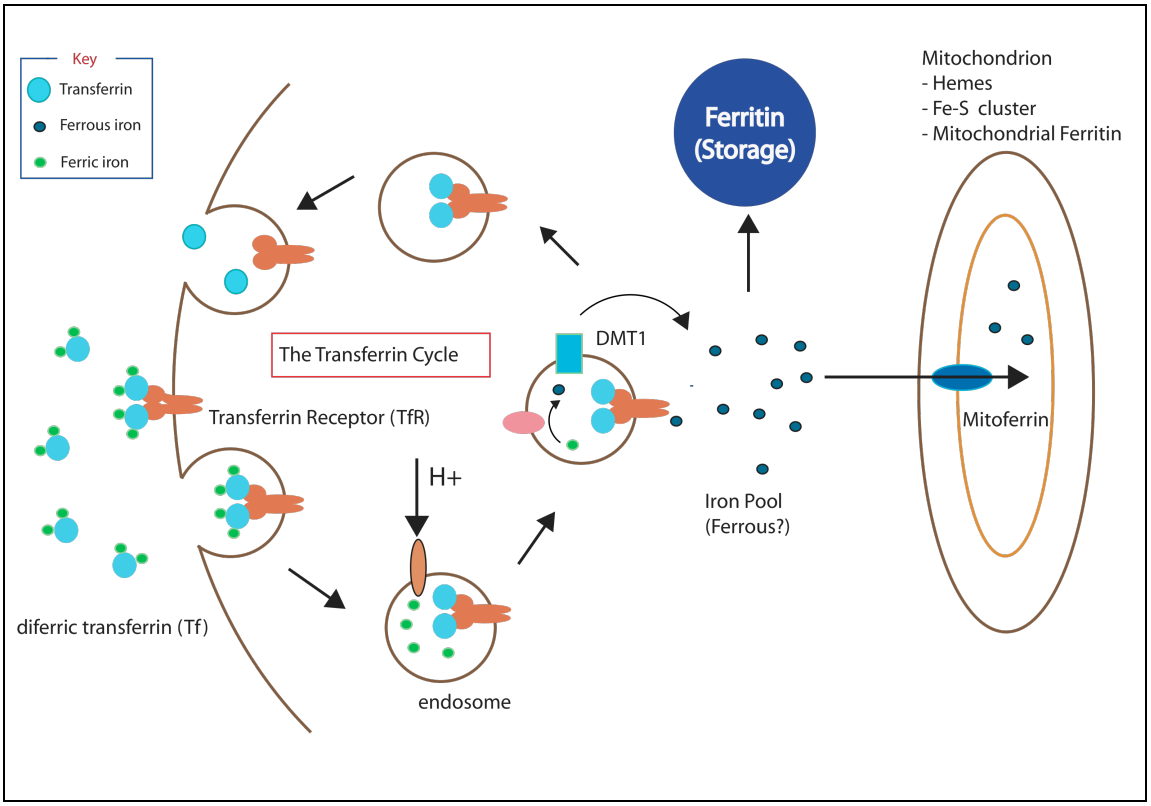

Figure 1-1. Model of the transferrin-dependent iron uptake pathway, and the proposed fate of iron that exits the endosome.

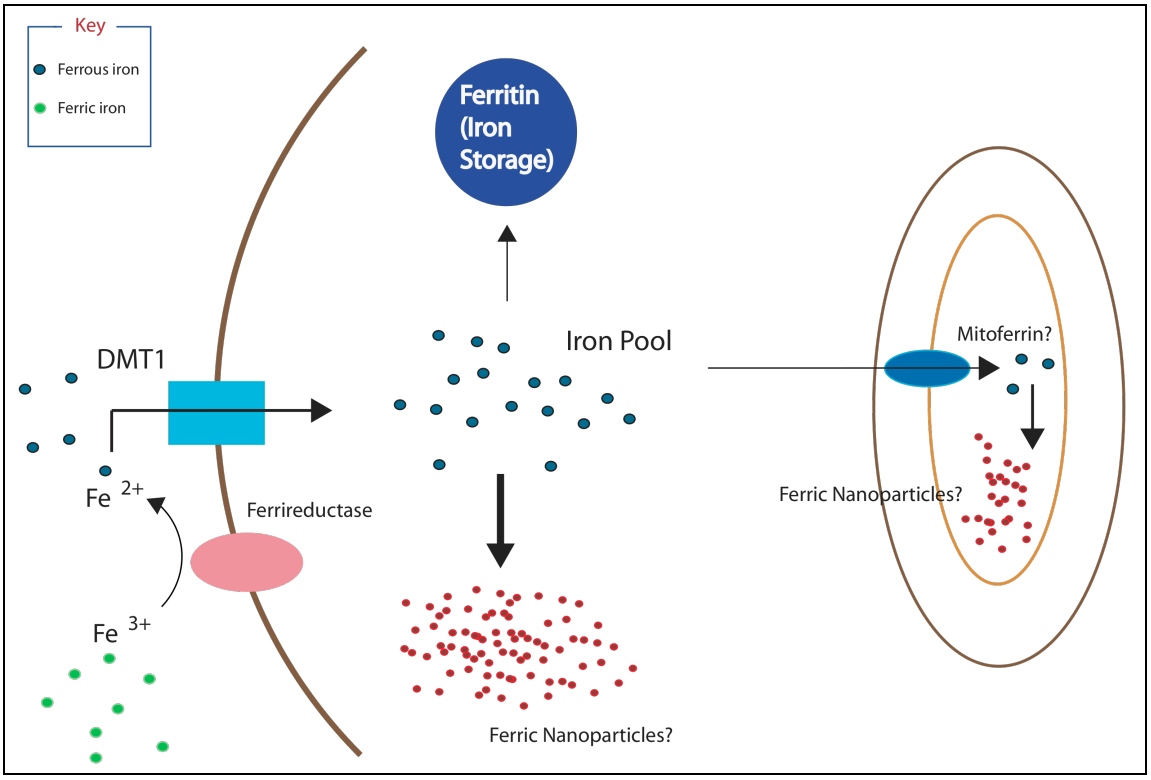

Figure 1-2. Model of the transferrin-independent iron uptake pathway, and the proposed fate of iron that enters the cell as NTBI.

The chemical composition of the cytosolic LIP is not well understood, but the iron is hypothesized to bind LMW organic chelates such as phosphates, citrates, and carboxylates, and ligands such as polypeptides and siderophores [39]. The LIP, being weakly chelated and hence more readily available for redox reactions, is often implicated in the formation of reactive oxygen species (ROS) via Fenton chemistry. The cytosolic LIP is hypothesized to be the major iron feedstock for iron trafficking to other parts of the cell, namely to the mitochondria, and to ferritin for storage when present in excess.

Mitochondria are the 'hub' of cellular iron metabolism, since the majority of iron taken up by the cell is trafficked to mitochondria for Fe/S cluster and heme biosynthesis [40]. The pathway of iron trafficking from the cytosolic LIP to mitochondria is not well characterized. However, the mammalian siderophore 2,5-dihydroxybenzoic acid was recently found to be the iron-binding moiety of lipocalin 24p3, and was implicated as the major siderophore that binds cytosolic labile iron and aids in its trafficking to mitochondria for metabolism [31]. Mitoferrin-1 (Mfrn1) and Mitoferrin-2 (Mfrn2) are the only two iron importers that are known to facilitate iron uptake through the inner mitochondrial membrane [41, 42]. In developing erythroid cells, Mfrn1 is stabilized by ABCB10, a member of the ATP-binding cassette transporter [43]. In spite of being highly homologous, Mfrn1 and Mfrn2 are not functionally redundant, since mitochondrial iron depletion due to knockdown of Mfrn 1 cannot be corrected by ectopic over-expression of Mfrn2 [42].

Apart from Mfrn1 and Mfrn2, other pathways of iron import into mitochondria, although not fully characterized, presumably exist. For example, siderophore-bound

iron uptake supports mitochondrial heme biosynthesis, but a mitochondrial siderophore-iron transporter has yet to be identified [44]. Another model for iron delivery to mitochondria, termed the "kiss-and-run" model, was derived mainly from imaging data and postulates that endosomes containing transferrin-bound iron deliver iron by direct contact with mitochondria, although the mediators of this process are yet to be identified [45].

Mitochondrial iron is utilized for heme and Fe/S cluster biosynthesis, and excess mitochondrial iron is stored in mitochondrial ferritin (mitoferritin, MtFt) [46]. Fe/S clusters are composed of iron and inorganic sulfur and are involved in processes such as electron transport in the respiratory chain complexes, regulatory sensing of iron, and DNA repair [47]. The most common types of Fe/S clusters in mammalian cells are the $[Fe_2S_2]$, $[Fe_3S_4]$, and $[Fe_4S_4]$ clusters. In mammalian cells, Fe/S cluster biogenesis occurs in mitochondria, as well as in the cytosol, and probably also in the nucleus [48].

The first step of Fe/S biogenesis is catalyzed by the multimeric protein complex formed by a dimer of cysteine desulfurase (NFS1) and two monomers of a scaffold protein (ISCU) at either end [49]. Using a pyridoxal phosphate cofactor, NFS1 functions by removing sulfur from cysteine residues and supplying it to the Fe/S biogenesis process [50]. ISCU provides the scaffold and the cysteine ligands upon which biosynthesis of a new Fe/S cluster occurs. Fe/S clusters consist of iron covalently bound to the cysteine ligands, and inorganic sulfur bridging the iron atoms [51].

The source of iron for Fe/S cluster biogenesis is still being debated, although existing evidence indicate that frataxin [52], or a complex of glutathione and glutaredoxin

binding an Fe/S cluster, might be potential iron donors [53]. The role of frataxin is still not elucidated, since reports involving structural modeling of frataxin binding to NFS1 and ISCU suggest that frataxin might be acting as an allosteric switch for Fe/S cluster biosynthesis, rather than an iron donor [54]. Frataxin's newfound role appears to be to bring about conformational change in the NFS1-ISCU complex to enhance Fe/S cluster synthesis. In mammalian cells, NFS1 is stabilized by a small partner protein called ISD11 [55]. The latter has been detected in the mitochondrial matrix, the cytosol, and the nuclei of mammalian cells. Fe/S biogenesis also requires a source of electrons, which are hypothesized to be delivered into Fe/S biogenesis via glutaredoxin 5 (GLRX5) [56] and ferredoxin [57]. After an Fe/S cluster is synthesized on the NFS1-ISCU-ISD11-Frataxin complex, it needs to be transferred to apo-proteins that require Fe/S clusters for their function. Many aspects of this process still need to be elucidated. However, current evidence suggests the participation of a highly conserved chaperone-co-chaperone system, which, in mammalian cells, involves binding of the mammalian co-chaperone HSC20 (heat shock protein) to ISCU [58]. The HSC20-ISCU complex, potentially aided by HSC70, may facilitate the transfer of an Fe/S cluster from ISCU to target apo-proteins [59]. The exact mechanism of selective insertion of Fe/S clusters into target proteins is not known, but is hypothesized to involve interactions between the target apoproteins and the binding surfaces of the chaperone-co-chaperone complex.

For many years, Fe/S cluster biogenesis was thought to occur primarily in mitochondria. In the *Saccharomyces cerevisiae* model, the mitochondrial exporter protein Atm1 was proposed to export either fully formed Fe/S clusters or some form of

sulfur compound for cytosolic Fe/S biogenesis [50]. However, this model has been called into question, as new evidence, albeit controversial, suggests that Fe/S biogenesis systems can be sustained in the cytosol and even in nuclear compartments, independently of the mitochondria. The cysteine desulfurase, NFS1, its binding partner ISD11, the scaffold proteins ISCU and NFU1, as well as the co-chaperone HSC20, are reported to be expressed in small amounts in the cytosolic and/or nuclear compartments [60]. Disruptions in mitochondrial Fe/S biogenesis have been repeatedly associated with mitochondrial iron overload and cytosolic iron depletion in mammalian cells.

Mitochondrial iron is also utilized for heme biosynthesis, a pathway that is significantly better characterized than the Fe/S biosynthesis pathway. Hemes are structurally defined as tetrapyrroles with an iron atom coordinated within, which imparts hemes with the ability to act as electron carrier and a catalyst for redox reactions [61]. The first step, which is also the rate-limiting step, in the heme biosynthesis pathway is catalyzed by an enzyme called ALA synthase. This enzyme carries out the condensation reaction between glycine and succinyl-CoA to form 5-aminolevulinic acid (ALA) [62]. ALA then exits the mitochondria via an unknown mitochondrial transporter, and subsequent steps of heme biosynthesis occur in the cytosol. The cytosolic enzyme aminolevulinate dehydratase (ALAD) catalyzes the condensation of two molecules of ALA into the monopyrrole porphobilinogen [63]. The formation of a tetrapyrrole of porphobilinogen, an unstable molecule called hydroxymethylbilane (HMB), is then catalyzed by porphobilinogen deaminase (PBGD) [64]. HMB subsequently serves as the substrate for the enzyme uroporphyrinogen III synthase (URO3S), which converts HMB

to uroporphyrinogen III (URO'GEN III), resulting in the closure of the tetrapyrrole [65]. URO'GEN III is then converted to coproporphyrinogen III (COPRO'GEN III) by the enzyme uroporphyrinogen decarboxylase (UROD), which catalyzes the removal of the carboxyl groups of the acetic acid side chains [66]. Sequential decarboxylation of the propionate groups of pyrrole rings A and B of COPRO'GEN III to vinyl groups by the enzyme coproporphyrinogen oxidase (CPO) follows, giving rise to protoporphyrinogen IX (PROTO'GEN IX) [67]. This process takes place in the intermembrane space of the mitochondria. The enzyme protoporphyrinogen oxidase (PPO) then oxidizes PROTO'GEN IX to protoporphyrin IX [68]. The final step in heme biosynthesis involves the insertion of iron into protoporphyrin IX by the enzyme ferrochelatase, and occurs on the inner surface of the inner mitochondrial membrane [69].

Excess iron that is not utilized for Fe/S cluster or heme biosynthesis is stored in the cytosolic iron storage protein ferritin. In some cell types, iron can also be exported through the membrane-bound iron exporter, ferroportin [70]. Mammalian cytosolic ferritin is composed of a protein shell made of two functionally and genetically distinct subunit types: H-chain (heavy chain, ~ 21 kD) and L-chain (light chain, ~ 19 kD). These subunits assemble in varying ratios depending on the cell type [11]. Mitochondrial ferritin, on the other hand, consists of 100% H-subunits, irrespective of cell type [46].

The dinuclear iron catalytic center, where the oxidation of Fe^{II} to Fe^{III} takes place in the presence of molecular oxygen or hydrogen peroxide, is present on the H-subunit. The L-subunit is believed to enhance the nucleation of the iron core, hence the more L-subunits present in ferritin, the greater its ability to store iron [71]. The H/L subunit ratio

varies according to tissue type. For example, up to 70% H-subunits may be present in ferritins of tissues such as the heart and the brain, which exhibit high ferroxidase activity, whereas ferritins in tissues involved mainly in iron storage, such as the liver and the spleen, exhibit up to 90% L-subunits [11]. Mitochondrial ferritin, unlike cytosolic ferritin, consists only of H-subunits [72]. Mammalian cytosolic ferritins can store up to 4500 iron atoms in their core in the form of a crystalline mineral ferrihydrite [73].

The mechanisms of iron oxidation and mineralization in ferritins have been studied for more than 30 years. The prevalently accepted mechanism involves binding of Fe^{II} at the H-subunit catalytic sites, oxidation to Fe^{III}, and displacement of the ferric ions into the protein cavity, leading to the formation of a stable nucleation point for formation of mineral ferrihydrite [74]. Recently, poly(rC) binding protein, PCBP1 was discovered to act as an iron-chaperone, aiding the delivery of cytosolic iron to ferritin [75].

Mammalian ferritin can also act as a source of iron during iron depletion of the cell. The mechanism of iron release from ferritin is not well understood, although certain processes, such as ferritin proteolysis in lysosomes, or reductive release of iron from the ferritin core, have been proposed [76]. Incomplete degradation of ferritin in lysosomes is believed to lead to the formation of hemosiderin [77].

Many of the proteins involved in cellular iron homeostasis (import, sequestration, utilization and export) are themselves regulated by the cellular iron concentration. The mRNAs of these proteins contain an iron-responsive element (IRE) in either their 5' or their 3'-untranslated region (5'-UTR or 3'-UTR) [78]. IREs are heterogenous sequences of 28-30 nucleotides that form stem-loop structures that can be recognized by the iron-

regulatory proteins (IRPs). Iron-regulatory proteins 1 and 2 (IRP1 and IRP2) are highly homologous proteins that possess ~64% sequence identity in human cells [79]. They bind to the IREs of transcripts to regulate protein translation in response to the iron status of the cell. IRP1 is a $[Fe_4S_4]$-binding protein that acts as cytosolic aconitase when iron is abundant, but loses its Fe/S cluster and functions as iron-regulatory protein when iron is scarce [80]. Recent evidence suggests, however, that iron deficiency alone could not be responsible for loss of Fe/S cluster by cytosolic aconitase, and that iron sensing by IRP1 may also require the action of reactive nitrogen species (RNS) and ROS such as nitroxide (NO), superoxide (O^-_2•), or hydrogen peroxide (H_2O_2) [81, 82]. RNS and ROS were found to lead to the activation of cytosolic aconitase into the RNA-binding IRP1 form. S138 phosphorylation of IRP1 by protein kinase C was also found to lead to accumulation of the RNA-binding form of IRP1 [83]. IRP2, on the other hand, is stabilized and functions in post-transcriptional regulation during iron-depleted conditions. This protein is targeted for degradation by the ubiquitin-proteasome pathway when cells are iron replete. Recently, an E3 ubiquitin ligase, FBXL5, was found to ubiquitinate IRP2, and target it for degradation under iron replete conditions [84, 85]. FXBL5 itself contains a hemerythrin domain that binds 2 iron atoms (yielding a di-iron center) under iron replete conditions, and thus, is stabilized by oxygen and iron abundance [86]. Interestingly, IRP1 was also found to be a substrate of FBXL5. When IRPs are stabilized during iron scarcity, they can stabilize mRNAs of some proteins by binding with high affinity to the 3'-UTR (e.g. mRNA of TfR1 or DMT1). They can also destabilize the mRNAs of other proteins by binding to the 5'-UTR (e.g. mRNA of

ferroportin or H- and L-chains of ferritin) [87]. Other proteins that have IREs in their transcripts include erythroid δ-aminolevulinic acid synthase (eALAS) and mitochondrial aconitase (mAcon). IRPs bind IREs of different transcripts with affinities varying over a 9-fold range [79]. For example, IRP2 has higher affinity for ferritin H- and L-chain IREs than for mAcon IRE, rendering the regulation of ferritin more sensitive than mAcon to variations in intracellular iron concentration [88].

Recently, a secondary pathway, independent of the IRP pathways, and involving the mammalian target of rapamycin (mTOR) protein, was found to regulate iron homeostasis in cells. Tristetraprolin (TTP), a protein formally known to be involved in anti-inflammatory response, was discovered to be the downstream target of mTOR. TTP was found to bind to the mRNAs of transferrin receptor 1 and ferroportin and enhance their degradation. mTOR regulates TTP expression, thus altering cellular iron flux through modulation of iron transporters. The mTOR pathway is believed to act more by fine-tuning cellular iron utilization to satisfy the metabolic needs of the cell, since the changes in iron levels in cells were modest when mTOR was targeted [89].

Excess cellular iron is exported from cells via the only known membrane-bound iron exporter, ferroportin (Fpn) [70]. Lack of Fpn results in cellular iron accumulation in cell types that are known to express Fpn and export iron [90]. Iron taken up by enterocytes enters the blood stream through Fpn-mediated export. Fpn present in macrophages is involved in iron export into the bloodstream following recycling of iron from senescent red blood cells [91]. Fpn has 9-12 transmembrane domains, and its oligomerization state is still under debate, with some studies portraying Fpn as a monomer and others as a dimer.

The preponderance of the evidence would seem to favor the model of Fpn as a dimer [92-94]. The mechanism of Fpn-mediated iron export is still obscure, although the fact that iron transport is dependent on an extracellular ferroxidase (such as ceruplasmin or hephaestin) suggests that the Fe^{II} state is the substrate for Fpn [95].

Diseases of iron metabolism encompass both iron deficiency and iron overload, exemplifying the two-faced nature of iron in human health. Systemic iron deficiency results in anemia, which affects approximately 2 billion people worldwide [96]. The most common forms of anemia include iron-deficiency anemia (IDA) [97], anemia of chronic disease (ACD) [98], and iron-refractory iron-deficiency anemia (IRIDA) [99]. IDA normally occurs due to nutritional iron deficiency, leading to hypochromic and microcytic anemia. ACD tends to occur in hospitalized patients suffering from conditions that cause chronic activation of the immune system. IRIDA appears to be genetically linked, leading to increased levels of hepcidin, a peptide that regulates systemic iron homeostasis by causing degradation of ferroportin, which prevents iron from entering the bloodstream.

Iron overload diseases are characterized by excessive iron accumulation in different tissues and organs, which is harmful because of iron's tendency to participate in redox reactions leading to the formation of damaging ROS. Two typical iron overload diseases, such as hereditary hemochromatosis and β-thalassemia, are characterized by an increase in non-transferrin-bound iron in the blood plasma [26, 27]. These diseases are also accompanied by an increase in plasma malondialdehyde, and a decrease in α-tocopherol, signatures of oxidative stress [100, 101]. NTBI may appear in the bloodstream even if plasma transferrin is not fully saturated. Hereditary hemochromatosis is typified by

excessive iron accumulation in the liver, heart, pancreas, parathyroid and pituitary glands [102]. β-thalassemia is a secondary iron overload disease, characterized by excessive α-globin production. This leads to α-globin precipitation in red blood cells, ineffective erythropoiesis, and iron overload [103]. Other forms of iron overload diseases, such as Friedreich's ataxia and X-linked sideroblastic anemia, involve disruption in mitochondria proteins involved in iron metabolism. Friedreich's ataxia is a result of frataxin deficiency, leading to defective Fe/S cluster biosynthesis. X-linked sideroblastic anemia is a result of ABCB7 deficiency, an inner mitochondrial membrane-bound transporter possibly involved in the export of an unknown molecule necessary for iron homeostasis in cells [104, 105].

Iron exists as various species in the mammalian cell. A comprehensive understanding of the fate of iron in healthy and diseased states requires the ability to probe the iron speciation and distribution in cells with minimal disturbance to the equilibria that exist between different iron-containing species inside the cell. Previous methods involving cellular and/or organellar sub-fractionation [106-108], and use of fluorescent Fe chelator in intact cells [109-111], have mainly been designed to probe the labile iron pool (also functionally defined as the *chelatable* iron pool) in various cell types and their organelles. Cellular and/or organellar subfractionation usually requires separation of cellular components into several fractions and quantification of iron content of each fraction. This method has been used primarily to probe the elusive labile iron pool(s) of cells, in an attempt to quantify them. The main problem with this method is its disruptive nature, which inevitably leads to decompartmentalization of cellular

iron, and a shift in oxidation state of the Fe during fractionation, resulting in inaccurate quantification of iron-containing species and large variations from study to study [112]. More recently, studies have used fluorescent chelators to selectively probe the *chelatable* iron pool inside intact cells. This minimizes the invasiveness of the experiment, and requires small sample volumes. However, the specificity of the chelators again disallows the comprehensive speciation of all iron present in the cells, and their affinities for Fe may still lead to shifts in the equilibria of iron-containing species. These problems can be avoided by adopting biophysical and spectroscopic techniques performed on intact whole cells, or isolated organelles. Recently, laser ablation inductively coupled plasma mass spectrometry (LA-ICP-MS) has been successfully used as a powerful, highly sensitive tool for probing the distributions of metals and non-metal species within biological samples [113, 114].

Our approach to probing the iron distribution in cells and organelles relies on the use of biophysical methods, namely Mössbauer spectroscopy, Electron Paramagnetic Resonance spectroscopy (EPR), and Electron Absorption Spectroscopy (UV-Vis). Mössbauer spectroscopy is based on the recoil-free, resonant absorption and emission of gamma rays in solids, as described by Rudolf Mössbauer in 1957 [115]. Mössbauer spectroscopy is similar, in principle, to Nuclear Magnetic Resonance spectroscopy (NMR), since both techniques probe transitions in the nuclear spin of the sample. Mössbauer spectroscopy may alternatively be called Nuclear Gamma Ray Resonance spectroscopy, since it is used to probe nuclear transitions from a ground state to an excited state that require a substantial amount of energy, which can only originate from a

gamma ray source. Mössbauer spectroscopy is limited by the need for a suitable gamma-ray source, which means that it can only be presently used to detect ^{57}Fe in samples, since ^{57}Fe absorbs the gamma-ray, of energy 14.4 keV, emitted by ^{57}Co. Mössbauer spectroscopy measures the nuclear transitions of ^{57}Fe from a ground spin state I = ½ to the excited spin state I = 3/2. The energy of the gamma rays incident upon the sample is modulated by moving the ^{57}Co back and forth, resulting in the Doppler Effect of the energy observed by the sample.

The major parameters of a Mössbauer spectrum, namely the isomer shift, the quadrupole splitting, and the magnetic hyperfine interactions, can provide detailed information regarding the iron oxidation states, the spin states (low-spin or high-spin), and the nature of the ligand environments around the iron centers. No ^{57}Fe is Mössbauer silent, and spectral intensities are proportional to the amount of iron containing species detected, since the extinction coefficient for every species is the same, making Mössbauer spectroscopy one of the most powerful tools to probe iron distribution and speciation in a sample. Furthermore, the disruption of biological samples is not required, and they are frozen to very low temperatures during analysis (4-70K), which eliminates the possibility of alterations in the chemical properties or equilibria of the iron-containing species in the sample. The main drawback of Mössbauer spectroscopy is its insensitivity (detection limit ~ 50 μM ^{57}Fe), which means that biological samples need to be scaled up and enriched with the expensive ^{57}Fe isotope, which is only 2.2% abundant in nature. Mössbauer analysis of biological samples containing low concentrations of ^{57}Fe require several hours of running time, and can last for up to two

weeks, which makes Mössbauer spectroscopy a very time-consuming technique. Our lab has successfully exploited Mössbauer spectroscopy to probe the iron distribution of yeast cells, and isolated yeast organelles, such as mitochondria and vacuoles [116-120].

Electron Paramagnetic Resonance is the next most powerful biophysical technique available at our hands to characterize iron-containing species [121]. EPR spectroscopy has a much lower detection limit than Mössbauer spectroscopy (~0.1 μM). It is commonly used complementarily with Mössbauer spectroscopy to probe paramagnetic Fe-containing species. As its name suggests, EPR spectroscopy is not specific to iron and can probe transitions in unpaired electrons from any species in the presence of an externally applied magnetic field. Similarly to Mössbauer spectroscopy, EPR can be used on intact cellular or organellar samples, and also provide information about the redox state, the spin state and the ligand environment of the species being studied. The main limitation of EPR is that species that do not have unpaired electrons are EPR silent. However, these species, if present in large enough concentrations, can be detected via Mössbauer spectroscopy.

Energy-dispersive X-Ray Imaging (EDX), combined with Scanning Transmission Electron Microscopy (STEM), is a powerful tool in direct visualization of iron accumulated in biological samples [122]. EDX consists of bombarding the biological specimen with high-energy electrons and detecting the characteristic X-rays produced, via use of an energy-dispersive spectrometer. The X-rays produced are indicative of the element (s) present in the sample. When combined with STEM, EDX imaging can provide a high-resolution elemental map of a biological specimen being studied,

relatively rapidly. Furthermore, overlaying elemental maps can provide information about which elements follow the same map patterns, and hence provide insight regarding the elements associated with accumulated iron in our samples. This can confirm the nature of the ligands associated with accumulated iron in biological samples. The main disadvantage of this technique is that it has a high detection limit, and hence requires significant accumulation of iron in biological samples to be detectable.

Other analytical techniques, such as Electron Absorption Spectroscopy (a.k.a UV-Vis spectroscopy) and Inductively-Coupled Plasma Mass Spectrometry (ICP-MS) are used complementarily with the biophysical methods. UV-Vis spectroscopy is used to detect the levels of reduced hemes in samples, and can resolve hemes *a*, *b* and *c* [123]. ICP-MS provides us with concentrations of metal ions in our samples, and can distinguish between ^{57}Fe and ^{56}Fe, thus providing information about the percent enrichment of the samples with ^{57}Fe. Total Fe concentrations, in combination with percentages of various species detected via Mössbauer spectroscopy, can provide us with 'absolute' concentration values for each Mössbauer species observed in the sample.

Transmission Electron Microscopy is used mainly to determine the purity and integrity of isolated mitochondria, to make sure that the isolated organelles are mostly intact after isolation. Molecular biology techniques, such as Western Blotting, and mammalian cell genetics are also employed in our attempts to better understand the 'ironome' of the human cell. Western blotting is used mainly to monitor the purity of the isolated mitochondria in the final mitochondrial fraction, and to determine protein levels relative to normal cells, when proteins are either over-expressed or knocked-

down. Changing the levels of proteins of interest allows us to determine how the 'ironome' of the cell and the isolated mitochondria is perturbed.

As described in this dissertation, the objective of my research has been to use the biophysical, bioanalytical and molecular biology techniques available to probe the iron distribution and speciation in the human cell and isolated mitochondria. Our initial Mössbauer studies revealed the presence of ferric nanoparticles in whole cells and isolated mitochondria of cells grown on 10 μM ferric citrate [124]. We then probed various grown conditions, such as iron source and concentration, as well as carbon source, to determine the effect on the formation of the ferric nanoparticles in the cells and isolated mitochondria. We found that cells are most prone to formation of ferric nanoparticles when grown with non-transferrin-bound iron, or when grown on galactose instead of glucose. We studied the nature of the ferric nanoparticles further using STEM combined with EDX imaging, and found them to be associated with phosphorus, suggesting that they may be chemically similar to ferric phosphate nanoparticles found to accumulate in yeast cells depleted in proteins involved in iron metabolism and homeostasis. Our work provides insight into the phenomenon of iron accumulation in human cells in iron overload diseases.

CHAPTER II

BIOPHYSICAL INVESTIGATION OF THE IRONOME OF HUMAN JURKAT CELLS AND ISOLATED MITOCHONDRIA

Introduction

Iron is an essential component of human cellular metabolism, due to its impressive redox, catalytic and substrate-binding abilities [125]. A comprehensive molecular-level understanding of cellular iron metabolism will require an understanding of individual Fe-containing proteins in the cell, but it will also require a systems-level understanding of iron trafficking and regulation. Connecting these two levels, the focus of this study, will be especially challenging.

Much is known of individual iron-containing proteins (though much also remains to be determined). One of the two pathways known to import Fe into the cell [24] involves transferrin (Tf), a blood plasma protein that binds Fe^{III} ions reversibly [14]. The binding of Tf to its receptor on the plasma membrane stimulates endocytosis. The resulting endosome is acidified, promoting the release of iron from Tf and reduction to the Fe^{II}

---

*This chapter is reproduced with permission from: "Biophysical Investigation of Ironome of Human Jurkat Cells and Mitochondria" by Nema. D. Jhurry, Mrinmoy Chakrabarti, Sean P. McCormick, Gregory P. Holmes-Hampton, and Paul A. Lindahl, 2012, *Biochemistry*, 51, 5276-5284.

state [126]. Fe^{II} ions are pumped into the cytosol where they are either incorporated into iron-dependent apo-proteins or trafficked into other cellular compartments. Fe^{III} citrate is taken up by a transferrin-independent pathway [127]. A cell-surface ferrireductase reduces Fe^{III} to Fe^{II} prior to uptake [128].

Mitochondria are "traffic hubs" in the cell, as they account for 20-30% of cellular iron [129]. Cytosolic Fe enters mitochondria via mitoferrins [41] and perhaps other transporters. Mitochondria may also import Fe by direct contact with transferrin-containing endosomes [45] and/or *via* the siderophore 2,5-dihydroxybenzoic acid [44]. Most cellular Fe/S clusters and all heme prosthetic groups are biosynthesized in mitochondria. The final step of heme biosynthesis, inserting Fe^{II} into protoporphyrin IX, occurs in the mitochondria [61].

The Fe used to build Fe/S clusters in the mitochondria is transferred onto Fe/S scaffold proteins in the matrix [130]. These clusters are inserted into various recipient apo-proteins including respiratory complexes RCI – RCIV [131]. RCI contains 2 $[Fe_2S_2]$ clusters and 6 $[Fe_4S_4]$ clusters [5]. RCII, a.k.a. succinate dehydrogenase, contains a low-spin (LS) heme *b* as well as $[Fe_2S_2]$, $[Fe_4S_4]$ and $[Fe_3S_4]$ clusters [6]. RCIII, a.k.a. cytochrome bc_1, contains a $[Fe_2S_2]$ Rieske cluster, one heme *c* and two heme *b* centers [7]. Cytochrome *c* contains a LS heme *c* center, while RCIV, a.k.a. cytochrome *c* oxidase, harbors a di-copper center (Cu_A), a heme *a* center, and an active-site heme a_3 center interfaced to the Cu_B center [132].

Ferritin is a cytosolic Fe storage protein that mobilizes Fe under iron-depleted conditions. It stores Fe as an insoluble magnetically-interacting ferrihydrite, which

prevents Fe from participating in Fenton chemistry ($Fe^{II} + H_2O_2 \Leftrightarrow Fe^{III} + OH^- + \cdot OH$) [11]. Ferritin can store up to ~4500 iron atoms in its inner core, estimated to correspond to 60% to 88% of total cellular iron [133]. Mössbauer spectra of ferritin at low temperatures (4.2 K) exhibit a broad sextet pattern similar to mononuclear high-spin (HS) Fe^{III} complexes. At ~ 70 K and higher, the sextet collapses into a broad quadrupole doublet with Mössbauer parameters of a superparamagnetic Fe^{III} species [134]. Unlike mononuclear HS Fe^{III} species, ferritin is EPR-silent at low temperatures and gives rise to a broad EPR signal in the g = 2 region as temperatures are raised above 50 K [135].

A proportion of cellular iron has been hypothesized to be loosely coordinated and to function either as feedstock for the biosynthesis of Fe centers or as trafficking species that can be imported into organelles. These forms of Fe are collectively referred to as the *Labile Iron Pool* (LIP). There is substantial, albeit circumstantial, evidence for an LIP in the cytosol and mitochondrial matrix [136]. The mitochondrial LIP may be used for Fe-S cluster and heme biosynthesis, whereas the cytosolic LIP may report on the Fe status of the cell and be imported into various organelles [112]. The LIP may also participate in Fenton chemistry and thus generate ROS. Aging and various neurodegenerative diseases such as Alzheimer's and Parkinson's are exacerbated by oxidative stress [112].

In this study, we evaluated the ironome of whole human Jurkat cells and their mitochondria from a systems-level perspective using a biophysical approach centered on Mössbauer spectroscopy. Our results indicate that ferritin and mitochondrial Fe are indeed dominant players in cellular Fe metabolism. Also significant are nonheme HS Fe^{II} species, which are present at concentrations exceeding previous estimates, and Fe^{III}

oxyhydroxo nanoparticles which were found in both isolated mitochondria and whole cells. These results allow an estimate of the overall distribution and speciation of iron in a human cell.

Experimental Procedures

Bioreactor Design

We adopted the design for a Chemglass 7 L bioreactor (Catalogue # CLS-1384-01) and modified the design into a 25-L water-jacketed, all-glass bioreactor for these studies (Figure 2-1). The 12" diameter stainless-steel lid plate had 4 evenly spaced 1" ID ports with screw tops surrounding a central stir-motor connection. Two 1" × 3" and two 1" × 30" Teflon rods were inserted into the ports. The long rods were used to add media, harvest cells, and bubble gases through the culture. The short rods were used to deliver gases to the headspace and exhaust gases. A small hole was drilled into the short Teflon rod used to exhaust gases, through which a thin tube connected to a syringe was threaded. This tube was used to remove small samples of culture for cell count and to assess viability. A rounded-rectangular (3" × 24") Teflon paddlewheel was attached to the underside of the lid, and a stir-motor (Arrow Engineering Co., Inc model 350) rotated it at ~ 60 rpm. The bioreactor was autoclaved for 3 hours before use, with Aervent filters (Millipore) on all openings, and allowed to cool down to room temperature before inoculation. The bioreactor was wrapped with a black cloth during cell growth to prevent photo-induced degradation of media components.

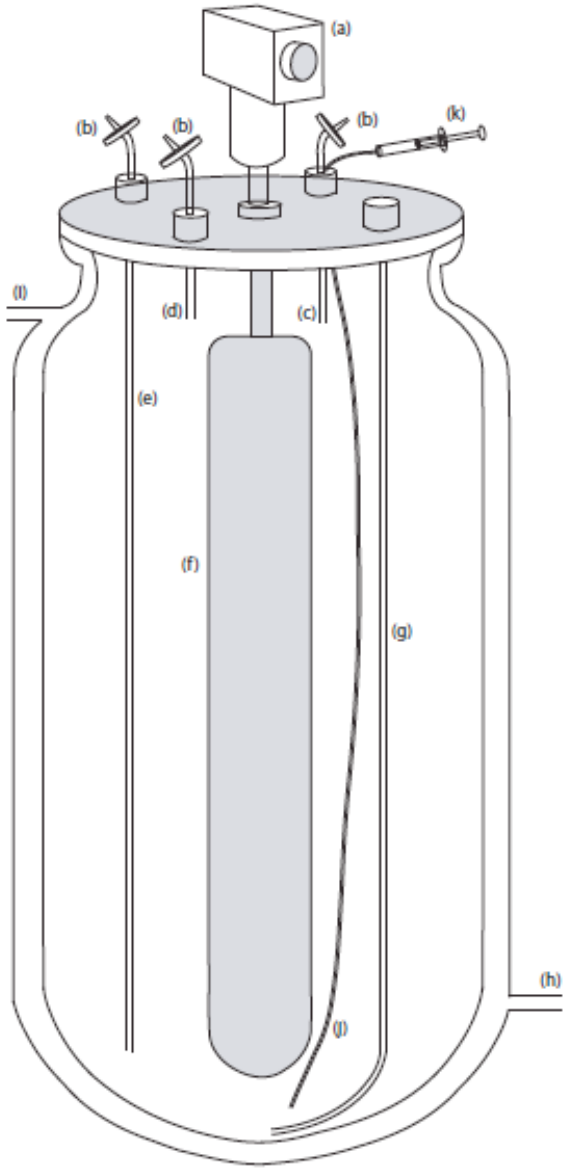

Figure 2-1. Design of the bioreactor. (a) motor to rotate impeller, (b) 0.2 micron Aervent filters, (c) tube for exhaust gases, (d) tube for gas delivery to headspace, (e) tube for sparging gas mixture into media, (f) flat impeller, (g) tube for loading/ unloading of media/cell culture into/out of bioreactor, (h) water inlet (i) water outlet, (j) thin tube to sample bioreactor culture for cell count, and (k) 1 mL sterile syringe.

Human Cell Culture

Starter cell cultures were grown in a CO_2 incubator (Nuaire, Model NU-5500), starting from a 100 mL culture, which was scaled up to 1 L once growth was evident. When the 1 L culture reached a density of ~3 $\times 10^6$ cells/mL (the maximum density), it was used to inoculate 2 L of medium in the bioreactor. T-REx Jurkat cells (Invitrogen, R72207) were grown in the bioreactor under an atmosphere of 75% N_2, 20% O_2, and 5% CO_2 as established with a high-precision gas mixer (MG Industries). All gases were 99.9% pure (certified grade) and were delivered to the culture medium at a combined flow rate of ~ 3 mL/min. Temperature was maintained at 37° C by circulating water through the jacket of the bioreactor (Chemglass). Additional medium was added when cells reached maximum density. When the culture volume was < 10 L, gases were delivered to the headspace *above* the liquid; when the volume was > 10 L, gases were bubbled *through* the liquid. Cells in all culture volumes were grown in RPMI 1640 medium (Sigma Aldrich) supplemented with 5% Newborn Calf Serum (Invitrogen) and an antimycotic-antibiotic cocktail (Invitrogen) to give final concentrations of 100 units/L penicillin, 100 μg/L streptomycin, 0.25 μg/L amphotericin B, and 10 μM ^{56}Fe or $^{57}Fe^{III}$ citrate. Pluronic F-68 (Sigma Aldrich) was added to a final concentration of 0.05% w/v to prevent hydrodynamic damage to the cells. Samples were removed daily and inspected by phase-contrast microscopy for viability and contamination, using 0.4% Trypan Blue solution. Cells were harvested when the cells reached maximum density. Cells were removed from the bioreactor using a peristaltic pump and centrifuged at 800×g for 10 min (Beckman Coulter Avanti J-26 XP centrifuge, JLA 8.1 rotor).

Whole Cell Mössbauer and EPR Sample Preparation

EPR and Mössbauer samples of cells were prepared from 1 to 3 L of cultures that had reached maximum density. Cells were washed with phosphate-buffered saline (PBS, pH 7.4) containing 1 mM EGTA, followed by another wash with EGTA-free PBS buffer. Cells were then packed into 3 mL Mössbauer cups or 4 mm OD quartz EPR tubes by centrifugation at 800×g for 1 hr. The supernatant was removed and samples were frozen in liquid N_2 aerobically.

Mitochondria Isolation

Pellets of freshly harvested cells (wet weight 50-60 g) from 24 L of culture were washed twice with PBS buffer (pH 7.4). Pelleted cells were re-suspended in ~ 500 mL of degassed Mitochondria Isolation Buffer (MIB: 225 mM D-mannitol, 75 mM sucrose, 5 mM HEPES, 1 mM EGTA and 1 mM PMSF, pH 7.4) to a cell density of ~2 x 10^7 cells/mL. From this point onwards, all manipulations were conducted anaerobically, mostly in an Ar-atmosphere MBraun Labmaster glove box containing less than 5 ppm O_2 as monitored by a Teledyne O_2 analyzer (Model 310). For centrifugation steps, samples were sealed in airtight centrifuge bottles inside the glove box before removing for centrifugation; afterwards, they were returned to the box before being opened for further manipulations. Cells were disrupted anaerobically by nitrogen cavitation at 800 psi for 30-40 min, using a disruption vessel (Model 4635, Parr Instruments). The cavitation extract was centrifuged at 800×g for 10 min and the pellet was discarded. The supernatant was centrifuged again at 9000×g for 30 min using a Sorvall Evolution

centrifuge with SLA-1500 rotor. The resulting pellet, which contained crude mitochondria, was re-suspended in ~ 2 mL of MIB buffer, layered over a discontinuous gradient of 7.5 mL of 6% Percoll/3 mL of 17% Histodenz/3 mL of 35% Histodenz in MIB as described [137] and centrifuged at 45,000×g for 1 hr using a Beckman Coulter Optima L-90K ultracentrifuge with a SW 32 Ti swinging-bucket rotor. Mitochondria were collected from the 17-35% Histodenz interface and washed once with MIB. Mitochondria were then packed into Mössbauer cups by centrifugation in the ultracentrifuge (SW 32 Ti rotor) at 10,000×g for 1 hr. The supernatant was removed and the mitochondrial samples were frozen and stored in liquid N_2.

Protein Concentrations

Protein concentrations were determined using a BCA Protein Assay kit (Thermo Scientific Pierce Protein Research Products) as per manufacturer's instructions. Bovine serum albumin (BSA) was used to generate a standard curve (0-2 mg/mL). Absorbances were measured at 562 nm.

Biophysical Studies

EPR spectra of whole cells and isolated mitochondria were collected on an X-band EMX spectrometer (Bruker Biospin Corp., Billerica, MA) equipped with an Oxford Instruments ER900A cryostat. Spin quantifications were performed with SpinCount (http://www.chem.cmu.edu/groups/hendrich/facilities/index.html), using 1.00 mM $CuSO_4$-EDTA as standard. Mössbauer spectra were acquired using a Model MS4

WRC spectrometer (SEE Co. Edina, MN) and a model LHe6T spectrometer (SEE Co., Edina MN). The latter instrument was equipped with a variable field superconducting magnet capable of generating 0 - 6 Tesla fields. Both instruments were calibrated using a spectrum of α-Fe foil collected at room temperature.

Packing Efficiencies

Jurkat cells were packed into an EPR tube by centrifugation at 800×g for 1 hr (Beckman Avanti-J26 XP centrifuge). Isolated mitochondria were similarly packed at 10000×g (Beckman Ultracentrifuge). The supernatant was discarded. Packed pellets of volume V_{pellet} consisted of the sample and interstitial buffer ($V_{pellet} = V_{sample} + V_{int}$). To determine packing efficiency, defined as $100 \cdot V_{sample}/V_{pellet}$, the pellet was re-suspended in a known volume of buffer ($V_{buffer1}$) containing 100 μM of a membrane-impermeable fluorescent Compound 5 [120]. The sample was packed again for 1 hr. The supernatant, of volume V_{sup1} and containing Compound 5 at concentration C_{sup1}, was removed. C_{sup1} was determined using a fluorescence spectrometer (Koala 90080, ISS Inc). The conservation of matter requires that

$$V_{buffer1} \bullet (100\ \mu M) = (V_{sup1} + V_{int1}) \bullet C_{sup1}$$

where V_{int1} is the volume of the interstitial buffer in the pellet. This equation was solved for V_{int1} allowing the first packing efficiency ($100 \cdot V_{sample1}/V_{pellet1}$) to be determined.

The pellet was re-suspended in a known volume of buffer ($V_{buffer2}$) lacking the fluorescent compound and the suspension was packed again. In this case, the conservation of matter requires that

$$V_{\text{int}2} \cdot C_{\text{sup}1} = (V_{\text{sup}2} + V_{\text{int}2}) \cdot C_{\text{sup}2}$$

C_{sup2}, V_{sup2} and $V_{pellet2}$ were measured as above, allowing V_{int2} and a second packing efficiency ($100 \cdot V_{sample2}/V_{pellet2}$) to be calculated. The two packing efficiencies were averaged. Results from this experiment are summarized in Table A3 (Appendix I).

ICP-MS

Packed whole cells and isolated mitochondria from EPR tubes were diluted with a known volume of buffer (PBS buffer for whole cells, MIB for mitochondria). Suspensions were placed in 15 mL BD Falcon tubes and digested in concentrated trace-metal-grade nitric acid (final concentration ~20-30%) for ~12 hr. Samples were diluted with distilled and deionized water to a final acid concentration of 3%. The metal concentrations of digested samples were determined in both H_2 reaction and He collision modes using ICP-MS (Agilent Technologies model 7700x). Values obtained from both modes were adjusted for dilution factors and packing efficiencies, and then averaged.

Electron Absorption Spectroscopy

Packed cell and mitochondrial samples from EPR tubes were diluted 3-fold with isolation buffer. Suspensions were placed in a custom 2 mm pathlength quartz UV-Vis cuvette (Precision cells), sealed with a septum, and removed from the glove box. Spectra

were acquired on an Hitachi U3310 spectrometer with a Head-on photomultiplier tube, then simulated using OriginPro as described [119].

Western Blots

Forty μg of protein from cell extracts or mitochondria was loaded and separated on a 12% polyacrylamide gel (Bio-Rad) using SDS-containing running buffer and 100 V potential. Proteins were transferred to Immun-Blot PVDF membranes (Bio-Rad) overnight at 20 V. The membranes were incubated for 2 hr using Blocker™ Casein solution (Thermo Scientific). Mouse monoclonal primary antibodies (Abcam) specific to human mitochondrial porin, human endoplasmic reticular protein PDI, human nuclear protein p84 were all diluted 1:1000 and mouse monoclonal antibody specific to human lysosomal protein LAMP1 was diluted 1:10,000 in Blocker™ casein solution. Membranes were incubated with primary antibody solutions for 1 hr, followed by another blocking step for 30 min using Blocker™ casein. Membranes were then incubated with goat anti-mouse HRP conjugated secondary antibody (Invitrogen) diluted 1:3000 in Blocker™ casein solution, followed by detection using the Thermo Scientific Enhanced Chemiluminescent Western Blotting Substrate. Images were obtained using the FujiFilm LAS-4000 mini imager and analyzed using ImageJ.

Electron Microscopy

Mitochondria were fixed in 3% (v/v) glutaraldehyde in MIB, washed 3 times with MIB, fixed in 1% (v/v) osmium tetroxide, infiltrated and embedded in epoxy resin

by polymerization at 60° C overnight. Ultrathin sections were obtained using an Ultracut E microtome (Reichert-Jung) and post-stained on drops of 2% (w/v) uranyl acetate and 100 mM lead citrate as described [138]. EM images were obtained on a JEOL 1200 EX Transmission Electron Microscope.

Results

Analytical Characterization

Eighteen batches of Jurkat cells were grown in medium containing ~ 6 μM endogenous ^{56}Fe, as measured by ICP-MS, and supplemented with 10 μM $^{57}Fe^{III}$ citrate. The percent enrichment (*ca*. 75%) indicates that the cells incorporated both sources of Fe. Mitochondria were isolated from 11 of these batches. Due to limited amounts of material, not every batch could be characterized by every technique; characterizations performed on each batch are summarized in Table A1 and A2 (see Appendix I).

Purities of 6 batches of isolated mitochondria were evaluated by Western blots and the membrane integrity of 4 batches was assessed using EM (Table A2). Western analysis indicated a 10-fold increase in the porin protein, a marker of mitochondria, in isolated mitochondria relative to in the same number of mg of cell extract. Isolated mitochondria contained small levels of contaminating proteins, including the marker proteins LAMP1 from lysosomes, p84 from nuclei, and PDI from ER **(**Figure 2-2, top panel**)**. EM images of isolated mitochondria **(**Figure 2-2, bottom panel**)** generally

	Mitochondria	*n*	Whole Cells	*n*
Protein (mg/mL)	52 ± 12	4	62 ± 11	4
[Fe] (μM)	1120 ± 95	5	400 ± 70	5
[Cu] (μM)	115 ± 8	5	28 ± 4	5
[Zn] (μM)	167± 94	5	408 ± 135	5
[Mn] (μM)	14 ± 3	5	7.2 ± 0.6	5
Fe^{III} oxyhydroxy nanoparticles (%)	37	3	18	2
Ferritin-like (%)	15	3	40	2
Central Doublet (%)	27	3	27	2
Non-Heme HS Fe^{II}	8	3	11	2
HS Fe^{II} Hemes	4	3	4	2
g = 1.94 (μM)	3.3 ± 0.6	4	0.3±0.1	4
g = 1.90 (μM)	3.3 ± 0.6	4	0.3±0.1	4
g = 2.00 (μM)	0.2 ±0.06	4	~ 0	4
g = 4.3 (μM)	6 ±0.6	4	1.5 ± 0.5	4
g = 6.0 + (6.4, 5.4)	0.5 ±0.3	4	~ 0	4
Reduced [Heme *a*] (μM)	37 ± 5	4	10 ± 2	4
Reduced [Heme *b*] (μM)	21 ± 4	4	5 ± 2	4
Reduced [Heme *c*] (μM)	75 ± 11	4	20 ± 3	4
Cytochrome *c* oxidase (μM)	~ 18		n/a	
Cytochrome *c* (μM)	~ 70		n/a	
Cytochrome bc_1 (μM)	~ 4		n/a	
Succinate Dehydrogenase (μM)	~ 4		n/a	
Respiratory Complex I (μM)	~ 1		n/a	

Table 2-1. Analytical properties of whole Jurkat cells and isolated mitochondria. Reported metal, UV-vis and EPR concentrations refer to packed cells and mitochondria after dividing by packing efficiencies. Values reported for isolated mitochondria were obtained by also dividing measured values by 0.75, to account for presumed metal-free impurities. The absolute uncertainty in percentages obtained by Mössbauer spectroscopy is ± 3%. Replicates *n* is given in the column to the right of the corresponding parameter. Concentrations of respiration-related mitochondrial proteins are estimated from the collective results of this study.

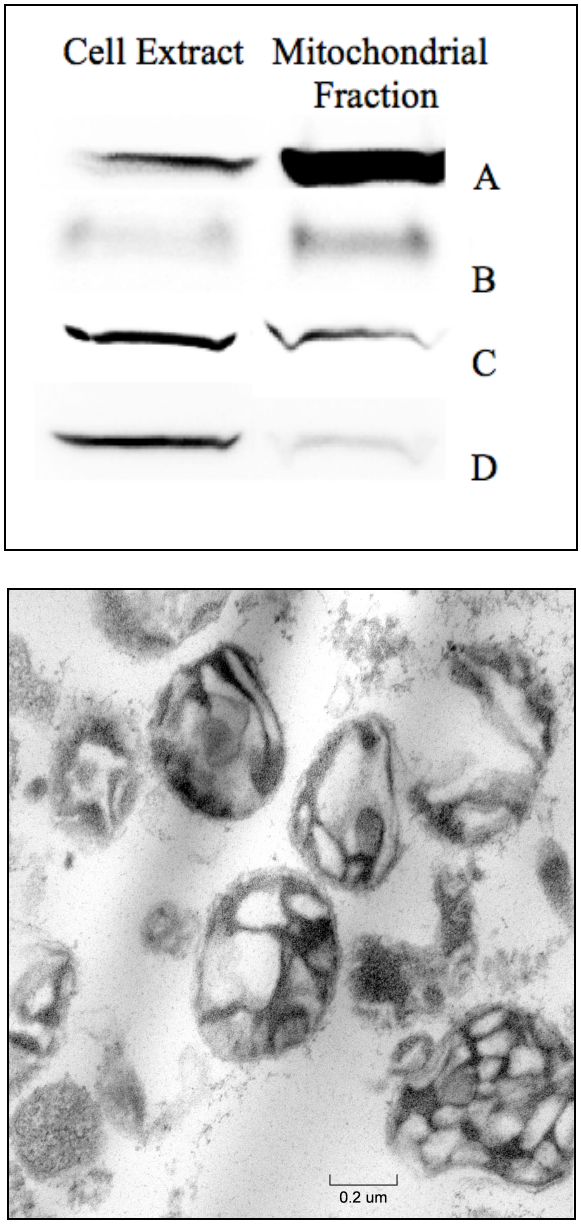

Figure 2-2. Characterization of isolated mitochondria. Top, western blot of isolated mitochondria; A, Porin (mitochondria); B, LAMP1 (lysosomes); C, Endoplasmic reticulum (PDI); and D, p84 (nuclei). Bottom, electron micrograph of isolated mitochondria, magnification = 40,000×.

showed intact organelles with sharp cristae, though some unidentified electron density was evident. In summary, the EM and western blot analysis suggests that the mitochondria used in this study were 70% - 80% pure and generally intact.

We determined the absolute concentration of metal ions and protein in 5 batches of mitochondria and 5 batches of whole cells (summarized in Table 2-1, individual determinations in Appendix I, Table A4). These values were obtained by dividing observed concentrations in packed mitochondria and cells by measured packing efficiencies (65% ± 10% and 81% ± 6%, respectively).

Biophysical Characterization of Mitochondria

Three batches of isolated mitochondria were analyzed (results summarized in Table 2-1). Low-temperature low-field Mössbauer spectra exhibited 4 distinguishable species; the spectrum from one batch is shown in Figure 2-3A while others are given in Figure A1 (see Appendix II). The dominating feature consisted of two overlapping quadrupole doublets in the center of the spectrum. This includes the central doublet (CD) with parameters typical of S = 0 $[Fe_4S_4]^{2+}$ clusters and low-spin (LS) ferrous heme centers (δ = 0.46 mm/s; ΔE_Q = 1.2 mm/s), and a broad doublet with parameters δ = 0.48 mm/s and ΔE_Q = 0.57 mm/s. These parameters are typical of Fe^{III} (phosphate) oxy-hydroxo nanoparticles, as has been observed previously in various genetic strains of yeast mitochondria [117, 139]. The blue and purple lines in Figure 2-3A are respective simulations of these two doublets.

Figure 2-3. Mössbauer spectra of mitochondria isolated from Jurkat cells. A, 5 K and 0.05 T; the red line is a total simulation (see Table 2-1 for percentages); B, same as A but at 70 K, with simulation of NHHS Fe^{II}; C, same as A except at 6 T and 4.3 K. The brown line simulates the ferritin sextet while the blue line simulates the CD; D, same as C but after subtraction of sextet and CD simulations. The red line is a 6 T, 4.3 K spectrum of yeast mitochondria isolated from Aft1-1^{up} cells [120]. The applied magnetic field was parallel to the γ radiation in A and B, perpendicular in C and D. mm/s; ΔE_Q = 2.00 mm/s) was simulated (brown line, Figure 2-3A). The doublet simulated by the green line had parameters (δ = 1.30 mm/s; ΔE_Q = 3.00 mm/s) typical of *non-heme* HS Fe^{II} ions.

Figure 2-3 (Continued)

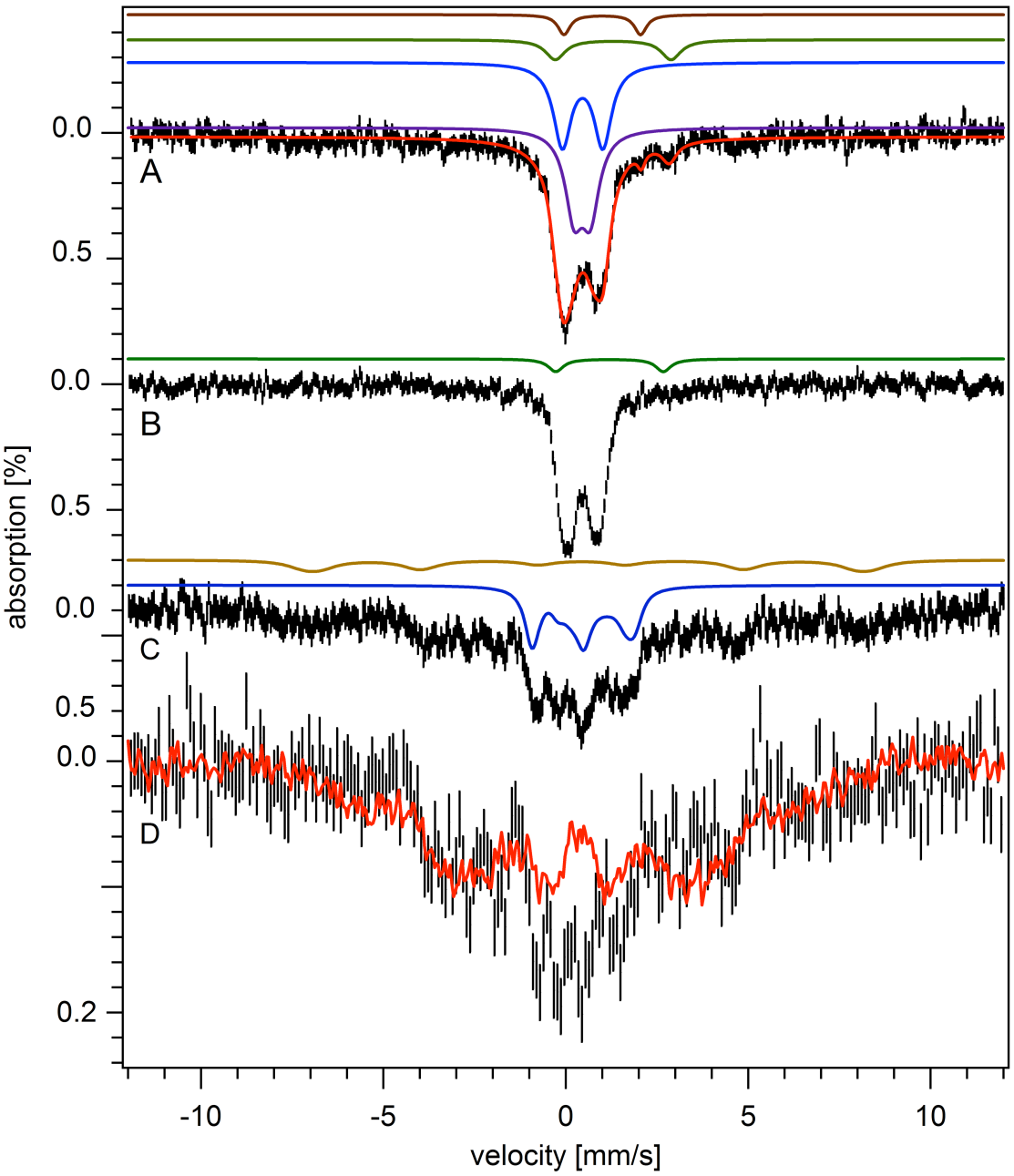

The magnetic properties associated with the two doublets were investigated by collecting a Mössbauer spectrum at high applied magnetic field (Figure 2-3C). The solid blue line simulates the CD and confirms that the species associated with this doublet are diamagnetic. The nanoparticle doublet broadened significantly at 6 T. Although we have not simulated this feature, we collected the corresponding spectrum of a yeast sample dominated by Fe^{III} oxyhydroxo nanoparticles [120]. Within the noise of the data, the spectral features (Figure 2-3D) were similar, adding evidence that the second doublet in the low-field spectrum arises from similar nanoparticles in human mitochondria. The low-temperature, low-field spectrum of human mitochondria included 3 minor features. A quadrupole doublet with parameters typical of HS Fe^{II} hemes (δ = 1.00 coordinated by ligands with predominately O and N donors. The concentrations of heme centers in isolated mitochondria were quantified most accurately by electronic absorption spectroscopy (Figure A on Pg. 45 and Table 2-1).

The final low-intensity feature in the 5 K 0.05 T spectrum of isolated mitochondria included broad features that were barely distinguishable from the baseline and were spread over the recorded velocity range (Figure 2-3A). At 70 K, these features collapsed into the center of the spectrum (Figure 2-3B) as is typical of ferritin. At 6 T, the same features sharpened slightly, revealing the same positions as the ferritin sextet in whole cell spectra (Figure 2-3C). These features in mitochondria could arise from either contaminating ferritin, mitoferritin or other materials with ferritin-like spectral features.

In the g = 2 region, low-temperature EPR spectra of isolated mitochondria were dominated by signals with g_{ave} = 1.94, 1.98, 2.00 and 2.02 (Figure A on Pg. 42). Spin

quantifications are given in Table 2-1. The signals at g_{ave} = 1.98 and g_{ave} = 2.09 may arise from Fe/S clusters but this is uncertain. The g_{ave} = 2.00 signal probably originates from an organic radical, whereas the g_{ave} = 1.94 signal probably arises from the $[Fe_2S_2]^+$ cluster of succinate dehydrogenase [116]. A low-intensity signal at g_{ave} = 2.15 was reproducibly present, but its origin is unknown.

In the low-field region, mitochondria exhibited two EPR signals (Figure 2-4B). The one at g_{ave} = 4.3 was assigned to non-heme HS Fe^{III} species with rhombic symmetry. The signal at g_{ave} = 6.0, which corresponds to a HS Fe^{III} heme, probably arises from the active site of cytochrome *c* oxidase in a mixed redox state in which heme a_3 is oxidized and Cu_b is reduced [140]. At high temperatures, a broad EPR signal in the g = 2 region developed, with inverse Curie law temperature dependence (Figure 2-4C). Such behavior is characteristic of superparamagnetic species such as Fe^{III} oxyhydroxo nanoparticles.

Biophysical Characterization of Whole Cells

Two batches of whole Jurkat cells were characterized (results summarized in Table 2-1). The dominant feature in the 5 K 0.05 T Mössbauer spectrum (Figure A on Pg. 43) was a broad sextet with effective isomer shift and quadrupole parameters (δ = 0.55 mm/s; ΔE_Q = 0.25 mm/s; H_{int} = 480 kG); the light-brown line is a simulation. This species was reminiscent of the HS Fe^{III} ions in ferritin [141]. The sextet was also observed at 4.3 K and 6 T field (Figure C on Pg. 43); under these conditions the magnetic

Figure 2-4. X-band EPR spectra of Jurkat cells and mitochondria. A, high-field region of (*i*) cells and (*ii*) mitochondria (ave. of 5 and 3 scans, respectively). Simulations *iii*, *iv*, *v*, and *vi* were of the g_{ave} = 1.94, 1.90, 2.00, and 1.98 signals, respectively. The solid line overlaying *ii* is a combined simulation. Temperature, 8 K; frequency, 9.47 GHz; microwave power, 2.012 mW. B, low-field region of (*i*) cells and (*ii*) mitochondria (ave. of 5 and 3 scans, respectively). Simulations *iii* and *iv* are of the g = 4.3 and 6.0 features, respectively. The solid line overlaying *ii* is a combined simulation (same EPR conditions). C, wide-sweep spectra of mitochondria at 8 K (*i*) and 80 K (*ii*). Frequency, 9.46 GHz, power, 20.12 mW. In all spectra, modulation amplitude was 10 G, modulation frequency, 100 kHz, conversion time, 164 ms, and sweep time, 336 sec.

Figure 2-4 (Continued)

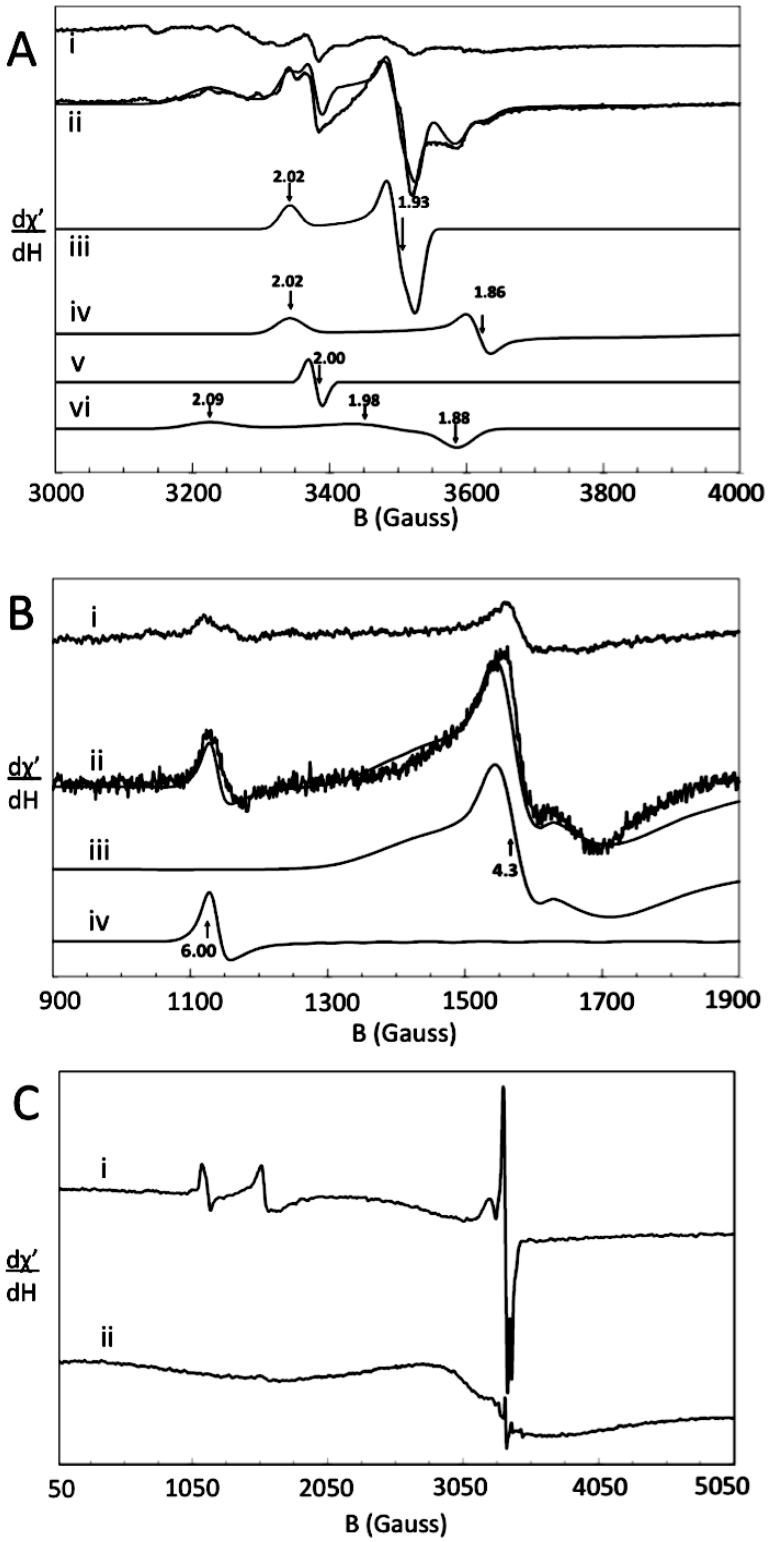

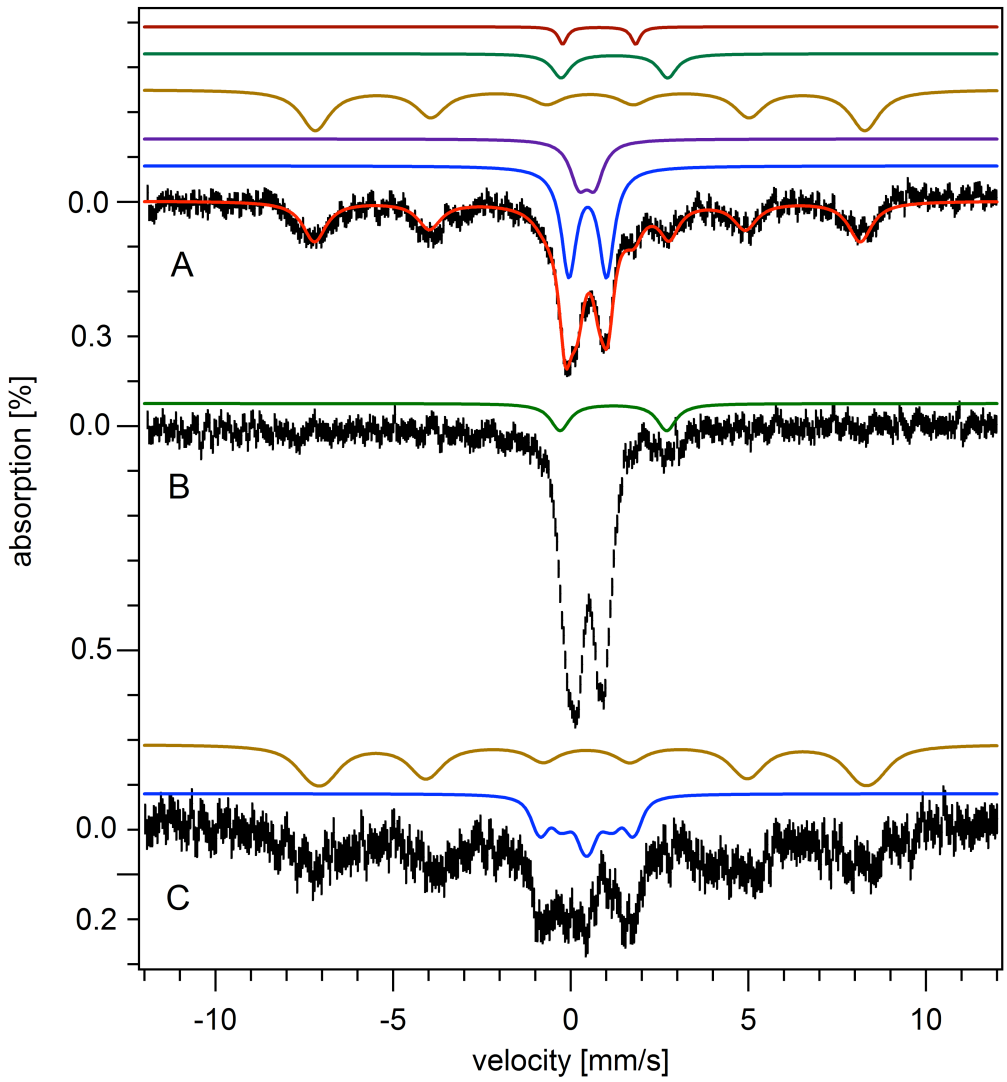

Figure 2-5. Mössbauer spectroscopy of Jurkat cells. A, 5 K and 0.05 T. Colored lines above the spectrum are individual simulations; the overlaid red line is a total simulation (see Table 2-1 for percentages). B, 70 K 0.05 T. The green line simulates the NHHS Fe^{II} doublet. C, 6 T and 4.3 K. The brown and blue lines simulate the sextet and CD respectively.

hyperfine interactions were similar to those of ferritin (δ = 0.54 mm/s; ΔE_Q = 0.20 mm/s; H_{int} = 450 kG; η = 1.00). At 70 K, the sextet collapsed into a quadrupole doublet (Figure 2-5B) as is again typical of ferritin (δ = 0.50 mm/s; ΔE_Q = 0.75 mm/s). We conclude that the sextet arises from ferritin or other very similar superparamagnetic Fe^{III} material. The other features of the 5 K, 0.05 T Mössbauer spectrum of whole Jurkat cells were essentially identical to those found in spectra of isolated mitochondria. These included a central doublet (δ = 0.46 mm/s; ΔE_Q = 1.20 mm/s), a nanoparticle doublet (δ = 0.48 mm/s; ΔE_Q = 0.57 mm/s), a quadrupole doublet from HS Fe^{II} hemes (δ = 1.00 mm/s; ΔE_Q = 2.00 mm/s) and a doublet arising from non-heme HS Fe^{II} species (δ = 1.30 mm/s; ΔE_Q = 3.00 mm/s). Concentrations of Fe^{II} heme *a*, *b* and *c* centers in whole Jurkat cells were quantified (Figure 2-6, Table 2-1).

The low-temperature X-band EPR spectra of whole cells exhibited numerous low-intensity features similar to those from isolated mitochondria, including at g_{ave} = 1.94, 1.98, 2.00 and 2.02 in the high field region, and g_{ave} = 6.0 and 4.3 at low field (Figure 2-4, A and B). These signals were 5-7 fold less intense in whole cell EPR spectra relative to in corresponding mitochondrial spectra.

Discussion

We determined the absolute concentrations of iron and other transition metals in Jurkat cells and mitochondria by determining packing efficiencies, and using them to correct the concentration of metals obtained in packed samples. There are few previous

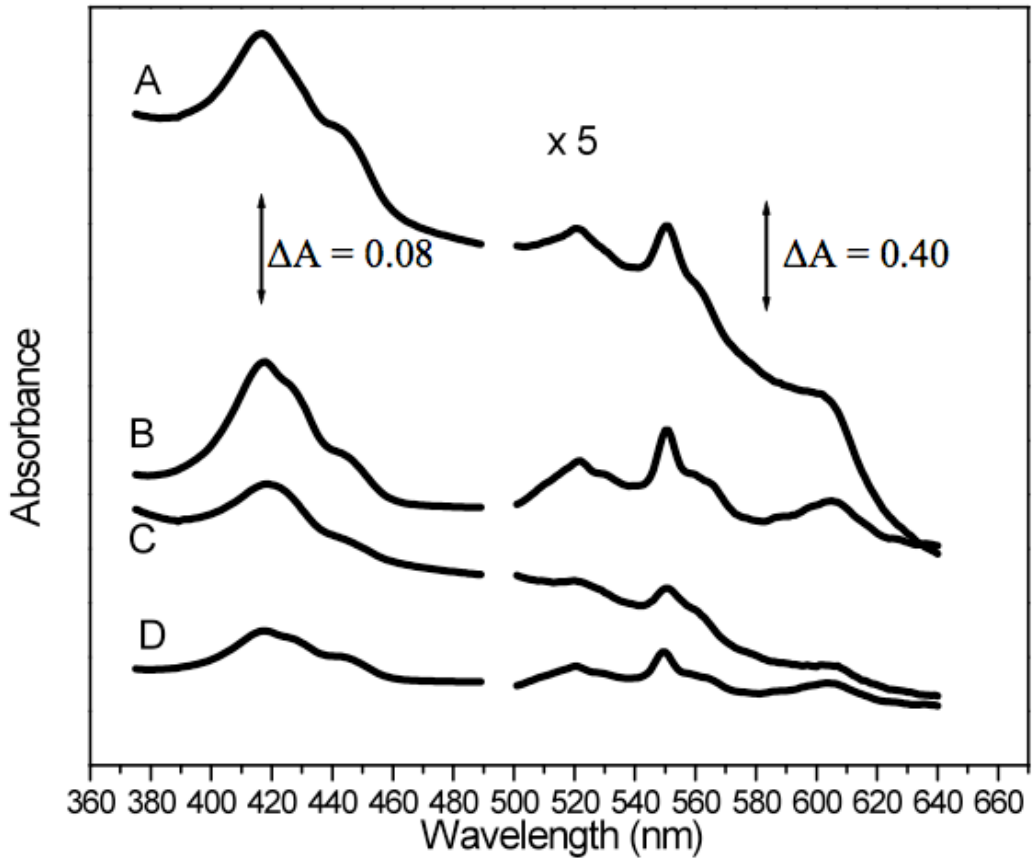

Figure 2-6. Electronic absorption spectra of mitochondrial (A) and cell (C) suspensions. Simulated spectra B and D were generated by combining individual spectra of isolated proteins containing the different types of hemes.

reports of absolute metal ion concentrations in mammalian cells; most are given as Fe:protein concentration ratios. Some reports of total intracellular iron concentration, as well as mitochondrial iron content, agree with our measurements of Fe:protein ratios [106, 107, 142]. However, other published ratios are dramatically different. Assuming a cellular volume of 200 fL [143] we calculated from published data [144] that lymphocytes contain ~ 5 mM Fe, 12 times higher than we measured. Another determination in the same type of cells indicated 0.3-0.4 μmol Fe/g protein [145], 45-fold lower than we measured. Rat intestinal epithelial cells reportedly contained ~ 1.4 μmol Fe/g protein [129], ~10-fold lower than our measurements. Besides being outside the range of concentrations that we observed, these reported concentrations are inconsistent with the Mössbauer and EPR intensities observed here. A 5 mM Fe sample would exhibit far greater % effect and spin intensities than we observed, and spectra would be unobtainable with samples that contain < 100 μM Fe. The Fe concentrations reported here and in some previous reports are fully consistent with the spectroscopic intensities exhibited by our samples.

Our results allow us to estimate the fraction of Jurkat cell volume due to mitochondria (V_{mito}/V_{cell}). Heme *a* is exclusively found in cytochrome *c* oxidase, a mitochondrial protein, and the UV-Vis spectral absorption due to reduced heme *a* is well isolated from other heme signals so that its intensity in whole cells *vs*. mitochondria can be compared with reasonable accuracy. This comparison (Table 2-1) suggests $V_{mito}/V_{cell} \approx 0.27$. Heme *c* may also be found exclusively in mitochondria (as cytochrome *c* and cytochrome bc_1); in this case, the heme *c* concentrations in Table 2-1 suggest the same value for V_{mito}/V_{cell}. After correcting for dilution factors, packing efficiencies and an

estimated 25% heme-free impurities, mitochondrial spectra were 4.3 times as intense as whole cell spectra, suggesting $V_{mito}/V_{cell} \approx 0.23$.

Our Fe concentrations, when considered with the cytosolic location of ferritin and the conservation of matter suggests the relationship

$$[Fe]_{cell} - [Fe]_{ferittin} = [Fe]_{mito} \cdot \frac{V_{mito}}{V_{cell}} + [Fe]_{other} \cdot \left(1 - \frac{V_{mito}}{V_{cell}}\right) \quad (1)$$

where $[Fe]_{other}$ is the average [Fe] in all non-mitochondrial compartments of the cell. Solutions of this equation are restricted by our data such that $V_{mito}/V_{cell} \leq 0.29$. Comparing EPR signal intensities in whole cell *vs*. mitochondria spectra suggested a lower ratio, $V_{mito}/V_{cell} \approx 0.17$, but the uncertainty associated with this number is larger. We conclude from all of these measurements that $V_{mito}/V_{cell} \approx 0.20 \pm 0.04$. Previous electron microscopy studies have measured this ratio in liver cells to be 0.18 [146].

Our results also allow us to estimate the concentrations for the respiratory complexes in human mitochondria (Table 2-1, lower section). The concentration of cytochrome *c* oxidase is ~ 18 μM, half of the concentration of heme $a+a_3$, as determined by UV-vis. This concentration (and others in Table 2-1 and below) refer to moles per mitochondrial volume; the concentration within the particular compartment of the mitochondria where the enzyme is located (the IM, in this case) will be substantially higher. Heme *a* is LS and likely contributes to the CD, while heme a_3 is HS and contributes to the HS Fe^{II} doublet. Cytochrome c oxidase binds 3 Cu ions, suggesting that about *half* (54 μM out of 115 μM) of the Cu in mitochondria is associated with this enzyme. Most of the remainder may be associated with a Cu pool [147]. Since no Cu^{II} EPR

signals were apparent in spectra of mitochondria, we conclude that most or all of the Cu ions in this pool are in the Cu^{1+} state.

By assuming that 20% of Jurkat cell volume is occupied by mitochondria, the same type of conservation-of-matter relationships as used for Fe suggests that the average concentrations of Cu, Mn, and Zn in non-mitochondrial locations within the cell are 6, 4, and 375 μM, respectively. Thus, 82%, 39% and 8% of the Cu, Mn, and Zn in the cell, respectively, appear to be located in mitochondria.

The HS Fe^{III} heme EPR feature at $g_{ave} = 6$ (corresponding to Fe^{III} heme a_3 and Cu_b^{1+}) represents ~ 3% of cytochrome *c* oxidase molecules. This signal has been called a "transient" catalytic intermediate arising from the one-electron reduction of the oxidized O_H state [148, 149]. However, our results demonstrate that it is *not* a transient – it is stable and present reproducibly under non-turnover conditions in both whole cells and anaerobically isolated mitochondria. Establishing whether this state functions in catalysis will require further study, but at minimum, our results suggest that the thermodynamic reduction potential of the heme a_3 (Fe^{III}/Fe^{II}) couple is *less positive* than that of the $Cu_b^{2+/}Cu_b^{1+}$ couple under *in vivo* conditions. This conclusion is supported by a previous determination of $E^{0'} = 210$ mV vs. SHE for heme a_3 and 340 mV for Cu_B [8]. We calculate a potential of *ca*. 170 mV for the solution in equilibrium with this site, under the (anaerobic) conditions of our experiments.

We estimate a concentration of ~ 4 μM for cytochrome bc_1 in mitochondria, based primarily on the spin concentration of the $g_{ave} = 1.90$ signal due to the Rieske Fe/S cluster associated with this respiratory complex. This complex contains 1 and 2

equiv/mol of LS heme c_1 and LS heme *b*, respectively, both of which would have contributed to the CD. We estimate a similar concentration for RCII in mitochondria, based on the g_{ave} = 1.94 signal intensity which we presume arises from its $[Fe_2S_2]^{1+}$ cluster. This enzyme also contains 1 LS Heme *b*, an $[Fe_3S_4]$ cluster and an $[Fe_4S_4]$ cluster. Collectively, the heme *b* contribution of both respiratory complexes is ~ 8 μM, suggesting that ~ 14 μM of heme *b* is due to other mitochondrial proteins such as catalase and cytochrome *c* peroxidase. The heme *c* contribution due to cytochrome bc_1 is minor, suggesting that concentration of cytochrome *c* in the mitochondria is ~ 70 μM.

Heme *c* centers are LS, as is the heme *a* center of cytochrome *c* oxidase and, we estimate, about half of the heme *b* centers. Collectively, this corresponds to ~ 100 μM, about 9% of mitochondrial Fe, and it would be contained in the CD. Since the CD represents ~ 27% of the Fe in the mitochondria, we conclude that ~ 17% (200 μM) is due to Fe in the form of $[Fe_4S_4]^{2+}$ clusters. After subtracting ~ 4 μM $[Fe_4S_4]$ due to succinate dehydrogenase, we are left with ~ 46 μM $[Fe_4S_4]$-containing proteins.

The ratios of RCI:RCIII:RCIV have been measured in various rat and bovine tissues to be ca. 1:3:8 [150]. The ratio of RCIII:RCIV in our mitochondrial samples is 3:18, which suggests an RCI concentration of 0.5 - 1 μM. Since RCI contains 6 $[Fe_4S_4]$ clusters and 2 $[Fe_2S_2]$ clusters, ~ 6 μM of $[Fe_4S_4]$ clusters due to RCI would contribute to the CD, leaving ~ 40 μM $[Fe_4S_4]$ clusters due to the sum of all other mitochondrial proteins (e.g. aconitase, homoaconitase, dihydroxyacid dehydratase, biotin synthase, lipoic acid synthase etc). As with yeast mitochondria [119], the concentration of $[Fe_2S_2]^{2+}$

clusters in human mitochondria seems low since a doublet due to this species is not observed in Mössbauer spectra.

If 20% of the cell volume is due to mitochondria, then ~ 55% of the Fe in the cell (220 μM) should be mitochondrial. Of this, *ca*. 27% (60 μM) is due to the CD. This would correspond to about 12% of the Fe in the whole cell spectrum. But the CD in the whole cell spectrum represents 27% of spectral intensity, corresponding to 108 μM. The difference 100 – 60 μM = 40 μM Fe represents the CD material in the cell that is not present in the mitochondria. This should be some combination of $[Fe_4S_4]^{2+}$ clusters and LS Fe^{II} hemes in the cell that are not in mitochondria.

Human mitochondria contain ~ 90 μM of HS Fe^{II} species. Some of these species are undoubtedly protein-bound, while others are probably associated with the mitochondrial LIP. The LIP was hypothesized to be present mostly in the Fe^{II} state [151]. Non-mitochondrial portions of the cell contain, on average, ~50 μM nonheme HS Fe^{II}; this is an upper limit for the cytosolic LIP. The size of the LIP has been estimated from the change in absorbance upon treating cell extracts with bathophenanthroline sulfonate [106] or fluorescent iron-binding chelators [39, 151-153]. Concentrations ranging from ~ 0.5 μM (erythroleukemic cells and lymphocytes) [154, 155] to ~ 10 μM (human and rat hepatocytes, liver endothelial cells) have been reported [152, 156].

Our results also show the presence of Fe^{III} oxyhydroxo nanoparticles in both mitochondria and whole cells. Considering the total iron concentrations of whole cells and mitochondria as determined by ICP-MS, the concentration of these nanoparticles appears to be ~ 73 μM in whole cells and ~ 410 μM in isolated mitochondria. Assuming

that mitochondria occupy 20% of the cell's volume, this ratio suggests that most if not all of the nanoparticles present in a cell are located in the mitochondria. Similar Fe^{III} oxyhydroxo nanoparticles have been observed in the mitochondria and vacuoles of yeast cells [118-120]. These particles are probably associated with phosphate (or polyphosphate) groups. At high fields, the Mössbauer spectra of these particles exhibit a wide distribution of hyperfine fields ranging from 0 - 40 T [157-159]. In contrast, the magnetically interacting Fe^{III} ions in the ferritin core afford a narrow range of hyperfine fields. The nanoparticles observed in human Jurkat cells and mitochondria exhibit a wide distribution of hyperfine fields, suggesting that they may have phosphate associated. This is the first evidence of Fe^{III} oxyhydroxo phosphate nanoparticles in human cells.

Our results also provide insight into the redox status of the mitochondria *within* Jurkat cells. The cells were grown in medium sparged with 20% O_2, and harvested and packed into Mössbauer/EPR cups/tubes in air. In contrast, mitochondria were isolated in a glove box under strict anaerobic conditions. Interestingly, almost all heme centers (and the same group of Fe/S clusters) in both types of samples were reduced. The only exception was a small portion of heme a_3 in the active site of cytochrome *c* oxidase, which was oxidized in both types of samples. This rather reduced redox state might be expected for mitochondria isolated anaerobically, but not for cells isolated in air. We conclude that the basal state of mitochondria within cells is *reducing* relative to most hemes and that this redox poise is not altered during the anaerobic isolation of the organelle.

The distribution of iron within Jurkat cells and their mitochondria are summarized in Figure 2-7. A surprisingly large portion of the Fe in mitochondria (37%, Figure 2-7) is present as Fe^{III} oxyhydroxo (phosphate) nanoparticles. These particles might be in equilibrium with the nonheme HS Fe^{II} and Fe^{III} species (9% of mitochondrial Fe). Similar species are present in yeast mitochondria, where they may exist in redox equilibrium and function as feedstock for Fe/S cluster and heme biosynthesis [119, 120]. Collectively, the respiratory complexes (including cytochrome *c*) account for about 17% of mitochondrial Fe. Another 14% of mitochondrial Fe is present as "other" $[Fe_4S_4]^{2+}$ clusters and heme *b* centers. About 15% of mitochondrial Fe is ferritin-like; this may be a contaminant of ferritin or ferritin-like material inside the mitochondria (mitochondrial ferritin?).

Approximately 20% of the volume of whole Jurkat cells is occupied by mitochondria, yet this fraction accounts for about *55%* of the Fe in the cell. Another 40% of cellular Fe is stored in the cytosol as ferritin and the remaining 5% is present (outside of the mitochondria) as Fe/S containing proteins, nonheme HS Fe^{II} and Fe^{III} species. Thus, the vast majority of Fe in human cells is either *stored* (as ferritin) or *used* (within mitochondria). The bulk of the latter Fe is used to synthesize Fe/S clusters and heme centers that are primarily installed in respiratory complexes, which are used, in turn, to generate cellular energy. Only ~5% of cellular Fe is used for all other Fe-associated processes. This does not imply a lesser functional importance for these other processes; we simply lack the resolution and sensitivity required to further characterize the Fe species associated with these processes.

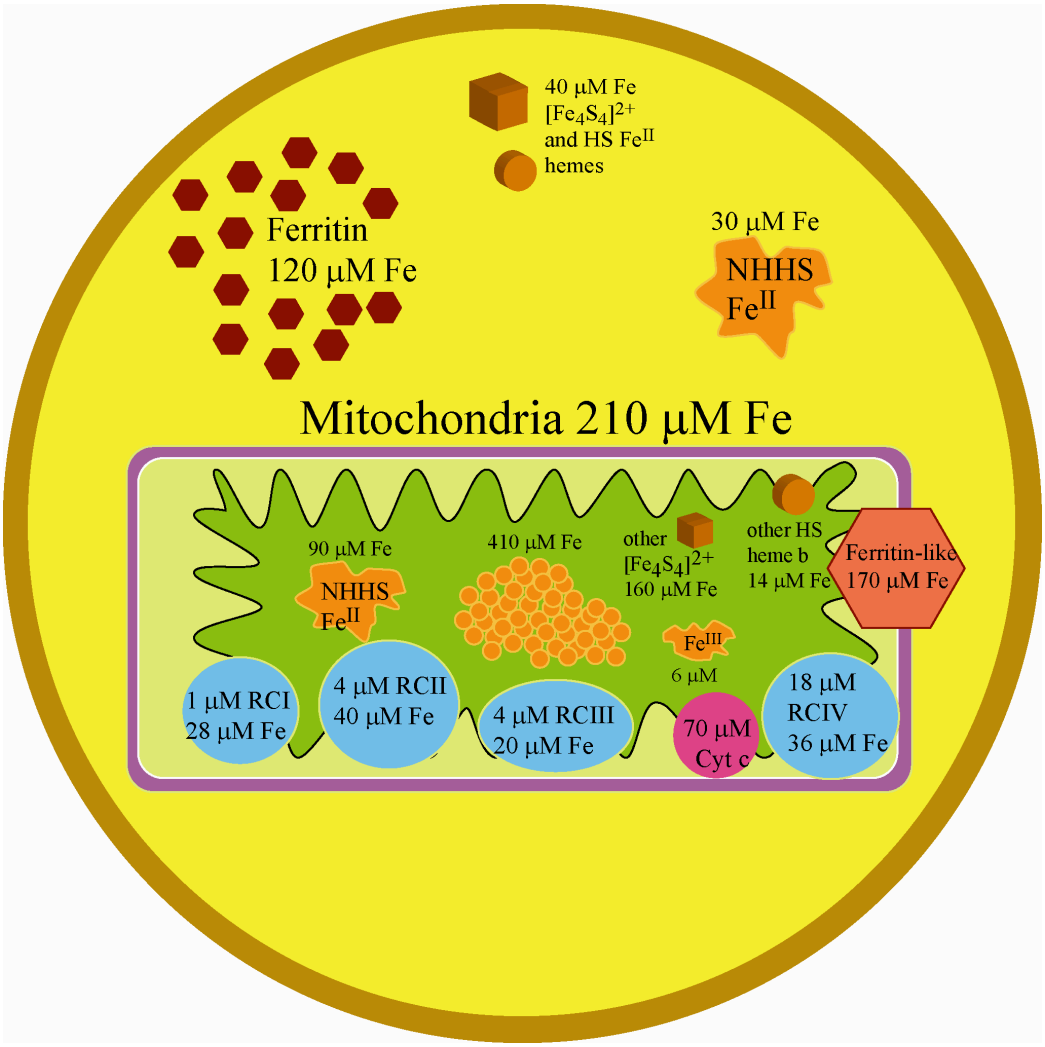

Figure 2-7. Ironome profile of Jurkat cells and mitochondria.

The iron distributions of yeast cells and mitochondria have also been studied using the same biophysical techniques, and it is interesting to compare the ironomes of yeast and human cells. The ironome of Jurkat mitochondria resides somewhere between those of fermenting and respiring yeast. The redox poise of the organelle and the relative proportion iron-containing species (including respiratory complexes) contained therein are very similar between yeast and humans. Clearly, yeast provides an excellent model of human cells for the study of Fe metabolism. Curiously even the human mitochondria contain nanoparticles, similar to those found in yeast. The formation of these particles is probably not under the genetic control of the cell. Rather, they probably result from chemical processes of which the cell is oblivious; thus, even human cells are unable to guard efficiently against iron overload. Indeed such problems are evident in human diseases. The significant levels of nonheme HS Fe^{II} species observed in human cells is also potentially significant, in that this is the type of Fe that can generate ROS through Fenton chemistry and thereby contribute to human disease. We plan to investigate how these nanoparticle and nonheme HS Fe^{II} species change under different growth and genetic conditions, and hopefully establish how these species can be controlled.

CHAPTER III

MÖSSBAUER STUDY AND MODELING OF IRON IMPORT AND TRAFFICKING IN HUMAN JURKAT CELLS

Introduction

Iron is essential in human metabolism due to its extensive redox, substrate binding, and catalytic properties. This transition metal is found in various forms, including hemes, Fe/S clusters, and nonheme mononuclear and binuclear centers. Conversely, excess Fe is widely regarded to be toxic to cells because it can generate Reactive Oxygen Species (ROS) through the Fenton reaction [125]. Hence, Fe import, trafficking, utilization and storage must be tightly regulated by cells.

Mammalian cells import Fe through many pathways, the best studied of which involves transferrin, a blood plasma protein that coordinates two Fe^{III} ions [24]. The cell-surface transferrin receptor TfRC1 mediates the endocytic import of transferrin-bound iron (TBI). This is followed by acidification of the endosome, release of Fe^{III} from transferrin, reduction of Fe^{III} to Fe^{II} and subsequent export of Fe^{II} from the endosome to the cytosol via the divalent metal transporter DMT1 [29]. The expression of TfRC1 is regulated post-transcriptionally by the iron regulatory proteins IRP1 and IRP2 [87]. Both bind to and stabilize the 3'-UTR of TfRC1 mRNA under iron-deficient conditions. This promotes TfRC1 translation and thus Fe import via the TBI pathway [87].

IRP1/2 also regulate the concentration of ferritin in the cell. Ferritin is a spherical 24- subunit protein complex used by the cell to store Fe. It has a hollow 7 nm-diameter core that can store up to ~ 4500 Fe^{III} ions as an oxyhydroxide aggregate [11]. When cells are iron deficient, IRP1/2 bind to the 5'-UTR of ferritin mRNA. This prevents mRNA translation, and leads to a decline of ferritin expression. When cells are Fe replete, IRP1/2 do not bind ferritin mRNA which increases ferritin expression, allowing storage of excess cellular Fe [87].

Other Fe import pathways are less well defined, and are often referred to as a single pathway in which a poorly defined species called non-transferrin-bound iron (NTBI) is imported [160]. Fe^{III} citrate (FC) is a likely component of NTBI [127, 161]. However, few details are known regarding the NTBI import pathway and the role of this/these Fe species in cellular physiology. An uncharacterized cell-surface ferrireductase has been implicated in the reduction of NTBI Fe^{III} to Fe^{II} prior to uptake [128]. Cell-surface metal transporters such as DMT1 [162], the zinc transporter ZIP14 [30] and L-type calcium channels [28] may be involved. NTBI may also be imported via bulk/adsorptive endocytosis [36].

Although poorly defined, NTBI plays important roles in a number of diseases. NTBI is found in the blood plasma of patients with Fe-overload diseases such as β-thalassemia [27], idiopathic hemochromatosis [163], hypotransferrinemia [164], and hereditary hemochromatosis [165]. This typically leads to iron accumulation in the liver and/or spleen. NTBI has also been implicated in the pathology of Alzheimer's disease [166]. NTBI uptake is not as tightly controlled as that of TBI, consistent with a role for NTBI in cellular Fe

overload and Fe-induced toxicity [160]. Hepatocytes import NTBI > 20-fold faster than they import TBI [167], which explains why NTBI is cleared efficiently from the blood by the liver [168]. Growth of cells on NTBI leads to severe Fe overload and oxidative damage [25, 169, 170].

Few studies have probed Fe metabolism in human cells using iron-centric methods such as Mössbauer (MB) spectroscopy. This technique, used in conjunction with EPR and other biophysical methods (e.g. UV-vis and EM), can effectively evaluate the speciation of Fe in cells [124, 171, 172], including human Jurkat cells grown in medium containing 10 μM FC [124]. The majority of Fe in these Fe-replete cells is bound to ferritin. Also evident are $[Fe_4S_4]$ clusters and heme centers primarily associated with mitochondrial respiratory complexes, and Fe^{III} oxyhydroxide nanoparticles that exhibit superparamagnetic behavior [124]. In low-temperature low-field MB spectra, the nanoparticles exhibited a broad quadrupole doublet with $\delta = 0.48$ mm/s, $\Delta E_Q = 0.57$ mm/s.

Whitnall *et al*. recently used MB spectroscopy to identify nonferritin mitochondrial Fe deposits in a mouse model of Friedreich's ataxia [173]. Friedrich's ataxia is the most common autosomal recessive ataxia; it causes progressive degeneration of the nervous system and heart. The deposits which they observed in heart tissue exhibited a broad quadrupole doublet in low-temperature low-field MB spectra. The parameters associated with this doublet ($\delta = 0.48$ mm/s, $\Delta E_Q = 0.71$ mm/s) are similar to those observed in Jurkat cells [124]. The mice had a muscle creatine kinase conditional knockout of frataxin, a mitochondrial matrix protein involved in Fe/S cluster

biosynthesis [174]. Yeast lacking the frataxin homolog (Yfh1p) accumulate massive amounts of Fe^{III} phosphate oxyhydroxide nanoparticles in their mitochondria, along with a deficiency of Fe/S clusters and heme centers [159].

Here, we report how the cellular concentrations of such Fe-containing species in human Jurkat cells vary with the concentration of FC and TBI in the growth medium. We examine the effect of different carbon sources (glucose *vs.* galactose) on the Fe content of these cells, and the effect of altering the expression levels of the transferrin receptor and frataxin. A mathematical model defining the fate of Fe that enters the cell as TBI and FC is developed.

Experimental Procedures

Cell Culture

Cells were grown in a 24 L custom-designed all-glass bioreactor [124]. Cells were counted and viability evaluated as described [124]. Glucose-free RPMI 1640 custom-formulated powder (Gemini Bio-Products, West Sacramento, CA) was reconstituted in distilled deionized water as per manufacturer's instructions, and supplemented with glucose or galactose (10 mM final concentration). The medium was supplemented with $^{57}Fe^{III}$ citrate (^{57}FC) to 3, 10, and 30 μM (final concentrations). Aqueous $^{57}Fe^{III}$ was obtained by dissolving ^{57}Fe metal (Isoflex USA) in a 1:1 mixture of trace-metal-grade HNO_3 and HCl. The solution was diluted to a concentration of 80 mM ^{57}Fe with double-distilled deionized (DDDI) H_2O to prepare a stock solution of ^{57}Fe. ^{57}FC was prepared

by mixing the stock solution with DDDI H_2O, and a 4:1 molar ratio of sodium citrate dihydrate: ^{57}Fe. The pH of the solution was adjusted to 5.0, and the volume adjusted with DDDI H_2O to obtain a final concentration of 40 mM ^{57}FC. $^{57}Fe_2Tf$ (diferric transferrin = ^{57}TBI) was prepared as described [175]. Apo-transferrin (Lee Biosolutions, St. Louis, MO) was dissolved at 10 mg/mL in phosphate-buffered saline (PBS, pH 7.4) containing 0.01 M $NaHCO_3$. Four molar equivalents of ^{57}FC were added per mol Tf. After 4 hr at RT, the solution was centrifuged through a 20 kD MW cut-off membrane (Amicon Ultra 15 mL Concentrator) to remove excess unbound ^{57}FC. The ^{57}TBI-containing retentate (~1 mL) was washed twice with 10 mL of PBS buffer containing 0.01 M $NaHCO_3$, spun through the 20 kD cut-off membrane and re-suspended in PBS buffer (Phosphate Buffered Saline, pH 7.4) at a concentration of 10 mg/mL. ^{57}TBI was added to the cell culture medium affording 3, 10, and 30 μM final concentrations. Whole-cell MB and EPR samples were prepared as described [124].

Total RNA Isolation and cDNA Synthesis

Total RNA was extracted from Jurkat cells using the hot-phenol method [172]. Cells were grown to maximum density (~2.5 × 10^6 cells/mL) in 200 mL of culture medium and harvested by centrifugation at 700×g for 5 min. Cells were washed twice with PBS buffer, re-suspended in 2 mL of AE buffer (50 mM sodium acetate, pH 5.3, 10 mM EDTA) and lysed by adding SDS (1% w/v, final concentration). An equal volume of AE-saturated phenol was added to the cell lysate. The mixture was incubated at 65°C for 10 min and vortexed every 2 min. The mixture was chilled rapidly in liquid N_2 and

spun at 4000×g for 5 min (Beckman Coulter) to separate the phases. The aqueous phase was collected, mixed thoroughly with an equal volume of a 25:24:1 volume-ratio solution of phenol:chloroform:isoamyl alcohol, and spun at 4000×g. The aqueous phase was collected and mixed with 0.1 volumes of 3M sodium acetate and 2.5 volumes of pure ethanol. The solution was spun at 6400 rpm on a Qualitron DW-41 microcentrifuge for 5 min. The RNA-containing pellet was washed 3× with 80% ethanol, allowed to air-dry for 1 hr and re-suspended in 200 μL TE buffer (10 mM Tris, pH 7.5, 1 mM EDTA). Contaminating DNA was removed using the DNA-Free reagent kit (Ambion) as per manufacturer's instructions. cDNA was synthesized from RNA using the Super-Script Vilo cDNA synthesis kit (Applied Biosystems) as per manufacturer's instructions.

Transferrin Receptor-1 (TfRC1) Overexpression

Primers for cDNA amplification of the ORF of the TfRC1 gene were custom-designed (Life Technologies: forward primer: 5'-**CACC**ATGATGGATCAAGCTAGATCAGC-3'; reverse primer: 5'-TTAAAACTCATTGTCAATGTCCCA-3'). Underlined nucleotides were added to the 5' end of the forward primer to enable directional cloning into the pcDNA 3.1 vector (Life Technologies). The TfRC1 gene was amplified from the cDNA using Accuprime Supermix (Life Technologies), along with 300 nM of the forward and reverse primers, as per manufacturer's instructions. PCR product size was determined by electrophoresis at 50 V using a 0.7% agarose gel and visualized using SYBR Green Fluorescent dye. The PCR-product was sequenced using 3 sets of forward and reverse primers that were

complementary to 3 adjacent 800 bp regions of the TfRC1 cDNA ORF sequence. Each 800 bp region was amplified via sequencing PCR, using BigDye Terminator mix (Life Technologies) as per manufacturer's instructions. PCR products were sequenced and analyzed on an ABI PRISM 3100 Genetic Analyzer. The TfRC1 PCR product was directionally cloned into pcDNA 3.1 vector as per manufacturer's instructions (Life Technologies). The resulting plasmid was transformed into OneShot TOP10 *E.coli* competent cells (Life Technologies), which were then plated and grown at 37°C overnight on LB agar plates containing 100 μg/mL of ampicillin. A colony was picked from the plate and grown overnight in liquid LB containing 100 μg/mL of ampicillin. Plasmids were purified from these *E.coli* cells using the PureLink Quick Plasmid Miniprep kit (Life Technologies) as per manufacturer's instructions. The insertion of the TfRC1 gene into the plasmid was verified by performing PCR on the isolated plasmid using the forward and reverse primers (T7 forward and BGH reverse) provided with the pcDNA 3.1 Directional TOPO expression kit (Life Technologies). The sequence of the product cloned into the isolated plasmid was verified as described above.

TREx Jurkat cells were transfected with the TfRC1 plasmid using Lipofectamine 2000 (Life Technologies) as per manufacturer's instructions. Transfected cells were selected by growth for 2 wks on medium containing 1000 μg/mL geneticin. TfRC1 overexpression was verified by Western Blot, using a rabbit anti-TfRC1 primary antibody (Santa Cruz Biotechnology) and an HRP-conjugated anti-rabbit secondary antibody (Life Technologies).

For the iron starvation experiment, cells were first grown in 500 mL of medium to a density of 2×10^6 cells per mL, then spun down and washed once with sterile PBS containing 1 mM EGTA, and then suspended in neat sterile PBS buffer. The cells were spun down again, and resuspended in complete unsupplemented medium containing 100 μM desferrioxamine for 12 hr. The cells were pelleted again, washed with sterile neat PBS buffer, and resuspended again in 1500 mL of complete growth medium supplemented with 3 μM ^{57}TBI. Cells were grown to a maximum density of 3×10^6 cells per mL, and a MB sample was prepared as described [124].

Mitochondria Isolation

Mitochondria were isolated anaerobically from cells grown with 3 and 30 μM FC, as well as from cells grown with 1.5 μM diferric transferrin (i.e. 3 μM TBI) as described [124]. Freshly harvested cells were washed twice with PBS buffer (pH 7.4), then re-suspended in degassed Mitochondria Isolation Buffer (MIB: 225 mM D-mannitol, 75 mM sucrose, 5 mM HEPES, 1 mM EGTA and 1 mM PMSF, pH 7.4). The cell suspension was subjected to N_2-cavitation at 800 psi for 15-20 min using a disruption vessel (model 4635, Parr instruments). The cavitation extract was centrifuged at 800×g for 10 min. The resulting supernatant was centrifuged at 9000×g for 30 min. The pellet was re-suspended in MIB buffer and the resulting solution was layered over a discontinuous gradient of 7.5 mL of 6% Percoll : 3 mL of 17% Histodenz : 3 mL of 35% Histodenz in MIB as described [137]. The gradients were centrifuged at 45000×g for 1 hr.

Mitochondria were collected at the 17-35% interface, washed once with MIB, packed into Mössbauer cups or EPR tubes at 9000×g, frozen and stored in liquid N_2.

Quantitative Western Blots

Whole cell samples were packed into EPR tubes and diluted by a known volume of cell lysis buffer (0.1 M Tris-HCl buffer (pH 7.4) containing 1% Triton X-100 (a non-denaturing detergent) and 1 mM PMSF). Protein concentrations were determined using the BCA Protein Assay kit (Thermo Scientific Pierce Protein Research Products). Various known amounts of human holo-ferritin (Lee Biosolutions, St. Louis, MO) were loaded and separated on a 7.5% polyacrylamide native gel, along with 20 μL of cell lysates from cells grown in glucose or galactose-containing medium supplemented with 3 μM, 10 μM, or 30 μM of either FC or TBI. Proteins were transferred to Immun-Blot PVDF membranes (Bio-Rad) overnight at 40 V. Membranes were treated for 2 hr with Blocker casein solution (Thermo Scientific), then incubated for 1 hr with rabbit monoclonal primary antibody specific to mammalian ferritin (Abcam) diluted 1:1000 in Blocker casein solution. Membranes were then incubated with goat anti-rabbit HRP conjugated secondary antibody (Life Technologies) diluted 1:3000 in Blocker casein solution, followed by detection using the Thermo Scientific Enhanced Chemiluminescent Western Blotting substrate. Images were acquired using the FujiFilm LAS-4000 mini imager. Ferritin bands were analyzed using MultiGauge software. A calibration curve was generated using the intensities of the human holo-ferritin bands. Ferritin concentrations of various cell lysates were quantified in terms of absolute

cellular concentrations by accounting for the dilution factors and employing the packing efficiency of Jurkat cells that was determined previously [124].

Biophysical Studies

EPR spectra of whole cells and isolated mitochondria were acquired using an X-band EMX spectrometer (Bruker Biospin Corp., Billerica, MA) equipped with an Oxford Instruments ER900A cryostat. Spin quantifications were performed with SpinCount (http://www.chem.cmu.edu/groups/hendrich/facilities/index.html), using 1.00 mM $CuSO_4$-EDTA as a standard. MB spectra were collected on a model MS4 WRC spectrometer and a model LHe6T spectrometer, capable of generating 0-6 T fields (SEE Co., Edina, MN). Both instruments were calibrated using the spectrum of α-Fe foil collected at room temperature.

For UV-visible spectroscopy, packed whole cell and mitochondrial samples from EPR tubes were diluted 2-fold with PBS buffer and MIB buffer respectively, placed in a custom 2 mm pathlength quartz UV-vis cuvette (Precision cells) and sealed with a rubber septum. Spectra were collected on a Hitachi U3310 spectrometer with a Head-on photomultiplier tube. Heme signals were simulated using OriginPro as described. [119]

Ferritin Loading with Fe^{II} Sulfate in Whole-Cell Lysates

After collecting Mössbauer spectra of Jurkat cells grown with 30 μM ^{57}FC, the sample was thawed at RT and re-suspended homogenously in an equal volume of non-denaturing cell lysis buffer containing 1 mM of PMSF. The lysate was split into two; to

half was added $^{56}Fe^{II}$ sulfate in aqueous solution to a final concentration of ~ 6.25 mM; the other half was left untreated. Both samples were exposed to air and mixed regularly for 2 h. Each sample was placed in a 3 mL Mössbauer cup and frozen immediately in liquid N_2.

Electron Microscopy and EDX Imaging

Cells were pelleted at 700×g for 10 min and washed 3 times with RPMI 1640 medium. Cells were fixed overnight with acrolein vapor, dehydrated for 2 days with ethylene glycol, infiltrated and embedded in epoxy resin by polymerization at 60 °C overnight. Ultrathin sections were obtained using an Ultracut E microtome (Reichert-Jung). Sections were carbon-stabilized overnight. Elemental analysis was performed on a TECNAI F20 Twin (scanning) transmission electron microscope ((S)TEM) fitted with a Schottky field emission gun, a high-angle-annular-dark-field (HAADF) detector, and an Oxford instruments ultrathin window energy-dispersive-X-ray spectroscopy (EDX) detector. EDX spectra were collected at a ~ 15^{o} tilt angle with a stationary electron probe in STEM mode. The STEM was operated at a 200 kV accelerating voltage. Spectral images were obtained from areas of interest by the electron-microscope-spectroscopy system. Elemental maps were acquired after choosing proper energy windows for element-specific transitions along with STEM-HAADF images.

Extracellular Flux Measurements

Cells were grown in RPMI 1640 medium containing 10 mM glucose or galactose, 5% Newborn Calf Serum (Invitrogen), 10 μM FC, 100 units/L penicillin, 100 μg/L streptomycin, and 0.25 μg/L amphotericin B. Cells were spun at 700g for 5 min and the pellet was washed with PBS buffer (pH 7.4). Cells were re-suspended in Modified DMEM XF Assay medium (Seahorse Biosciences, Billerica, MA) supplemented with either 10 mM glucose or 10 mM galactose. Cell-Tak™ (BD Biosciences), a cell and tissue adhesive, was diluted in 0.1 M sodium bicarbonate buffer (pH 8.0) as per manufacturer's instructions and used to coat the wells of a 24-well plate (Seahorse) by adding ~4 μg of Cell-Tak™ in a total volume of 50 μL per well. O_2 consumption (OCR) and extracellular acidification rates (ECAR) were measured on the Extracellular Flux Analyzer (XF24) (Seahorse Biosciences) as described [176] with minor modifications. Briefly, Jurkat cells were seeded in Cell-Tak™ treated XF24-well cell culture microplates at 250,000 cells/well in 10 mM glucose- or 10 mM galactose–containing XF assay media and incubated at 37°C for ~1 hr prior to measurements. The baseline was measured 3 times prior to adding oligomycin (1 μM final concentration); the data presented here represent the third measurement. Each measurement included a mix (2 min), wait (3 min) and measure (2 min) cycle.

Oxyblot Assays

Whole-cell lysates were prepared in cell lysis buffer (0.1 M Tris-HCl, 1% Triton X-100, 1 mM PMSF). Twenty μg of cellular protein from each extract was solubilized

with 10% w/v SDS, derivatized with 2,4-dinitrophenylhydrazine (DNPH) and loaded onto a 12% SDS-PAGE gel. Oxyblot analysis was performed using the DNPH-primary antibody and the HRP-conjugated secondary antibody provided with the manufacturer's kit (Millipore).

ICP-MS

Packed whole cells and mitochondrial samples from EPR tubes were diluted with a known volume of PBS buffer and MIB buffer respectively. Suspensions were digested overnight with concentrated trace-metal-grade nitric acid (final concentration 20-30%) in 15 mL plastic screw-top tubes (BD Falcon). Digested samples were diluted with 4 mL of double-distilled and deionized water. Metal concentrations were measured in H_2 and He collision modes using ICP-MS (Agilent Technologies model 7700x). The absolute metal concentrations in the samples were obtained by adjusting for dilution factors and packing efficiencies, and then averaging individual numbers.

Frataxin Knockdown

Frataxin protein knockdown was performed using the BLOCK-iT Inducible H1 RNAi Entry Vector kit (Life Technologies) as per manufacturer's instructions. Four DNA oligonucleotide sequences encoding shRNA sequences specific to frataxin mRNA were designed using Life Technologies' BLOCK-iT™ RNAi Designer (rnaidesigner.invitrogen.com/rnaiexpress/) and cloned into pENTR™/H1/TO vector (Life Technologies). The plasmids were separately transformed into One Shot® TOP10

chemically competent *E. coli* cells, which were plated and selected on LB agar plates with 50 μg/mL kanamycin. Bacterial colonies were picked and grown in liquid LB with 50 μg/mL kanamycin. Plasmids were purified from the liquid cultures using PureLink™ HQ Mini Plasmid Purification kit (Life Technologies) as per manufacturer's instructions. Plasmids were transfected into Jurkat cells using Xfect™ transfection reagent (Clontech) as per manufacturer's instructions. Cells were grown under selection for 2-3 weeks in RPMI-1640 medium supplemented with tetracycline-negative fetal bovine serum (PAA Laboratories), 10 μg/mL blasticidin, and 50 μg/mL Zeocin. After selection, frataxin knockdown was induced by adding tetracycline to a final concentration of 3 μg/mL in the cultures. Transfected cells were allowed to grow in the presence of tetracycline for 4-5 days before being assayed for frataxin knockdown.

To assay for frataxin knockdown, transfected cells (both uninduced and induced) were grown to a maximum density of 2×10^6 cells/mL. Cells were spun down, washed with PBS buffer, and lysed using ice-cold RIPA buffer (RadioImmunoprecipitation Assay Buffer: 50 mM Tris HCl, 150 mM NaCl, 1% Triton X-100, 0.5% sodium deoxycholate, 0.1% SDS, pH 8.0). Protein concentrations of cell lysates were determined using Pierce BCA Protein Assay Kit (Thermo Fisher Scientific) as per manufacturer's instructions. Forty μg of protein was boiled with denaturing Laemmli buffer and loaded on a 10% polyacrylamide gel. SDS-PAGE was carried out at 100 V, and proteins were transferred to Immunblot-PVDF membranes for 16 hr at 20 V. Membranes were blocked for 2 hr using Blocker Casein solution (Thermo Fisher Scientific). Membranes were then incubated (with shaking) in rabbit polyclonal anti-

frataxin primary antibody (Abcam) diluted 1:500 in PBS buffer. Membranes were subsequently rinsed 3× with PBS buffer, and incubated with goat anti-rabbit HRP conjugated secondary antibody diluted 1:3000 in PBS buffer. Membranes were again rinsed 3× with PBS buffer, and immersed in Pierce ECL Western Blotting substrate (Thermo Fisher Scientific). Frataxin bands were detected using FujiFilm LAS-4000 mini imager. The frataxin band intensities were analyzed by densitometry using ImageJ software. The DNA oligonucleotide encoding the shRNA sequence 5'-GGACTATGATGTCTCTTTGG**CGAAC**CAAAGGAGACATCATA-3' (loop region indicated in bold), which targets bases 583-603 of frataxin mRNA, resulted in 50%-70% knockdown of frataxin protein after 4-5 days of induction by tetracycline, as judged by densitometry analysis of frataxin bands. The remaining shRNA sequences tested did not result in measurable frataxin knockdown. Therefore, the cells expressing the shRNA targeted to bases 583-603 were chosen for further analysis.

For spectroscopic investigations, transfected cells expressing shRNA targeted to frataxin were grown up to 3 L in complete RPMI-1640 medium supplemented with 50 μg/mL Zeocin, and 10 μg/mL tetracycline to ensure continuous frataxin knockdown. ^{57}FC was added to a final concentration of 10 μM to the cell culture. Cells were washed with PBS containing 1 mM EGTA, followed by PBS without EGTA, packed into MB cups, and flash-frozen in liquid N_2. After MB analysis, cells were thawed and analyzed by UV-Vis spectroscopy and ICP-MS as described before. WT cells grown with 10 μM ^{57}FC were analyzed alongside the transfected cells for comparison.

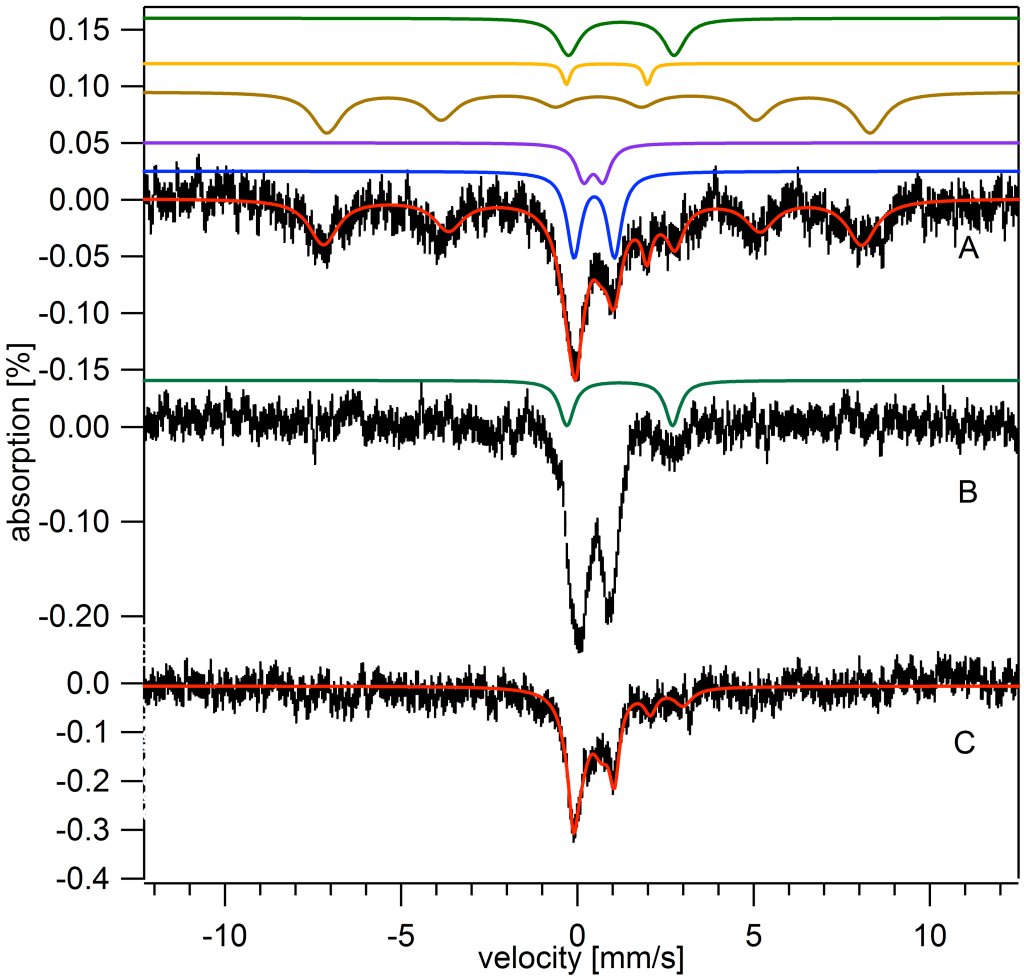

Figure 3-1. Mössbauer spectra of Jurkat cells grown in medium supplemented with 3 μM $^{57}Fe^{III}$ citrate. A, 3 μM FC at 5K, 0.05 T; B, same as A but at 70 K. Simulations are as follows: CD (blue, δ = 0.46 mm/s; ΔE_Q = 1.2 mm/s), ferric nanoparticles (purple, δ = 0.48 mm/s and ΔE_Q = 0.57 mm/s), ferritin (brown, δ = 0.54 mm/s; ΔE_Q = 0.20 mm/s; H_{eff} = 480 kG), HS Fe^{II} hemes (orange, δ = 1.00 mm/s; ΔE_Q = 2.00 mm/s), and NHHS Fe^{II} (green, δ = 1.30 mm/s; ΔE_Q = 3.00 mm/s) C, 5 K, 0.05 T MB spectrum of isolated mitochondria from cells grown with 3 μM FC. Total simulations for A and C are shown in red.

Results

3 μM ^{57}FC-Grown Cells

To evaluate the essential Fe content of human cells, we prepared cells under Fe-limited conditions. However, the concentration of natural abundance endogenous Fe in the medium was substantial (~ 6 μM [124]). Unlike yeast cells that can be grown in chemically-defined minimal synthetic medium, human cells require fetal bovine or newborn calf serum which contains significant amounts of Fe. Grown in such unsupplemented medium, Jurkat cells contained 100 ± 20 μM of Fe. These cells grew at about the same rate as when grown in medium supplemented with 3 – 30 μM ^{57}FC, namely with a doubling time (DT) of 24 hr. This indicates that growth was not limited by the endogenous Fe content of the unsupplemented medium.

We attempted to reduce the concentration of endogenous Fe by adding (in different batches) desferrioxamine (DFO) and bathophenanthroline sulfonate (BPS), well-known chelators of Fe^{III} and Fe^{II} ions, respectively. Similar procedures have been used to create Fe-deficient conditions in yeast [171]. However, Jurkat cells did not grow in the presence of 100 μM DFO or BPS, which disallowed further analysis of cells subjected to Fe-deficient conditions.

For MB studies, we grew cells in medium supplemented with as little as 3 μM ^{57}FC (Figure 3-1). Although not strictly Fe-deficient, this Fe concentration was significantly lower than used in our previous investigation [124].

Table 3-1. Iron-related properties of Jurkat cells. Cellular states are designed by the nomenclature #AB where # indicates the concentration of Fe supplementing the growth medium, with values 0, 3, 10, 30 or 100 μM, A indicates whether the Fe was TBI (T) or FC (F), and B indicates whether the medium used glucose (U) or galactose (L) as the carbon source. WT indicates normal cells, $TfRC^+$ indicates cells overexpressing TfRC1, and $Frxn^-$ indicates frataxin-deficient cells. Replicates *n* are given in parentheses where applicable. The concentration of endogenous Fe was assumed to be 4-6 μM, and was added to the concentration of ferric citrate. For all simulations, K_{Ic} = 9 μM; *cs* = 3; K_{Im} = 120 μM; K_{If} = 130 μM; k_t = 0.3 hr^{-1} (except for 3TU "starved" cells for which k_t = 3 hr^{-1} and $TfRC^+$ cells for which k_t = 1.8 hr^{-1}), k_m = 0.27 hr^{-1}; k_f = 0.55 hr^{-1}; k_{np} = 0.000045 $\mu M^{-1.9}$ hr^{-1}, and *p* = 2.9. Values for k_r are given in the table. The unusually high value of k_r for 3TU "starved" cells suggests that the receptor for FC was also upregulated during the "starving" step of the experiment. α = 1/24 hr^{-1} for all simulations except for 10FL and 30FL, in which case α = 1/34 hr^{-1}, and for $Frxn^-$ cells where α = 1/30 hr^{-1}. For 20FU (1:4), the sample was diluted into medium without Fe supplementation and allowed to grow for 2 doublings. To simulate this, the initial Fe concentrations were set to those obtained for 20FU before dilution, and final Fe concentration were recorded at t = 48 hr. Read the table as we illustrate with the row beginning with 3FU, WT and the next row labeled "sim". The upper row indicates the data while the lower row indicates the simulation. The overall concentration of FC in the experiment includes the 3 μM ^{57}Fe that was added to the medium plus 6 μM endogenous Fe. No TBI was added. The rate-constant k_r used in the simulation was 1.0 hr^{-1}. The cellular Fe concentration was 220 ±

Table 3-1 (Continued)

65 μM (average of 3 experiments) while the simulation afforded a concentration of 216 μM. The concentration of ferritin protein in one of the samples was 0.3 μM, with an average loading of 380 Fe's per ferritin. The next 5 columns indicate the percentage of Fe in the sample due to particular groups of Fe centers in the sample (based on MB quantification) followed, after the comma, by the absolute concentration of that group of species (obtained by multiplying the percentage by $[Fe_{cell}]/100$). Simulated analogous values are given in the row below. Two of the groups (Fe/S clusters + LS hemes combined with HS Fe^{II} hemes) were collectively viewed as "mitochondrial Fe_m" by the model. Thus, to compare the data and simulations for this category, add the two percentages in the data row (25% + 5% = 30%) and compare it to the percentage in the simulation row (38%). Likewise, compare the sum of absolute concentrations (55 μM + 11 μM = 66 μM) in the data row to 82 μM in the simulation row. In the remaining 4 columns, the experimental and simulated percentages and absolute concentrations can be compared directly. For the $Frxn^-$ cells, the concentration of nanoparticles includes both those in the cytosol (Fe_n) and those in the mitochondria (Fe_{mp}).

Table 3-1 (Continued)

Sample	[FC] (μM)	[TBI] (μM)	k_r (hr^{-1})	[Fe_{cell}] (*n*)	[Ferritin Protein], Fe/Ferritin	Fe/S+LS Hemes %, μM	HS Fe^{II} hemes %, μM	Ferritin [Fe_f] %, μM	NHHS Fe^{II} [Fe_c] %, μM	Nano-particles [Fe_n] %, μM
0U, WT	0 + 6 = 6	0		100 ± 3 (*1*)	---,---	---	---	---	---	---
sim	4	0	0.8	105		31, 33= [Fe_m]		64,67	5,5	0,0
3FU, WT	3 + 6 = 9	0		220 ± 65 (*3*)	0.3, 380	25,55	5,11	52,114	13,29	5,11
sim	9	0	1.0	216		38, 82		55,119	13,6	1,2
10FU, WT	10 + 6 = 16	0		400±70 (*5*)	0.3, 530	27,108	4,16	40,160	11,44	18,72
sim	16	0	1.0	384		32,124		38,146	12,45	18,69
30FU, WT	30 + 6 = 36	0		840±276 (*3*)	0.4, 275	13,109	2,17	13,109	7,60	65,546
sim	36	0	1.0	865		16,135		18,157	10,89	56,483
100FU, WT	100+6 = 106	0		3700±200 (*2*)	0.5,---	5,185	---	---	---	93,3440
sim	106	0	1.3	3307		4,144		5,167	5,163	86,2833
3TU, WT	0+6= 6	3		142±24 (*3*)	0.6,95	40,57	---,---	40,57	---,---	---,---
sim	5	3	1.1	145		32,46		63,92	5,7	0,0
10TU, WT	0+6= 6	10		160±20 (*2*)	0.8,80	40,64	---	40,64	---	---
sim	5	10	1.1	170		33,56		61,104	5,9	0,1
30TU, WT	0+6= 6	30		225±25 (*3*)	0.4,300	30,68	2,5	54,122	8,18	6,14
sim	5	30	1.1	209		37,78		56,117	6,12	1,2
3FL, WT	3+6= 9	0		130±6 (*2*)	0.4,115	35,46	2,3	35,46	11,14	14,18
sim	8	0	0.8	218		39,86		56,121	5,10	0,1
10FL, WT	10+6 =16	0		580±160 (*2*)	0.4,290	26,151	2,12	20,116	13,75	38,220
sim	16	0	1.1	598		23,135		26,157	10,62	41,244
30FL, WT	30+6 =36	0		2000±300(*2*)	1.2,167	10,200	---,---	10,200	---,---	79,1580
sim	36	0	1.3	1591		9,143		10,165	7,107	74,1176
3TU,TfR^+	0+6= 6	3		400±29 (*2*)	0.5,480	25,100	3,12	60,240	6,24	2,8
sim	6	3	1.2	302		38,115		46,138	10,29	7,20
10TU, TfR^+	0+6= 6	0		510±14 (*2*)	0.7,290	25,127	2,10	40,204	3,15	30,153
sim	6	0	1.0	528		25,130		29,151	12,63	35,183
20FU, WT	20+6 =26	0		675±33 (*2*)	---	20,135	2,14	20,135	4,27	45,304
sim	26	0	1.1	686		19,133		22,154	11,77	47,322
20FU (1:4), WT	0+6= 6	0		225±8 (*1*)	---	37,83	2,5	45,90	10,23	3,7
sim	6	0	1.1	229		30,69		45,104	3,8	21,48
3TU (starved) WT	0+6= 6	3		330±5 (*1*)	---	19,63	2,7	50,165	16,53	13,43
sim	5	3	2.6	328		36,119		43,141	11,35	9,31
10FU ($Frxn^-$)	10+6 =16	0	---	550±36 (*2*)	---	28,154	3,17	20,110	5,28	40,220
sim	16	0	1.1	528		12,64		27,146	7,37	53,281

The 5 K 0.05 T MB spectra of such cells (Figure 3-1A) was dominated by a sextet which collapsed into a doublet at 70 K (Figure 3-1B). This behavior and the apparent hyperfine splitting of the sextet (H_{eff} = 480 kG) and MB parameters for the resulting doublet (δ = 0.55 mm/s, ΔE_Q = 0.25 mm/s) are typical of ferritin. We have assigned this feature as such (see Table 3-1 for a list of Fe-containing species found in these cells). Fe-bound ferritin represented about half of the Fe in the sample (52% of 220 μM = 114 μM). Assuming that this storage form of Fe is unnecessary for cellular metabolism, the remaining ~ 100 μM Fe in these cells matches the concentration of Fe in cells grown on unsupplemented medium. We suggest that *Jurkat cells require ~ 100 μM cellular Fe for normal growth*; this is the concentration of essential Fe in these cells.

The non-ferritin forms of Fe evident in the spectra of these cells included the central doublet (CD) and non-heme high-spin (NHHS) Fe^{II} doublet. The CD primarily includes the S = 0 $[Fe_4S_4]^{2+}$ clusters and HS Fe^{II} hemes found in mitochondrial respiratory complexes. This doublet represented ~ 25% of the intensity (55 μM) of the 5 K low-field MB spectrum of Figure 3-1A. At 70 K the ferritin sextet collapsed, revealing the high-energy line of a NHHS Fe^{II} doublet (simulated by the green line in Figure 3-1B). The NHHS Fe^{II} doublet represented 13% of spectral intensity, which corresponds to *ca*. 30 μM Fe^{II} ions. The observed spectral parameters (δ = 1.30 mm/s, ΔE_Q = 3.00 mm/s) are typical of Fe^{II} ions coordinated primarily by O and N ligands. These two species (the CD and NHHS Fe^{II}) represent the majority of the essential Fe in Jurkat cells. Interestingly, Fe-deficient yeast cells which also contained only essential Fe exhibited significant contributions from the same two components [171]. Although the function of the

NHHS Fe^{II} ions in yeast has not been established, most of it was not located in mitochondria.

The concentration of the ferritin protein complex in 3 μM ^{57}FC-grown cells was determined by quantitative Western blotting (Figure 3-2, Table 3-1) to be 0.3 μM, indicating an average of 400 Fe atoms per ferritin complex (114 μM Fe/0.3 μM ferritin). Populations of purified ferritin complexes afford binomial-like Fe-loading distributions [177, 178], and we interpret our results similarly for *in vivo* ferritin populations.

We isolated mitochondria from 3 μM ^{57}FC-grown cells. The Fe concentration of the organelle was low (280 μM) compared to mitochondria isolated from 10 μM ^{57}FC-grown cells [124]. Also, the corresponding 5 K low-field MB spectrum (Figure 3-1C) was weak. Nevertheless, the CD doublet clearly dominated the spectrum, corresponding to at least half of the total intensity. The degree of resolution between the two legs of the CD indicated that the level of Fe^{III} nanoparticles in the sample was low. HS Fe^{II} heme and NHHS Fe^{II} species contribute quadrupole doublets with well-defined δ and ΔE_Q values. Such doublets at *ca*. 5% intensity for each can easily be fitted in the spectrum of Figure 3-1C (this is not conclusive evidence that such material is present, given the noise). Isolated mitochondria did not exhibit significant levels of a ferritin-like sextet. A minor ferritin-like feature could be distinguished from the baseline, but whether it arose from mitochondrial ferritin or a contaminant of cytosolic ferritin could not be determined (we suspect the latter).

The lack of a significant NHHS Fe^{II} doublet in the spectrum of isolated mitochondria indicates that the bulk of the associated NHHS Fe^{II} species observed in our

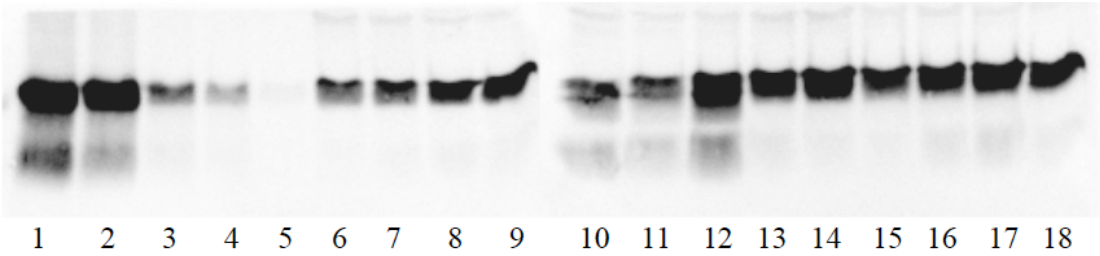

Figure 3-2. Quantitative Western blot of ferritin in cell lysates. The lanes given in parentheses were loaded with (1) 1000, (2) 500, (3) 100, (4) 50 and (5) 10 ng of holo-ferritin. The following lanes were loaded with 10 µL of lysates: (6) 3FU, (7) 10FU, (8) 30FU, (9) 100FU, (10) 3FL, (11) 10 FL, (12) 30FL, (13) 3TU, (14) 10TU, (15) 30TU, (16) 3TU $TfRC^+$, (17) 10TU $TfRC^+$, (18) 30TU $TfRC^+$.

whole cell spectrum was located in one or more non-mitochondrial regions of the cell (assumed for this study to be the cytosol). This is similar to the Fe content of Fe-deficient yeast cells [171]. In a previous study [124], we showed that the equation

$$[Fe]_{cell} - [Fe]_{ferritin} = [Fe]_{mito}\frac{V_{mito}}{V_{cell}} + [Fe]_{other}\left(1 - \frac{V_{mito}}{V_{cell}}\right)$$

followed from the conservation of matter and that $V_{mito}/V_{cell} \sim 0.2$ for Jurkat cells. Along with the concentrations obtained in the current study for 3 μM FC-grown cells, this relationship and ratio suggest that *ca*. 50 μM of Fe in these cells (primarily the NHHS Fe^{II} species) is found in regions other than mitochondria (e.g. the cytosol).

Equivalent samples of whole cells and their isolated mitochondria were characterized by EPR (Appendix II, Figure A5 and A6) and UV-vis (Appendix II, Figures A7 and A8) spectroscopies. EPR signals were weak, consistent with the low concentration of EPR-active Fe in these cells. Spectra included signals in the high-field and g = 2 regions. Observed resonances at g = 6.3 and 5.4 were assigned to the mixed-valence state (Heme a_3 Fe^{III} Cu_b^{I}) of the cytochrome *c* oxidase active-site [124]. The g = 4.3 signal was assigned to HS Fe^{III} species with rhombic symmetry. The g = 2 region included signals at g = 2.00 due to an unidentified organic radical, and at g_{ave} = 1.94 and 1.90 (due primarily to mitochondrial respiratory complexes). The standard set of Fe^{II} heme UV-vis features were observed for all the whole cell and isolated mitochondria samples. Our analysis of these EPR and UV-Vis spectral features indicated that they were similar in concentration as observed in 10 μM FC-grown cells studied previously [124].

30 μM ^{57}FC-Grown Cells

We next analyzed cells grown in medium supplemented with 30 μM ^{57}FC. Such cells contained nearly 4-times more Fe than those grown with 3 μM ^{57}FC (Table 3-1) and 2-times more Fe than cells grown with 10 μM FC [124]. The corresponding 5 K low-field MB spectrum (Figure 3-3A) was dominated by a broad quadrupole doublet with parameters typical of Fe^{III} oxyhydroxide nanoparticles (δ = 0.48 mm/s, ΔE_Q = 0.57). This doublet represented 65% of the Fe in the sample and corresponded to ~ 550 μM Fe (65% of 840 μM total Fe). Nanoparticles were also present in cells grown on 10 μM ^{57}FC, but their concentration was 7-fold less.

The MB spectrum of 30 μM ^{57}FC cells also exhibited a ferritin-based sextet. Although barely distinguishable from baseline, the sextet represented *ca*. 13% of the Fe in the sample (0.13 × 840 μM = 109 μM). This concentration was almost the same as that of ferritin Fe in 3 μM FC-grown cells. Quantitative Western blotting (Figure 3-2) indicated ~ 0.4 μM ferritin protein in the sample, again suggesting partial Fe loading (109 μM/0.4 μM ≈ 300 Fe/ferritin). A similar analysis of 10 μM ^{57}FC-grown cells also indicated partial ferritin loading (160 μM/0.3 μM ≈ 500 Fe/ferritin). The uncertainty in these determinations was such that loading ratios are considered to be basically invariant for most conditions measured, with an average of 400 ± 100 Fe/ferritin (3 and 10 μM TBI-grown cells have even lower loading ratios).

The Fe associated with ferritin and nanoparticles collectively accounted for all but 185 μM Fe in the 30 μM ^{57}FC-grown cells. Nanoparticles and ferritin-bound Fe

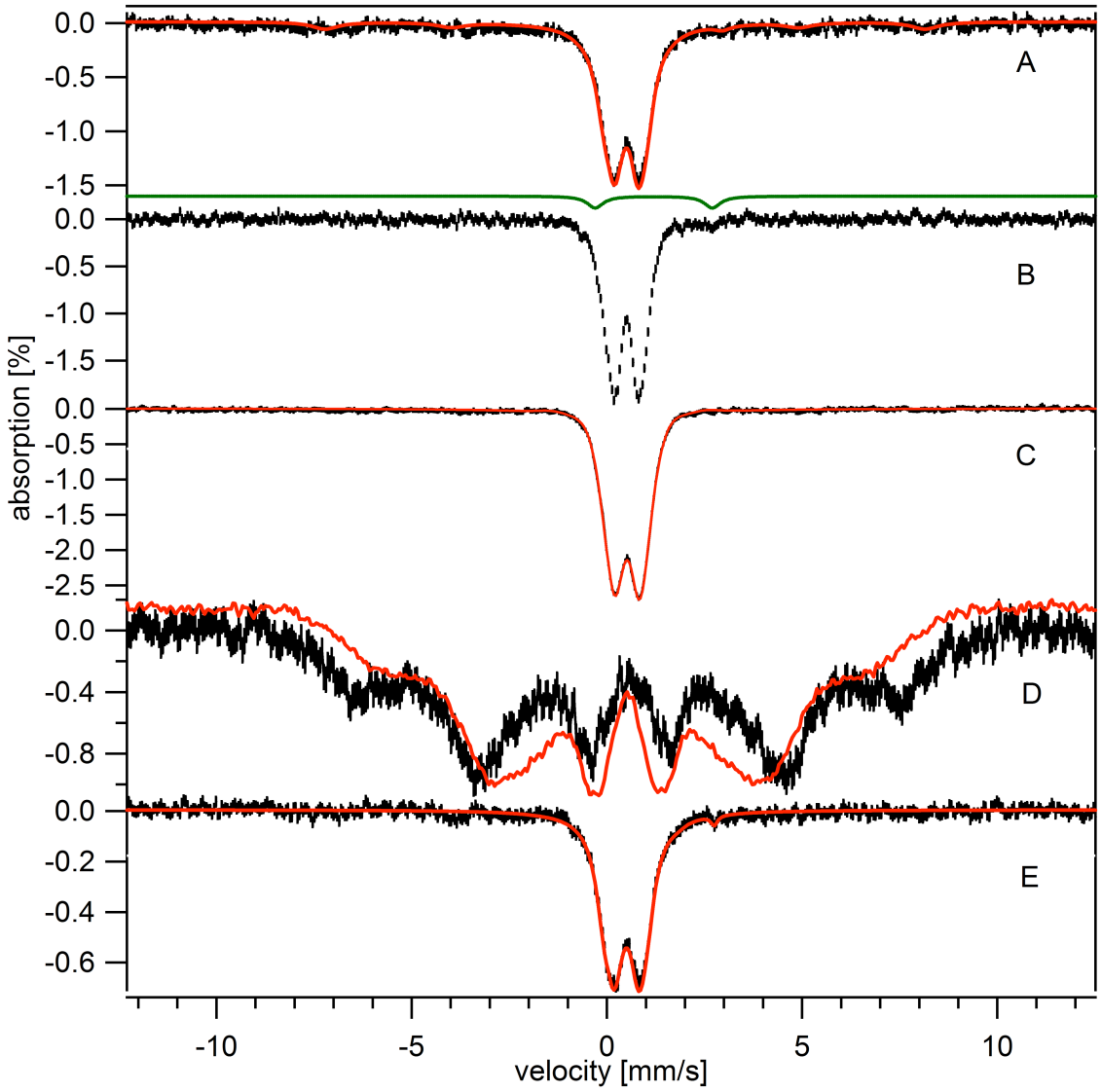

Figure 3-3. Mössbauer spectra of high-Fe Jurkat cells and mitochondria. A, 30FU, 5K, 0.05T; B, 30FU, 70K, 0.05T; C, 100FU, 5K, 0.05T; D, 100FU, 4.3K, 6T, overlaid with a 6T, 4.3 K spectrum (red) of yeast mitochondria isolated from Aft1-1^{up} cells [120]; E, 5K, 0.05T spectrum of mitochondria isolated from cells grown on glucose with 30 μM FC. Overall simulations for A and D are shown in red.

probably do not contribute to cellular physiology; the majority of the remaining Fe is probably due to the essential Fe described above. The CD in the 5 K MB spectrum (Figure 3-3A) could not be cleanly resolved from the nanoparticles doublet; however, subtracting various percentages of a doublet fixed with CD parameters from the unresolved nanoparticle-dominated feature suggested that 10 - 15% of the spectral intensity (100 - 130 μM) was due to the CD. At 70 K, the ferritin sextet collapsed into a doublet revealing a NHHS Fe^{II} doublet (green line in Figure 3-3B) that corresponded to *ca.* 7% of spectral intensity (60 μM Fe^{II}). These two features, the CD and NHHS Fe^{II}, undoubtedly represented much of the essential Fe in the sample. Somewhat lower concentrations of these two species were observed in the 3 μM FC-grown sample.

The extent of nanoparticle formation scaled nonlinearly with the concentration of Fe in the medium. Cells were grown in 100 μM ^{57}FC to maximize formation of these particles; such a sample was characterized by MB spectroscopy at 5 K and 0.05 T (Figure 3-3C). These cells accumulated 3.5 - 4 mM total Fe, > 90% of which was in the form of nanoparticles. The corresponding 6 T spectrum (Figure 3-3D, black hashmarks) was dominated by a broad magnetic feature suggesting superparamagnetic behavior. This spectrum was compared to that of previously-characterized Fe^{III} oxyhydroxide phosphorous-associated nanoparticles from the Aft1-1^{up} yeast strain [172] (Figure 3-3D, red line). Spectral features were similar but not identical, indicating a different distribution of hyperfine coupling constants. These magnetic differences must correspond, at some level, to structural differences.

MB spectra of mitochondria isolated from 30 μM ^{57}FC-grown cells were also dominated by nanoparticles (Figure 3-3E). Approximately 690 μM Fe in these isolated organelles originated from nanoparticles whereas the concentration of nanoparticles in corresponding whole cells was ~ 550 μM. Since mitochondria occupy ~ 20% of the cell's volume, we would expect that if all nanoparticles in the cell were present in these organelles, the concentration of nanoparticles in isolated mitochondria would be ~ 2.7 mM Fe (5× more than observed). Furthermore, upon increasing the FC concentration from 10 to 30 μM in the medium, the whole-cell Fe concentration doubled, but the Fe concentration associated with isolated mitochondria did not change significantly. These considerations imply that the extra Fe in the 30 μM FC-grown cells (primarily nanoparticles) accumulated in one or more non-mitochondrial regions of the cell, possibly the cytosol.

Although the concentration of Fe in 30 μM FC mitochondria was similar to that of 10 μM FC mitochondria [124], the MB distribution of that Fe was different. Mitochondria from the 30 μM FC-grown cells exhibited a significant decrease in absolute concentration of ferritin-like Fe, HS Fe^{II} hemes, and NHHS Fe^{II}, as well as a significant increase in nanoparticles (Table A5, Appendix I). The diminished amount of ferritin-like Fe may be irrelevant given that ferritin is cytosolic. The difference in ferritin-like material is probably the consequence of small-number-variations (we prepared two batches at each concentration) and less contamination in the 30 μM FC samples. UV-vis analysis of these samples exhibited similar levels of cytochromes

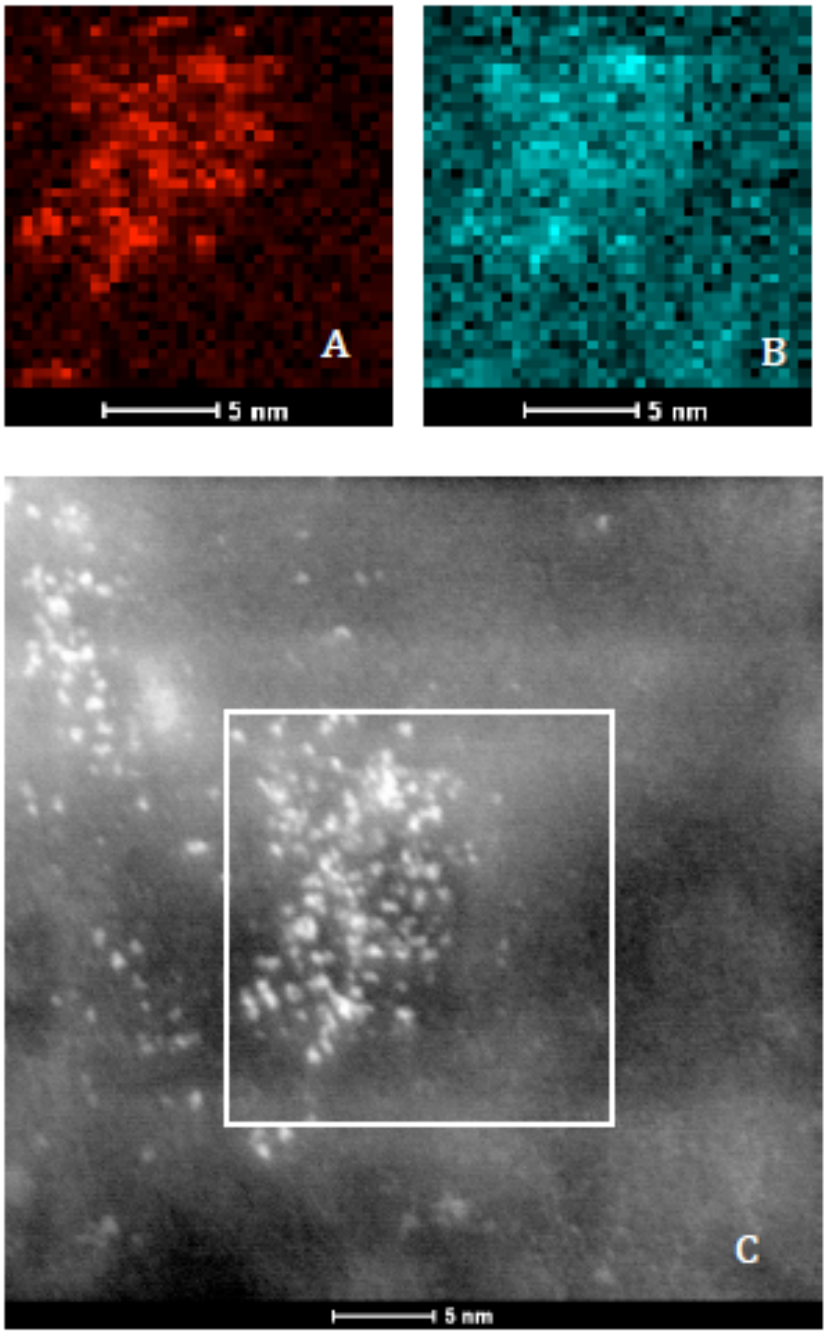

Figure 3-4. EDX images of glucose-grown cells in medium containing 30 μM FC. A, Fe map; B, P map; C, 320K magnified image of Fe deposits. The box in C indicates the region in which the elemental maps were obtained.

(Figure A8, Appendix II). EPR spectra were also determined for cells grown on 3 and 30 μM FC. The same group of signals, with similar intensities, was observed as for the 10 μM FC sample [124]. The spectral intensities of the CD component of MB spectra were similar for the samples. These characteristics, considered collectively, suggest that the concentrations of respiratory complexes in the mitochondria isolated from 3, 10, and 30 μM FC-grown cells were approximately the same. The major difference was the presence of more nanoparticles in the 30 μM FC-grown cells.

We were initially concerned that the doublet attributed to nanoparticles in these cells actually represented ferritin loaded with small amounts of Fe (≤ 10:1 Fe:Ferritin ratio). At ~ 4 K, such species exhibit quadrupole doublets rather than a sextet [73]. We reasoned that if the superparamagnetic doublet actually arose from poorly-loaded ferritin, adding an excess of Fe^{II} under aerobic conditions would load the ferritin, causing the doublet to disappear and the sextet to appear. However, the results (Figure A4, Appendix II) did not show such a shift, indicating that the majority of the broad doublet arose from nanoparticles rather than from poorly-loaded ferritin.

EDX EM imaging of cells grown with 30 μM FC revealed ~ 1 nm diameter particles in what appears to be the cytosol (Figure 3-4C). Elemental mapping revealed that these particles were associated with both Fe and P in approximately a 1:1 molar ratio (Figures 3-4 A-B and Appendix II, A3). Results for O were ambiguous due to strong background levels of O in the cytosol and/or in the embedding medium. Such nanoparticles were not detected by EDX imaging in cells grown in medium containing 3 μM TBI or FC.

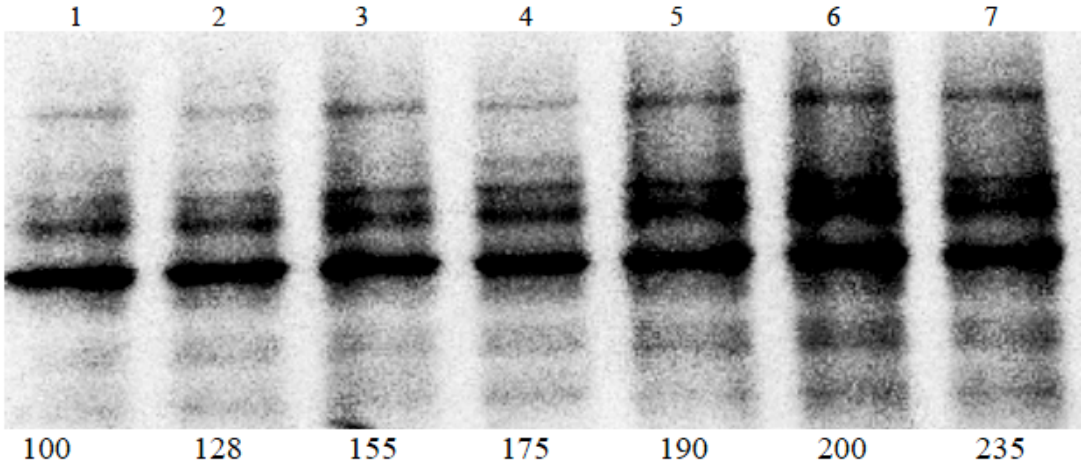

Figure 3-5. Oxyblot analysis of cells grown under different conditions. Samples include (with lanes in parentheses) (1) 3FU; (2) 10FU; (3) 30FU; (4) 100FU; (5) 3FL; (6) 10FL; (7) 30FL. Percentages of intensities relative to lane 1 are designated below each lane.

Oxidative Damage in Glucose-Grown Cells

In yeast cells, nanoparticle formation is reportedly associated with oxidative damage [117, 139]. To investigate whether nanoparticle formation is associated with oxidative damage in human cells, we performed an Oxyblot analysis on Jurkat cells grown on 3, 10, 30 and 100 μM FC (Figure 3-5, lanes 1 - 4). In this experiment, the level of oxidative damage increased slightly as the FC and nanoparticle levels increased. In another experiment (Figure A9, Appendix II), there was no correlation between ROS and Fe level. We conclude that there is little, if any, effect of nanoparticle formation on ROS levels in glucose-grown Jurkat cells.

Bioavailability of Nanoparticles

We wondered whether cells can utilize the Fe in nanoparticles. Cells were overloaded with nanoparticles (by growth in 20 μM ^{57}FC medium) and then transferred to unsupplemented medium. They were grown to maximum density, and a portion was used to prepare a MB sample. Remaining cells were washed once with PBS containing 1 mM EGTA (to remove excess Fe), followed by another wash with PBS buffer lacking EGTA. The cells were diluted 4-fold in unsupplemented medium, allowed to grow to maximum density (two doubling times), and then harvested. The cells grown on 20 μM ^{57}FC accumulated significant amounts of nanoparticles (Figure 3-6A), but nanoparticles were absent in the cells that were subsequently grown on unsupplemented medium; only the CD, ferritin, NHHS Fe^{II} and HS Fe^{II} hemes were evident in the 5 K low-field MB

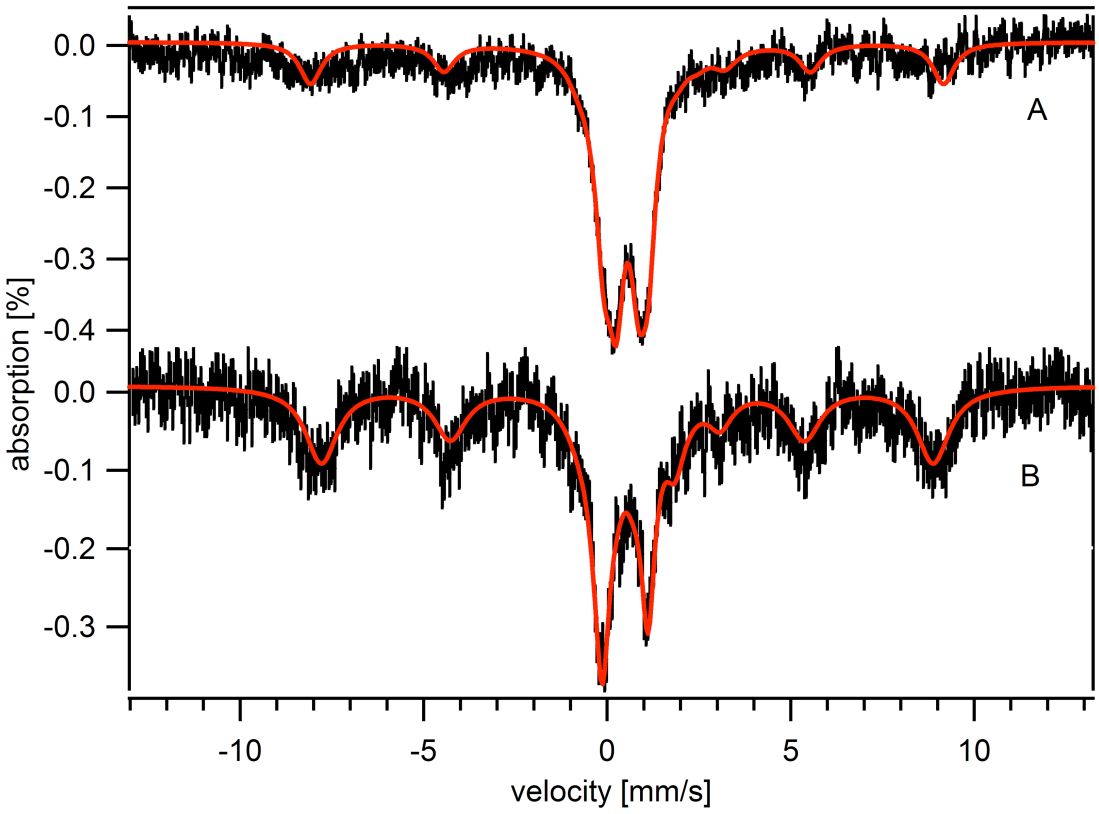

Figure 3-6. Bioavailability of nanoparticles. A, 5K, 0.05T Mössbauer spectra of 20FU cells (half-filled cup); B, derived from A, but after washing and further growth on medium unsupplemented with ^{57}Fe (filled cup).

spectrum (Figure 3-6B). Metal analysis combined with MB simulations of different Fe species (Table 3-1) indicated that the only feature that declined considerably in concentration (> 40-fold decrease) upon growth of the split cells was nanoparticles. Other features remain roughly unchanged, with minor decreases attributed mainly to dilution due to growth of the cells. These results indicate that Jurkat cells can utilize nanoparticle Fe, converting it into mitochondrial Fe, ferritin, and presumably all other Fe-containing species required for cellular metabolism.

Galactose-Grown Cells

Cells were grown with 3, 10, and 30 μM ^{57}FC in medium containing galactose rather than glucose as a carbon source. Cells grown on galactose and 3 μM ^{57}FC accumulated *ca*. half as much Fe as equivalent glucose-grown cells. However, the Fe concentration of galactose-grown cells increased faster than did glucose-grown cells as the FC concentration in the growth medium was raised. The concentration of Fe in cells grown with galactose and 10 μM FC was ~ 50% higher than in corresponding glucose-grown cells. Cells grown on galactose and 30 μM FC contained > twice as much Fe as the corresponding glucose-grown cells (Table 3-1). Galactose-grown cells had a longer doubling time (*ca.* 34 hr) which may have promoted Fe uptake.

MB analysis revealed that cells grown on galactose and 3 μM ^{57}FC were largely devoid of nanoparticles (Figure 3-7A, Table 3-1). Interestingly, the 5 K 0.05 T MB spectrum of cells grown on galactose and 10 μM FC exhibited a 3-fold *greater* contribution from nanoparticles and a decline of ferritin Fe relative to comparable

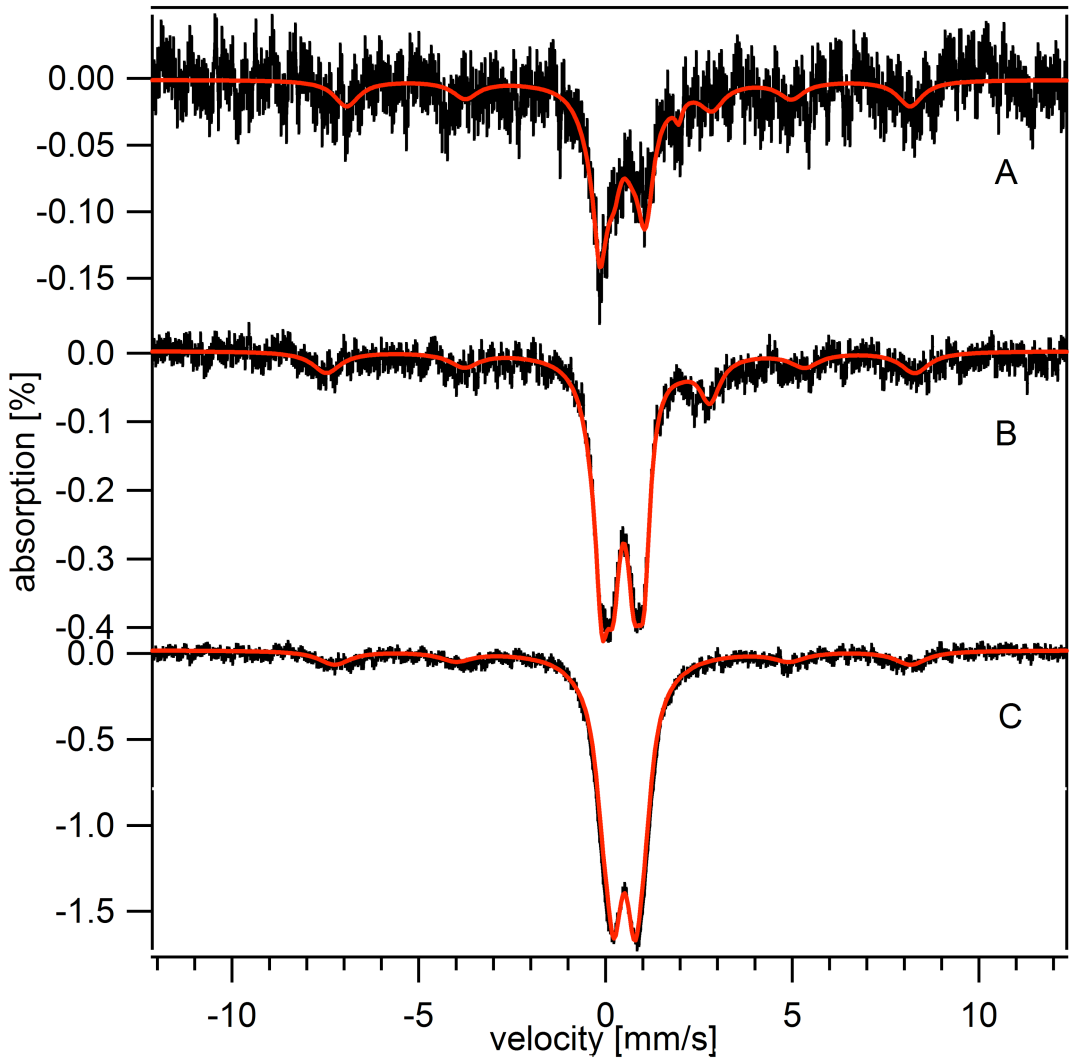

Figure 3-7. 5K, 0.05T Mössbauer spectra of galactose-grown cells. A, 3FL; B, 10FL; and C, 30FL. Simulations are shown in red.

glucose-grown cells (Figure 3-7B and Table 3-1). The nanoparticle doublet obscured the CD in the MB spectrum of galactose-grown cells, but simulation of the MB spectrum afforded an estimate of the percentage due to the CD. The low-intensity NHHS Fe^{II} doublet was evident, with a concentration similar to that observed for cells grown with glucose and 10 μM ^{57}FC. The absolute concentrations of nanoparticles (and possibly the CD) were significantly larger in galactose-grown cells grown on 30 μM ^{57}FC than in equivalent glucose-grown cells (Figure 3-7C, Table 3-1). Distinguishing these two contributions is difficult because they are not well resolved. UV-vis spectra of galactose-grown cells do not exhibit increased concentrations of cytochromes (Appendix II, Figure A7) suggesting that there is no significant increase in mitochondria concentration (and thus no significant increase in the CD). The concentration of ferritin Fe also did not change considerably in galactose-grown cells upon increasing the FC concentration in the medium.

The observed difference in nanoparticle level might be related to the different metabolic activity of galactose- *vs.* glucose-grown cells, and/or different growth rates. The oxygen consumption (OCR) rate of galactose-grown cells was 2 - 3 times greater than that of glucose-grown cells (Figure 3-8A). On the other hand, the normalized extra-cellular acidification rate (ECAR) of the glucose-grown cells was 3 - 4 times greater than that of the galactose-grown cells. The OCR of cells grown under the two different carbon sources was also determined in the absence and presence of oligomycin (an inhibitor of F_1F_0 ATP synthase). The normalized OCR of glucose-grown cells decreased

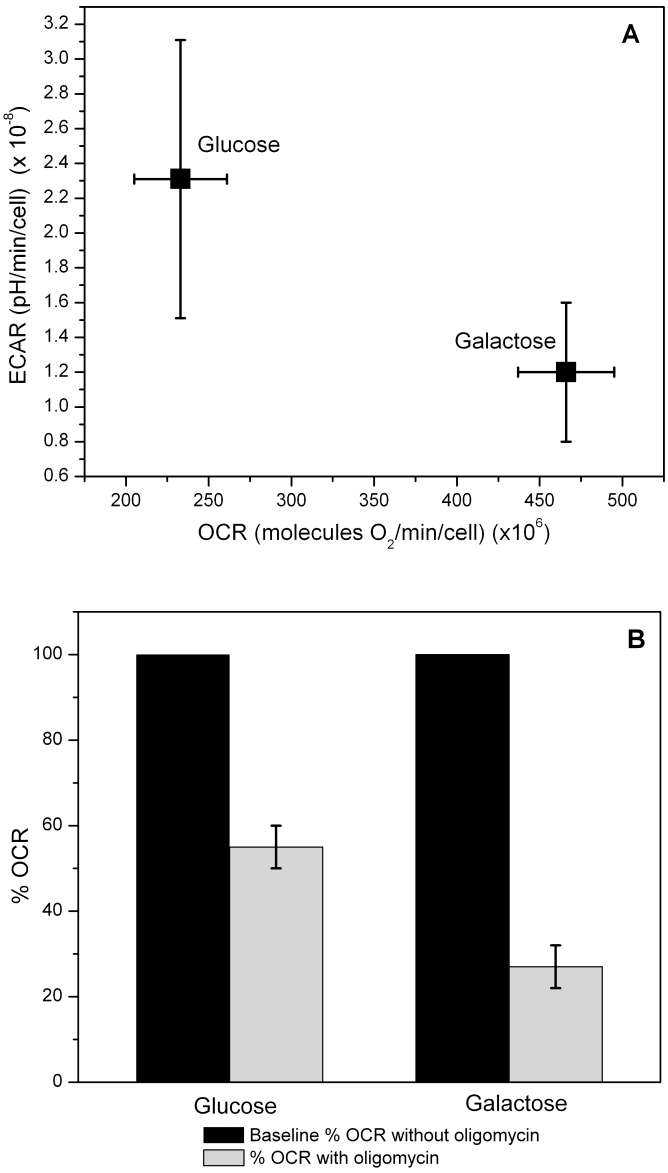

Figure 3-8. Oxygen consumption rate (OCR) and extracellular acidification rate (ECAR) of glucose- and galactose-grown cells. A. Normalized ECAR *vs*. OCR measurements of cells grown in glucose or galactose. B. Normalized OCR measurements of cells grown in glucose or galactose in the absence (black) or presence (grey) of 1 μM oligomycin.

~60% in the presence of oligomycin, whereas that of galactose-grown cells decreased almost ~80% (Figure 3-8B) indicating tighter coupling of respiration and ATP synthesis in galactose-grown cells [176]. These results confirm that our galactose-grown cells depended more heavily on oxidative phosphorylation (i.e. mitochondrial respiration) for ATP production than they did on glycolysis.

Oxidative Damage in Galactose-Grown Cells

Cells grown on galactose and FC exhibited ~ 50% higher levels of oxidative damage than cells grown on glucose and FC (Figure 3-5). The effect of cellular Fe concentration on the level of ROS damage was again minor, if any. The increased damage to galactose grown cells may be caused by the greater dependency on mitochondrial respiration and oxidative phosphorylation for ATP production in galactose-grown cells [179].

Increased Transferrin-Receptor Expression

Cells were grown on medium supplemented with 3 μM transferrin-bound ^{57}Fe (^{57}TBI). The total Fe concentration in such cells was quite low (140 μM) and the ^{57}Fe enrichment was only ~ 50%. Consequently, the corresponding 5 K low-field MB spectrum (Figure 3-9A) had a low percent-effect and was noisy. The general pattern indicated less ferritin and relatively more CD, compared to the Fe content of 3 μM ^{57}FC-grown cells. Spectral noise precluded a more detailed analysis. MB spectra of

mitochondria isolated from cells grown with 3 μM TBI (Figure 3-9C) exhibited little evidence of a nanoparticle doublet.

Increasing the ^{57}TBI concentration in the medium to 30 μM yielded an intracellular Fe concentration of 225 μM, which resulted in a more intense and analyzable 5 K low-field MB spectrum (Figure 3-9B). The spectrum was dominated by ferritin and CD Fe, and displayed a negligible nanoparticle doublet (Table 3-1). The extent of ferritin loading was ~3 times larger than in 3 μM or 10 μM (spectrum not shown) TBI-grown cells (Table 3-1), but was still low (~300 Fe/ferritin) relative to full loading.

In an effort to increase the Fe concentration in TBI-grown cells, cells were genetically modified to overexpress ~3-fold more TfRC1 than normal (Figure A10, Appendix II). Such cells (called TfRC^{+}) grown on 3 μM ^{57}TBI contained 3-times as much total Fe as equivalently grown WT cells. Correspondingly, the MB spectrum exhibited by the TfRC1^{+} cells (Figure 3-9D) was more intense. Sixty percent of the Fe in the cells was ferritin-bound, which was the highest percentage of Fe found in this form for any cell conditions examined. The sextet contribution was simulated and removed, revealing CD and NHHS Fe^{II} contributions. The spectrum included little if any nanoparticle doublet. TfRC^{+} cells were also grown with 10 μM ^{57}TBI; such cells accumulated ~ 25% more Fe than cells grown with 3 μM ^{57}TBI. MB analysis of these cells revealed a more significant accumulation of nanoparticles (Figure 3-9E and Table 3-1).

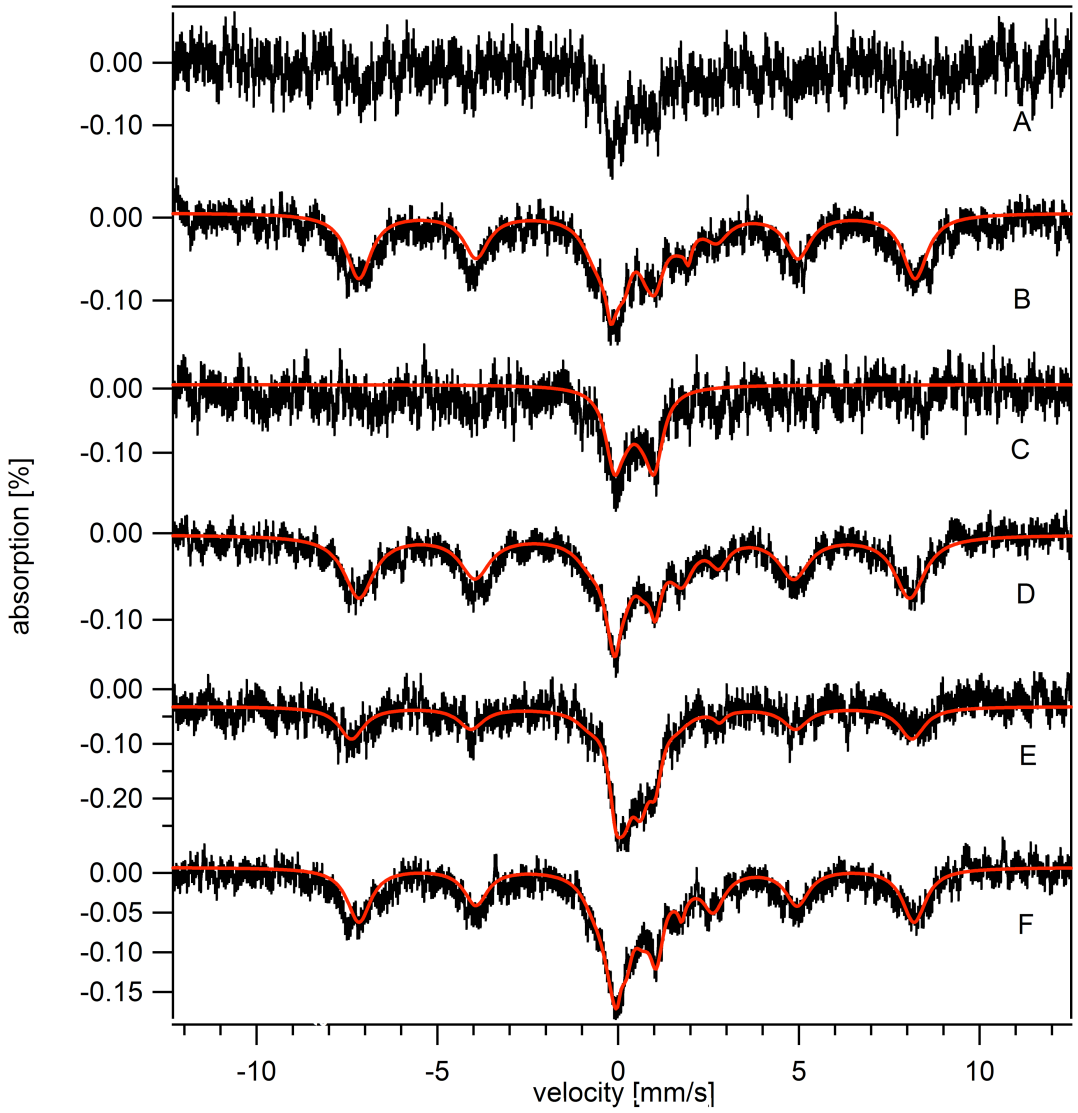

Figure 3-9. 5K, 0.05T Mössbauer spectra of Jurkat cells grown on TBI and mitochondria isolated therefrom. A, 3TU WT; B, 30TU WT; C, mitochondria isolated from cells in A; D, 3TU TfRC^{+}; E, 10TU TfRC^{+}; F, WT cells grown in unsupplemented glucose-containing medium with 100 μM DFO, and then transferred to medium containing 3 μM ^{57}TBI. Red lines are overall simulations using percentages given in Table 3-1 and parameters given in the Figure 3-1 legend.

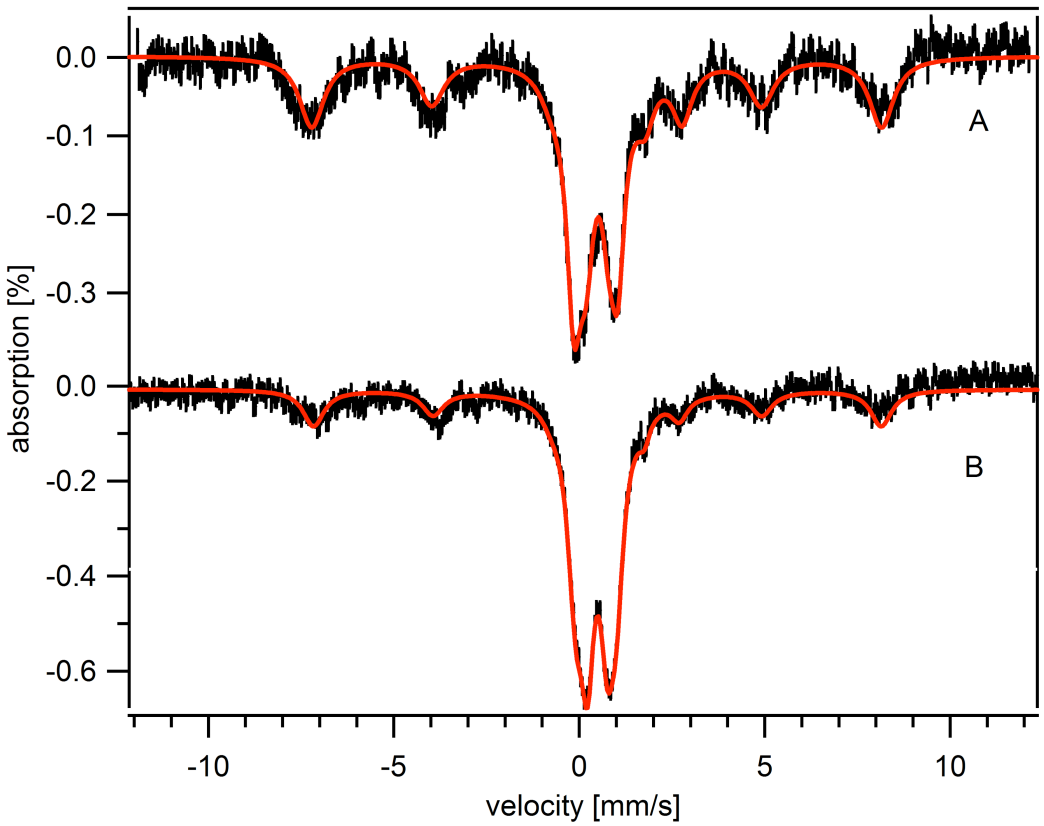

Figure 3-10. Effect of frataxin deficiency. A, 5K, 0.05T Mössbauer spectrum of WT 10FU; B, frataxin-deficient cells grown with 10 μM FC. Total simulations are showed in red using percentages given in Table 3-1.

We also attempted to stimulate WT cells to uptake TBI by first starving them of Fe in the presence of DFO for 12 hours (to upregulate TfRC1 expression), and then adding 3 μM ^{57}TBI to the growth culture. These cells incorporated *ca.* 3 times more ^{57}Fe than cells grown on 3 μM ^{57}TBI without this stimulation. These cells accumulated Fe mainly in the form of ferritin and CD (Figure 3-9F, Table 3-1).

Reduced Frataxin Expression

We also examined the Fe content of Jurkat cells in which frataxin expression was reduced by RNAi. Western blot analysis indicated that the expression level of frataxin in frataxin-deficient cells was 30-50% that of WT levels in cells grown under the same conditions (10 μM FC) (Figure A11, Appendix II). Frataxin-deficient cells grown with 10 μM FC accumulated significantly more nanoparticles than normal cells grown under the same conditions (Figure 3-10, Table 3-1). The concentration of nanoparticles detected by MB spectroscopy was *ca*. 3× greater in frataxin-deficient cells (220 μM *vs.* 72 μM in WT cells). These cells accumulated more total cellular Fe than WT cells (550 μM *vs.* 400 μM) (Table 3-1), with most of the excess Fe present as nanoparticles. UV-Vis analysis indicated a ~ 40% decline in cytochrome levels of frataxin-deficient cells relative to WT cells (Figure A12, Appendix II).

Analysis

We analyzed our data by developing a chemical model for the import and trafficking pathways in human Jurkat cells (Figure 3-11). Cellular Fe was assumed to be composed of 4 species, namely $[Fe_{cell}] = [Fe_c] + [Fe_f] + [Fe_m] + [Fe_n]$. Fe could enter the cell by either TBI or FC import pathways. Both pathways merged at Fe_c, an unidentified cytosolic Fe species presumed to correspond to the NHHS Fe^{II} spectral feature observed in MB spectra of Jurkat cells. According to the model, Fe_c can react to form Fe_f, Fe_m and Fe_n, which represent the Fe associated with ferritin, mitochondria and nanoparticles, respectively. Fe_m is the sum of cellular Fe-S clusters and hemes, which we assumed to be originating exclusively from mitochondria.

The model was translated into ordinary differential equations (ODE's) [1] – [4] which describe the factors that influence the changes in concentration of each cellular component.

$$\frac{d[Fe_c]}{dt} = \frac{k_t[TBI]}{1+\left(\frac{[Fe_c]}{K_{Ic}}\right)^{cs}} + k_r[FC] - \frac{k_m[Fe_c]}{1+\left(\frac{[Fe_m]}{K_{\mathrm{Im}}}\right)^{ms}} - \frac{k_f[Fe_c]}{1+\left(\frac{[Fe_f]}{K_{If}}\right)^{fs}} - k_n[Fe_c]^p - \alpha[Fe_c] \qquad [1]$$

$$\frac{d[Fe_f]}{dt} = \frac{k_f[Fe_c]}{1+\left(\frac{[Fe_f]}{K_{If}}\right)^{fs}} - \alpha[Fe_f] \qquad [2]$$

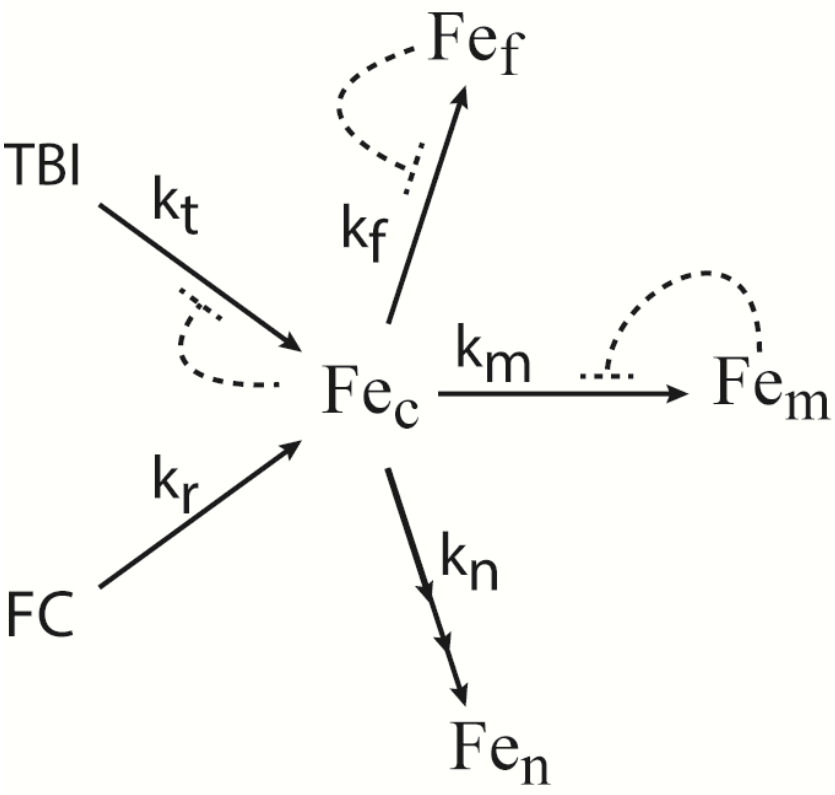

Figure 3-11. Model of Fe import and intracellular trafficking in Jurkat cells. Solid arrows indicate reactions associated with rate-constants k_t, k_r, k_f, k_m and k_n. Reactions k_t and k_r represent import of TBI and FC Fe, respectively. Reactions k_f and k_m represent transfer of Fe_c to ferritin and mitochondria, respectively. Reaction k_n represents conversion of cytosolic Fe into nanoparticles. Dashed lines terminating at short straight orthogonal segments represent regulation sites. The lines emanate from the sensed form of Fe. The triple-headed arrow indicates higher-order dependence of Fe_c on that reaction.

$$\frac{d[Fe_m]}{dt} = \frac{k_m[Fe_c]}{1+\left(\frac{[Fe_m]}{K_{\mathrm{Im}}}\right)^{ms}} - \alpha[Fe_m] \qquad [3]$$

$$\frac{d[Fe_n]}{dt} = k_n[Fe_c]^p - \alpha[Fe_n] \qquad [4]$$

The first term on the right-hand-side of equation [1] describes the rate of import of TBI through the TfRC1 on the plasma membrane. Regulation of this and two others rates in the model are described by the function

$$\mathrm{Reg\_}(Fe_s, K_{Is}, s) = \frac{1}{1+\left(\frac{[Fe_s]}{K_{Is}}\right)^{s}}$$

in which species Fe_s is sensed by the regulatory system, K_{Is} is an apparent inhibition constant associated with the sensing event (also called a set-point concentration), and s is a sensitivity parameter. *Reg*_ is a form of the Hill equation that we have used as a surrogate for poorly defined or highly complex regulatory mechanisms. *Reg*_ could reflect the direct (or indirect) binding of Fe_s to: a) the promoter of a gene (i.e. transcriptional regulation); b) an mRNA strand (translational regulation); or c) an allosteric site of a protein (enzyme regulation). *Reg*_ can be viewed as a valve that opens wide when $[Fe_s] < K_{Is}$, shuts down when $[Fe_s] > K_{Is}$, and is half-opened when $[Fe_s] = K_{Is}$. The rate of TBI influx is regulated by *Reg*_, with Fe_c serving as Fe_s. In this case, *Reg*_ is a surrogate for the Fe-dependent binding of IRP1/2 to the mRNA of the transferrin receptor mRNA.

The second term of [1] reflects the *unregulated* import of FC. Our model is minimal in that no unnecessary terms are included. We could fit the data in Table 3-1 acceptably well without assuming that the import of FC was regulated. The third term of [1] reflects the flow of Fe_c into mitochondria. The rate of mitochondrial Fe import via mitoferrin1/2 is regulated but the mechanism has not been established in non-erythroid cells, except for the fact that these proteins are regulated post-translationally [42, 43]. The sensed molecule in this process was assumed to be the concentration of mitochondrial Fe_m.

The fourth term of [1] reflects the loading of Fe into ferritin. IRP1/2 also regulate ferritin synthesis in an Fe-dependent manner, stimulating production of ferritin under high-Fe conditions [87]. We initially tried to regulate the system in this manner (by multiplying the rate of Fe loading into ferritin (k_f) by the function $Reg_+ = 1 - Reg_-$, using Fe_c as the sensed molecule) but the resulting behavior was not satisfactory, as the observed ferritin concentrations changed significantly less than the simulated concentrations. This suggested that the regulation of ferritin loading was more like the regulation of mitochondrial Fe import. Thus, we employed the Reg_- function in the manner used to regulate mitochondrial Fe import, namely by assuming that the sensed Fe_s was ferritin Fe_f.

The fifth term of [1] refers to the rate of nanoparticle formation. We initially assumed a first-order dependence of $[Fe_c]$ in this process, but our simulations could not reproduce the disproportionate increase in nanoparticles (Fe_n) that occurred when the FC concentration in the growth medium increased (e.g. from 3 → 30 or →100 μM).

Mimicking this behavior required that we assumed a higher-order dependence on [Fe_c] (Table 3-1). This order-dependence is consistent with a mechanism in which multiple (~ 3) Fe ions react at or before the rate-determining step in the formation of nanoparticles.

The last term of [1] reflects dilution due to cell growth. In our model, the cell is growing as Fe is imported, such that a steady-state Fe_{cell} concentration is eventually achieved (The Fe concentration data of Table 3-1 was interpreted as representing steady-state values). Each component of a growing cell requires a dilution term in its ODE [180]. The growth rate α was assumed to be the inverse of the doubling time.

The sum of ODEs [1] – [4]

$$\frac{d[Fe_{cell}]}{dt} = \frac{k_t[TBI]}{1+\left(\frac{[Fe_c]}{K_{Ic}}\right)^{cs}} + k_r[FC] - \alpha[Fe_{cell}]$$

defines how the overall Fe concentration of the cell changes in time. In the absence of TBI and under Fe-limiting steady-state growth conditions, $k_r[FC] = \alpha[Fe_{cell}]$. [FC] in this equation includes not only the concentration of ferric citrate in the medium, but the endogenous Fe (6 μM). In the absence of FC, [Fe_{cell}] ≈ 100 μM and [FC] = 6 μM such that a DT of 24 hr implies that $k_r \approx 0.7$ hr^{-1}. When grown on 100 μM FC, [Fe_{cell}] = 3500 μM, [FC] = 106 μM, and thus $k_r \approx 1.3$ hr^{-1}. We view this range for k_r (1.0 ± 0.3) as acceptable, given the simplicity of the model.

Sensitivity factors *ms* and *fs* were set semi-arbitrarily to 10 to provide extremely tight regulation. The other parameters of the system (*cs*, K_{Ic}, K_{Im}, K_{If}, k_t, k_m, k_f, k_n and *p*) were estimated by attempting to simulate the entire dataset of Table 3-1. The ODEs were

numerically integrated using Maple software (http://www.maplesoft.com/). Growth conditions of the simulation model cell were varied to mimic the conditions listed in Table 3-1. For $TfRC^+$ cells, the constitutive overexpression of TfRC was mimicked by assuming a 6-fold faster import rate constant k_t AND by removing the *Reg*- term. Cells grew slower on galactose than on glucose (DT = 34 hr rather than 24 hr) so α was adjusted accordingly for those simulations. Each simulation was allowed to continue for 1000 hr (where time refers to that indicated in the ODEs) to assure that steady-state conditions had been achieved. Resulting simulated concentrations are given in Table 3-1. The uncertainties associated with the data were estimated to be ± 20% so that minor discrepancies between simulations and data are considered irrelevant. The model is simple, semi-quantitative, and foundational. It captures the essential features of Fe import and trafficking in Jurkat cells, but lacks many details associated with these processes.

One advantage of ODE models is that they have predictive power. Thus, our model can predict the distribution of these 4 forms of Fe in Jurkat cells grown with any concentration of TBI or FC. It can also be modified so as to explore genetic changes in the cell - such as the consequences of reducing the expression level of frataxin. Previous studies in yeast and mice have shown that a frataxin deficiency causes the accumulation of nanoparticles in mitochondria. This leads to an Fe-deficiency condition in the cytosol [130, 174, 181]. To examine how our model would respond to this phenotype, we allowed for

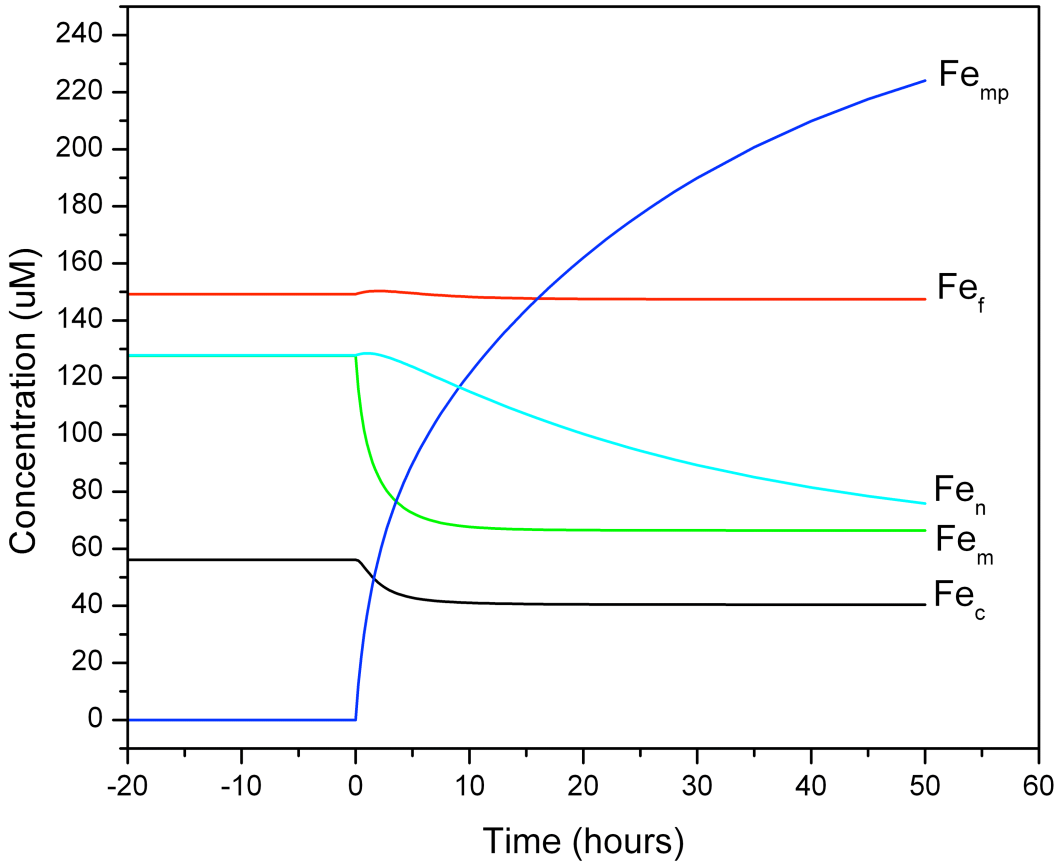

Figure 3-12. Simulation of the changes in cellular iron distribution following frataxin depletion. The simulation at $t < 0$ is of WT glucose-grown cells in 10 µM FC, with DT = 24 hr and $k_{mp} = 0$. At $t = 0$, k_{mp} was set to 0.000045 hr^{-1} and DT to 30 hr.

the possible formation of nanoparticles in the mitochondria (by adding the term ($-k_{np}[Fe_m]^p$) to the ODE of equation [3] and by adding ODE [5]

$$\frac{d[Fe_{mp}]}{dt} = k_{mp}[Fe_m]^{mp} - \alpha[Fe_{mp}] \qquad [5]$$

to the set of ODEs [1] – [4]. For simplicity, we assumed that the kinetics of nanoparticle formation in the mitochondria were the same as for nanoparticle formation in the original model (presumably in the cytosol). As such, we assigned k_{mp} and mp to the same values assigned to k_{np} and p, respectively.

As a control, we solved the new system assuming $k_{mp} = 0$ and $\alpha = 1/24$ hr so as to mimic WT expression levels of frataxin and the growth rate of WT cells. Resulting steady-state simulated concentrations are shown in the early region of the plot of Figure 3-12. We then set k_{mp} = 0.00045 hr^{-1} and α to 1/30 hr^{-1} to stimulate mitochondrial nanoparticle formation and mimic the slower-growing frataxin-deficient cells. The overall Fe concentration increased in our simulations from 461 to 528 μM, similar to the change observed experimentally. The simulation included an increase in mitochondrial nanoparticles as well as a decline of non-nanoparticle forms of mitochondrial Fe (interpreted as Fe/S clusters, hemes and the pool of NHHS Fe^{II}). These latter changes are consistent with the deficiencies of Fe/S clusters and hemes that are associated (along with the dominance of nanoparticles) with the frataxin phenotype [182]. The simulated response to frataxin deficiency also included a decline of cytosolic and ferritin Fe, consistent with the cytosolic Fe-deficiency phenotype that has been reported [130]. We repeated the simulation at 3 μM FC concentration, but no phenotype was evident.

Discussion

Using MB spectroscopy and other biophysical methods, we have investigated the Fe import pathways and downstream trafficking of two forms of Fe in human Jurkat cells, namely transferrin-bound iron (TBI) and ferric citrate (FC). We did this by characterizing the Fe content of such cells grown in media containing different concentrations of TBI and/or FC and different carbon sources (glucose *vs*. galactose). We also investigated cells in which the expression levels of the transferrin-receptor and frataxin were altered. We developed a mathematical model of Fe import and trafficking in these cells, and fitted simulations obtained therefrom to our data.

TBI and FC Import Pathways

Our data and simulations indicate that the import of TBI iron is highly regulated. Our model suggests that cytosolic Fe regulates TBI import in accordance with a set-point concentration of 9 μM. In contrast, the import of FC does not appear to be regulated, or at least our model did not require that assumption. Whether the same holds true of other forms of NTBI remains to be determined, but we regard this as a viable possibility.

The fate of TBI (after DMT1-promoted export from endosomes into the cytosol) and the fate of FC within the cell are largely unknown. An earlier version of the model assumed two forms of cytosolic Fe, one derived from TBI and the other from FC. However, this assumption did not improve the fits and so we merged the two import pathways immediately once Fe entered the cytosol. In real cells, the pathways may not

merge immediately. However, they must eventually merge. Fe from either source eventually traffics into mitochondria (via the IM transporters mitoferrin1/2 [41]), loads into ferritin (via PCBP1/2 chaperones [75, 183]), and forms nanoparticles. There is probably no dedicated protein chaperones that traffics Fe into nanoparticles. Rather, these particles appear to form spontaneously via chemistry of which the cell is unaware.

The distribution of Fe in TBI-grown cells differs relative to that in cells grown on the same concentration of FC, primarily because less Fe overall is imported into TBI-grown cells. This is due, in turn, to the tighter regulation of TBI import. The higher concentration of cytosolic Fe in FC-grown cells increases the rate of nanoparticles formation disproportionately, such that it dominates the Fe content of FC-grown cells but not TBI-grown cells. Consistent with this, TBI-grown cells in which the transferrin-receptor was constitutively overexpressed contained higher concentrations of Fe, relative to WT cells grown on TBI. The distribution of Fe in these cells was similar but not identical to that observed in FC-grown cells.

Another likely reason for the different Fe distributions is that the TBI pathway may somehow favor storing Fe as ferritin relative to the FC pathway which tends to funnel more Fe into nanoparticles. Our current model does not include such distinctions, but the possibility of distinct intracellular pathways should be considered when developing more advanced models. Supporting such a distinction at the protein expression level, our data show a more sensitive upregulation of ferritin protein in TBI-grown cells relative to in FC-grown cells. For example, cells grown with 3 μM TBI had twice the concentration of ferritin compared to cells grown with 3 μM FC. This suggests

that the IRP1/2 system of regulation responds more sensitively to Fe_c derived from TBI. Furthermore, $TfRC^+$ cells grown on 3 μM TBI accumulated the same cellular Fe concentration as WT cells grown with 10 μM FC, but that Fe included significantly fewer nanoparticles and more ferritin Fe. Our simple model cannot account for such differences.

Mitochondria

The concentrations of mitochondrial Fe centers, including Fe-S clusters, hemes and HS Fe^{III} ions, do not change drastically upon increasing the medium Fe concentration. This indicates the ability of mitochondria to regulate their own Fe import. The expression of the only known Fe transporters in the mitochondrial membrane, mitoferrin 1 and mitoferrin 2 (Mfrn1 and Mfrn2) is tightly regulated to prevent excessive mitochondrial Fe accumulation [42]. To mimic this invariance, our model tightly regulated mitochondrial Fe import using mitochondrial Fe itself as the sensed species. Clearly, not all mitochondrial Fe is sensed. Nevertheless, this regulatory assumption would remain viable as long as the concentration of the sensed molecule was proportional to the overall mitochondrial Fe concentration. The concentration of nanoparticles in mitochondria does seem to increase with the concentration of Fe in the medium. Again, this form of Fe may not be regulated by the cell; indeed the cell may be unaware of its existence.

Ferritin

The extent of Fe loading into ferritin was an order-of-magnitude less than the often-quoted value of 4500 Fe per core. Moreover, the extent of loading did not increase with increasing Fe concentration in the growth medium (which we presume is proportional to the cytosolic Fe concentration). Both results were surprising.

The low average extent of loading is undoubtedly due to a distribution of loading levels in a population of ferritin molecules. Ferritin-loading distributions have been previously described for ferritin purified from various organs, using ultracentrifugation [184] or MB spectroscopy coupled with electron microscopy [177, 185]. Bovell *et al*. obtained similar results by performing *in situ* electron microscopy coupled with ASAX analysis on rat liver sections [178]. We suggest a binomial distribution of Fe loadings in ferritin populations of Jurkat cells, with the maximum approaching 4500 Fe per ferritin and the mean near 400 Fe/ferritin. Our studies also suggest that the average ferritin-load remains about the same regardless of the overall Fe concentration in the cell (though perhaps lower load in 3 and 10 μM TBI-grown cells). Our results are consistent with an EM study showing a distribution of ferritin loading in iron-overloaded rat livers [178].

The popular explanation of IRP1/2 regulation of ferritin is that the unbinding of these proteins to the ferritin message under high cytosolic Fe concentrations promotes ferritin synthesis *so that* excess cytosolic Fe can be removed from the cytosol and stored in ferritin [87]. The implication is that without this promotion, there would be no way for excess cytosolic Fe to be removed - *because the existing ferritin was already fully loaded*. The regulation of ferritin and the extent of loading do not appear to be so

simple, at least in Jurkat cells. Cells containing partially loaded ferritin responded to increasing (cytosolic/medium) Fe concentrations by synthesizing more ferritin proteins, not by loading pre-existing ferritin to the fullest possible extent. Another spurious initial notion of ours was that nanoparticles would form only once the cell exhausted its ferritin-binding capacity. In contrast, we found that the ferritin was partially loaded in FC-grown cells that also contained substantial quantities of nanoparticles.

One explanation of this partial-loading behavior is that the set-point concentrations for ferritin synthesis and Fe-loading of ferritin differ. The set-point concentration of the Fe species that regulates the synthesis of new ferritin protein (via the IRP1/2 system) might be lower than the concentration of Fe required to fully load ferritin. In this way, as cytosolic Fe levels increase, they trigger further ferritin protein synthesis such that existing ferritin never becomes fully loaded.

Another shift in our thinking arose from our attempt to model the concentration of ferritin Fe in cells grown under different conditions. The concentration of ferritin Fe was roughly invariant among all of the conditions tested and examined by MB spectroscopy (Fe-limited cells and Fe-overloaded cells could not be investigated by MB). We initially attempted to model this using the well-known IRP1/2 mechanism. This required a Reg_+ function in which Fe_c was sensed. However, this resulted in *greater* variation in Fe ferritin levels than was evident in the data. Thus, we abandoned that form of regulation and employed a Reg_- function in which ferritin Fe_f was sensed (we did this after noting how well mitochondrial Fe could be regulated by assuming the Reg_- function with Fe_m as the sensed molecule). This arrangement adequately reproduced

ferritin Fe levels under the various circumstances examined. However, the molecular-level mechanism responsible for this form of regulation is not understood; it seems unlikely that ferritin Fe could directly be sensed since it is an aggregated form. The rate of Fe import into ferritin might be inhibited as the degree of ferritin loading reaches some critical threshold, as has been suggested based on the rates of ferritin loading *in vitro* [186, 187].

Nanoparticles

The nanoparticles that accumulate in Jurkat cells are similar in chemical composition to those found in strains of yeast that have mutations in Fe/S cluster metabolism proteins [117, 139]. The modest differences in high-field MB spectra, relative to yeast nanoparticles, suggest modest structural differences. Previous MB studies of the spleens of β-thalassemia patients [188] indicate accumulation of a species with MB parameters similar to the nanoparticle doublet observed here. Ferric phosphate nanoparticles accumulate in the hearts of mice displaying symptoms of Friedreich's ataxia [173]. The size of the particles observed in our cells are substantially smaller than ferritin particles (~ 1 nm *vs.* 2.8 – 8 nm) [177, 189] and they contain more phosphorus than ferritins [190]. Our results suggest that the majority of nanoparticles formed in these cells are non-mitochondrial. Our EM results suggest that nanoparticles form in the cytosol, and this was assumed by our model.

Our model suggests that the rate of nanoparticles formation is *not* regulated. This is consistent with the idea that the cell is unaware that nanoparticles are forming,

suggesting that this is a purely chemical phenomenon. Although nanoparticles cannot be sensed by the cell, they may nevertheless play a role in cellular metabolism. We found that nanoparticles formation is reversible and that nanoparticle Fe can be recycled by the cell.

Our model required that the rate of nanoparticle formation depend on the cytosolic Fe concentration to higher than first order. This high-order rate dependence leads to the observed "burst" phenomenon in which there is a disproportionate increase in nanoparticles as the Fe_c concentration increases. It implies that more than one Fe^{III} ions (nominally 3 such ions, according to our simulations) come together to form nanoparticles at or before the rate-determining step in the process.

Oxidative Damage

The lack of correlation between the extent of nanoparticle formation and oxidative damage in FC-grown cells grown on glucose is consistent with the results of Hartwig *et al*. who found that oxidative damage to DNA and lipid peroxidation in glucose-grown mammalian cells is *not* induced by growth on up to 2 mM FC [191, 192]. Fe^{III} nanoparticles form from the oxidation of Fe^{II} ions, but whether this generates ROS (or is promoted by ROS) is uncertain. Our results indicate that the overall level of cellular ROS damage does NOT correlate significantly with cellular Fe or nanoparticle level. Nanoparticle formation may generate (or be generated by) small amounts of ROS, but this doesn't impact cellular ROS levels significantly. ROS can be scavenged by catalases, peroxidases and antioxidants [3, 193]. Perhaps the observed extent of oxidative

damage is inversely related to the rate of these repairs. Also, metabolic mode and growth rate may be factors in the level of cellular ROS damage. These considerations are supported by our finding that galactose-grown cells (which are more active in terms of respiration and also grow more slowly) are associated with greater ROS damage.

Our results and conclusions regarding the insignificance of nanoparticle formation on overall cellular oxidative damage are literally *opposite* of that proposed by Whitnall *et al*. [173] who identified nanoparticles in the hearts of frataxin-deficient mice. They proposed that nanoparticles may be an "explosive" (their emphasis) source of ROS in such diseased heart tissue. Our data suggest that nanoparticle formation has little impact on cellular ROS levels.

Frataxin

Although simple, our model reproduces the major effects of depleting cells of frataxin. Besides accumulating nanoparticles in the mitochondria (which was designed into the model), other cellular Fe species in the model responded in ways that are also observed experimentally. Frataxin-deficient cells "feel" Fe-deficient in the cytosol, due to the increased rate of Fe import into mitochondria. This effect was recreated in our simulations. Importantly, there was no alteration of the regulation of the entire system – including the regulation of Fe import into the mitochondria themselves. The increase in total mitochondrial Fe (including $[Fe_m] + [Fe_{mp}]$) was associated with the *decline* in $[Fe_m]$ as this form of Fe was used to make mitochondrial nanoparticles. This decline stimulated further Fe import into the organelle, which created a deficiency of Fe in the

cytosol. Importantly, this imbalance of Fe in the cell was due to nanoparticle formation in the mitochondria, *not* to malfunctioning regulatory systems. Our study and model suggest that there is nothing "wrong" with Fe regulation in cells that are deficient in frataxin (or by extension, in patients with Friedrich's ataxia). The problem is that a deficiency of frataxin somehow alters the mitochondrial matrix so as to favor nanoparticle formation. This might involve changes in pH, redox state, or chemical composition. Understanding the mechanistic basis of these alterations will be critical in understanding and treating the disease.

Mathematical Modeling

Interpreting changes in cellular Fe metabolism (or any other complex cellular metabolic subsystem) on the molecular/mechanistic level is difficult, as the complexity of these systems is enormous. As more molecular-level interactions are discovered and characterized, it becomes increasingly difficult (and will eventually become impossible) to draw mechanistic inferences based merely on mentally contemplating such interactions. Gaining mechanistic insights will increasingly require the aid of mathematical models that can include an unlimited number of relationships explicitly and can integrate their collective effects.

CHAPTER IV

IRON CONTENT OF *SACCHAROMYCES CEREVISIAE* CELLS GROWN UNDER IRON-DEFICIENT AND IRON-OVERLOAD CONDITIONS*

Introduction

Iron plays critical roles in cells, including as redox agents within mitochondrial respiratory complexes and as active-site metals in numerous metalloenzymes [194-196]. Iron can also be deleterious, in that certain types of Fe centers, e.g. labile mononuclear nonheme Fe^{II} complexes, engage in Fenton chemistry to generate reactive oxygen species (ROS). Thus, Fe trafficking in cells must be highly regulated to allow Fe to be used in cellular functions while also minimizing deleterious side-processes. Understanding the molecular-level details of how cells do this is a current challenge in the field.

---

*This chapter is reproduced with permission from: "Iron Content of *Saccharomyces cerevisiae* Cells Grown under Iron-Deficient and Iron-Overload Conditions" by Gregory P. Holmes –Hampton, Nema D. Jhurry, Sean P. McCormick, and Paul A. Lindahl, 2013, *Biochemistry*, 52, 105-114, Copyright 2013 American Chemical Society. My contributions to these studies were to isolate mitochondria from cells grown under fermenting conditions and varying iron concentrations, and prepare samples for analysis by Mössbauer, EPR, and UV-Vis spectroscopies, as well as perform Oxyblot analysis on isolated mitochondria. Copyright 2013 American Chemical Society.

Cellular Fe trafficking involves numerous components interacting as a system. Membrane-bound proteins transport Fe across cellular and organellar membranes, while Fe-binding proteins and perhaps low-molecular-mass Fe complexes traffic Fe within aqueous regions of the cell [197]. Iron-sensing proteins and DNA-binding transcription factors control gene expression levels of Fe-associated species [198, 199], while various chaperone proteins install Fe ions into myriad target/recipient apo-proteins.

The details of Fe trafficking are best understood in the budding yeast *Saccharomyces cerevisiae* [200]. These cells import Fe through several pathways. A *high-affinity* pathway imports Fe through the Fet3p/Ftr1p complex on the plasma membrane. This pathway allows WT cells to grow under *Fe-deficient* conditions [201] in which the growth medium is pretreated with bathophenanthroline sulfonate (BPS), a strong chelator of Fe^{II} ions. The resulting $[Fe^{II}(BPS)_3]^{4-}$ complex, generated using endogenous Fe in the growth medium, is inaccessible to cells for growth [202]. WT cells growing in Fe-deficient medium express the *iron regulon*, a group of *ca*. 20 genes, including FET3 and FTR1 [203]. Gene expression is controlled by the transcription factor Aft1p [198, 199, 204]. Under Fe-deficient conditions, Aft1p moves from the cytosol to the nucleus where it increases expression of iron regulon genes. Under Fe-sufficient and Fe-overload conditions, Aft1p moves to the cytosol, decreasing expression of these genes. The rate of Fe import into the cell by the high-affinity system is *saturable*, such that plots of rates *vs*. the concentration of Fe in the medium ($[Fe_{med}]$) can be fitted to a Michaelis-Menten-type expression with apparent $K_m \sim 0.2$ μM [205-208].

Iron metabolism in cells grown under Fe-deficient conditions is also regulated post-transcriptionally. Cth1p and Cth2p bind to mRNA strands transcribed from various Fe-associated genes [209]. This destabilizes those transcripts and curtails protein synthesis. Cth2p binds and destabilizes the mRNA of Ccc1p, the only known Fe importer on the vacuolar membrane. Vacuoles store and detoxify Fe. These transcription factors also destabilize the mRNA of genes involved in Fe/S cluster and heme biosynthesis and respiration. Under Fe-deficient conditions, this regulatory mechanism minimizes the use of Fe by preventing vacuoles from depleting the cytosol of Fe and by curtailing synthesis of Fe-containing proteins.

Fe-sufficient growth conditions are defined here as having 5 – 40 μM Fe in the medium ($[Fe_{med}]$). Cells lacking the high-affinity Fe import pathway can grow under such conditions [202, 207] due to *low-affinity* pathways. Fe^{II} ions can be imported through Smf1p and Fet4p on the plasma membrane, with apparent K_m values of 2.2 and 33-41 μM, respectively [206, 210-212]. Once imported, Fe is trafficked to vacuoles, mitochondria, and other organelles. CCC1 gene expression is controlled by transcription factor Yap5 which activates CCC1 under intermediate and high cytosolic Fe ($[Fe_{cyt}]$) [213]. Once installed in the vacuolar membrane, the newly synthesized Ccc1p imports Fe into the vacuole [139, 196, 214]. Isolated vacuoles from fermenting cells grown in medium with $[Fe_{med}]$ = 40 μM contain a magnetically-isolated mononuclear HS Fe^{III} species [120]. In fermenting Fe-sufficient yeast cells, this species represents ~75% of total cellular Fe [118]. Fe in vacuoles can also be found as Fe^{III} nanoparticles [120, 215]. These organelles export Fe

through Fet5p and Fth1p, homologs of the Fet3p and Ftr1p [216], and through Smf3p, a homolog of Smf1p [217].

The same cytosolic Fe species that is imported into vacuoles [218] is presumed to be imported into mitochondria primarily through high-affinity transporters Mrs3/4p [219, 220]. *High-affinity* in this case means that ΔMrs3/4 cells cannot grow on Fe-deficient medium [219, 221], apparently because [Fe_{cyt}] in such cells is insufficient to be imported rapidly into mitochondria. Since mitochondria are the sole site of heme biosynthesis in the cell and the major site of Fe/S cluster biosynthesis, Fe-deficient ΔMrs3/4 cells probably cannot generate sufficient quantities of these prosthetic groups. These and other results imply that [Fe_{cyt}] is proportional to [Fe_{med}], at least under low-Fe conditions. These same strains can grow normally under Fe-sufficient conditions [219], implying that other low-affinity mitochondrial import pathways can operate when [Fe_{cyt}] is higher than it is under Fe-deficient conditions.

Little is known about the Fe content and distribution in cells grown under Fe-overload growth conditions, defined here as being > 40 μM. Only at extremely high concentrations is toxicity observed. WT cells grow reasonably well in medium containing as high as 5 mM – 10 mM Fe^{II} [222-226] and 20 mM Fe^{III} [215].

We use an integrated biophysical approach centered on Mössbauer spectroscopy to evaluate the Fe content of organelles, cells, and tissues from a systems-level perspective [120, 124, 227]. In this paper, we analyze WT yeast cells grown on Fe-deficient and Fe-overloaded growth medium, as well as mitochondria isolated there-from. Under Fe-deficient condition, cells *prioritize* their use of Fe, using it for essential functions that

involve Fe/S cluster and heme centers, and minimizing nanoparticles and vacuolar Fe. Cells grown on Fe concentrations ranging from 40 – 10,000 μM [Fe_{med}] maintained nearly the same Fe concentration and speciation despite a 250-fold increase in environmental Fe, indicating an amazing ability to regulate Fe import. A model that rationalizes these results is presented.

Experimental Procedures

Cell Growth and Preparation of Samples

WT strain W303-1B and strain DY150, FET3-GFP::KanMX [228] were used. DY150 is isogenic to W303 [229], and it was used for studies involving Fet3-GFP. Cells were grown on minimal medium without added Fe [117-119], called *Fe-unsupplemented*. The medium contained (2% w/v) glucose or galactose to establish fermenting or respirofermenting growth modes, respectively. Iron-deficient medium was prepared by adding 21 μM BPS (Sigma-Aldrich) to Fe-unsupplemented minimal medium, followed by supplementing with 1 μM ^{57}Fe(citrate). This corresponded to a molar excess of BPS (the endogenous Fe concentration in minimal medium was ~ 100 nM). ^{57}Fe citrate was prepared by dissolving ^{57}Fe metal powder (IsoFlex USA) in a 1:1 mixture of concentrated trace-metal grade (TMG) HNO_3 and HCl (Fisher Scientific) and diluting with double-distilled water. The resulting 80 mM Fe stock contained ~ 0.2% (v/v) acid. The solution was diluted further with distilled water and treated with a 3-fold molar

excess of sodium citrate (Fisher Scientific). The solution was adjusted to pH ~ 5 with 1 M NaOH (EMD chemicals) resulting in a final concentration of 40 mM ^{57}Fe citrate.

Fifty mL of Fe-unsupplemented minimal medium was inoculated with a single colony from a YPAD (1% yeast extract, 2% peptone 40 mg/L adenine sulfate, and 2% dextrose) plate. Cells were allowed to grow to an OD600 of 1.0 - 1.4 in a 30 °C rotary incubator at 150 rpm. The culture was used to inoculate fermenting minimal media supplemented with different concentrations of ^{57}Fe citrate. Once the OD600 reached 1.0 - 1.4, cells were collected by centrifugation at 4000×g and rinsed 3× with 100 μM unbuffered EDTA. Subsequently cells were rinsed 3× with water and packed into EPR or Mössbauer cuvettes for analysis.

For cells from which mitochondria were isolated, 50 mL cultures were used to inoculate 1 L of growth medium. Once grown, these cultures were used to inoculate 24 L of medium in a custom glass bioreactor (ChemGlass) maintained at 30 °C. O_2 (99.99%) was bubbled through the bioreactor at 2 SCFM with a propeller rotation of 150 rpm. Cells were harvested at an OD600 of 1.0 – 1.4. Mitochondria were isolated as described [118] with EGTA (1 mM final concentration) present in all buffers. Samples were packed into EPR or Mössbauer cuvettes as described [230] and stored in LN_2 for subsequent analysis.

Spectroscopic Analysis

Mössbauer spectra were collected using a model MS4 WRC spectrometer (SEE Co, Edina MN) as described [117]. Parameters in the text are reported relative to α-Fe foil

at room temperature (RT). Applied magnetic fields were parallel to the gamma radiation. Spectra were simulated using WMOSS software. EPR spectra were collected on an X-band spectrometer (EMX, Bruker Biospin Corp., Billerica MA) with an Oxford Instruments ER910 cryostat. Spin quantifications used a 1.00 mM CuEDTA spin standard and SpinCount software (http://www.chem.cmu.edu/groups/hendrich). UV-vis spectra were collected at RT on a Hitachi 4400U spectrophotometer with a head-on photomultiplier tube. Spectra were analyzed as described for reduced heme *a*, *b*, and *c* content [119].

ICP-MS Analysis

Metal concentrations were determined by ICP-MS (Agilent model 7700x). Samples were packed into EPR cuvettes to determine the volume of the cell pellet (typically 200 - 300 μL). Following analysis by EPR, samples were diluted by a known factor while being transferred to a 15 mL screw-top tube containing 100 μL of concentrated trace metal grade HNO_3 (Fisher). Tubes were sealed with electrical tape to prevent evaporation, and then incubated overnight at 90° C. Digested samples were diluted with 7.8 mL double-distilled H_2O, and then analyzed by ICP-MS. *Double-distilled* means that the H_2O was house–distilled, deionized using exchange columns (Thermo Scientific 09-034-3), and distilled again using a sub-boiling still (Savillex DST-1000).

Fet3-GFP Expression Western Blot

Cells were grown to an OD(600) of 1.0 - 1.2 on minimal medium supplemented with 21 μM BPS and various concentrations of Fe under both fermenting and respirofermenting conditions. Cells were harvested by centrifugation at 4000×g, rinsed 3× with unbuffered EDTA (100 μM), then 3× with water. A portion of the resulting material was saved for Western blot analysis; the remainder was packed into EPR or Mössbauer cuvettes. Protein concentrations were measured and 60 μg protein of each sample were added per lane of the SDS-PAGE gel. Proteins were separated and transferred to a PVDF membrane as described [118]. The membrane was then incubated with antibodies against GFP and actin (Thermo Scientific) with the actin serving as a loading control. OxyBlot assays were performed as suggested by the manufacturer (Millipore).

Results

Iron-Deficient Cells

For this study, *iron-deficient* means that BPS was added to the growth medium to chelate endogenous unenriched Fe *and* that 1 μM $^{57}Fe^{III}$ citrate was subsequently added to enhance Mössbauer spectral intensity. Fe-deficient cells were grown with either glucose or galactose as the carbon source. Yeast cells exclusively ferment when grown on glucose whereas they both respire and ferment (called respirofermenting) when grown on galactose. In a previous study, we grew cells under respirofermenting

Table 4-1. Characteristics of isolated mitochondria and whole cells. Metal numbers, percentages used for Mössbauer spectral simulation, spin intensities of EPR signals, and concentrations of heme centers from UV-vis spectra. Percentages are based on corrected Mössbauer spectra where applicable. For fermenting mitochondria obtained from cells grown with 100 μM Fe in the medium, the two numbers listed for percentage refer to each of the two batches examined. EPR and ICP-MS data have been corrected for packing efficiency. Numbers in parenthesis represent number of trials (*n*) if different from 1. Estimated uncertainties in Mössbauer percentages are ± 4%, except for the sample obtained under Fe-deficient conditions in which the uncertainty is ± 7%. Uncertainties for EPR spin quantifications are ± 25%. Metal concentrations in cells have *not* been corrected for adventitious $[Fe^{2+}(BPS)_3]^{4-}$ bound on the cell's exterior.

Table 4-1 (Continued)

Whole Cells	**Respiro ferm.**	**Ferm.**	**Ferm.**	**Ferm.**	**Ferm.**	**Ferm.**	**Ferm.**
$[Fe]_{medium}$ (μM)	BPS + 1	BPS + 1	1	10	100	1,000	10,000
$[Fe]_{cell}$ (μM)	170 ± 50 (3)	240 ± 80 (3)	250 (1)	395 ± 40 (3)	470 ± 100 (3)	440 80 (3)	450 (1)
$[Cu]_{cell}$ μM)	62 ± 25 (3)	280 ± 20 (3)	---	26 ± 6 (3)	20 ± 6 (3)	35 ± 8 (3)	90 (1)
$[Mn]_{cell}$ (μM)	16 ± 7 (3)	17 ± 4 (3)	---	14 ± 4 (3)	17 ± 3 (3)	39 ± 10 (3)	30 (1)
$[Zn]_{cell}$ (μM)	160 ± 40 (3)	560 ± 70 (3)	---	600 ± 100 (3)	570 ± 70 (3)	1300 ± 130 (3)	300 (1)
NHHS Fe^{3+} (%)	~ 0	~ 0	40	76	80	75	84
CD (%)	43	36	22	18	10	5	3
NHHS Fe^{2+} (%)	39 (66 μM)	26 (62 μM)	26 (65μM)	7 (26 μM)	5 (23 μM)	6 (26 μM)	5 (22 μM)
Nanoparticles (%)	18	~ 0	12	~ 0	4	18	10
$[Fe^{2+}(BPS)_3]^{4-}$ (%)	12	35	N/A	N/A	N/A	N/A	N/A
g = 4.3 (μM)	~ 0	14	---	130	360	320	290
g = 2.0 region (μM)	26	14	---	16	15	28	27
Mitochondria	**Respiro ferm.**	**Ferm.**	**Ferm.**	**Ferm.**	**Ferm.**	**Ferm.**	**Ferm.**
[Fe] (μM)	300	480 ± 160 (2)	---	544 ± 70 (2)	710 (1)	840 ± 200 (3)	500
[Cu] (μM)	270	80	---	48 ± 13 (2)	52 (1)	60 ± 20 (3)	65
[Mn] (μM)	12	13	---	12 ± 3 (2)	11 (1)	10 ± 2 (3)	22
[Zn] (μM)	250	570	---	236 ± 100 (2)	350 (1)	450 ± 200 (3)	150
NHHS Fe^{3+} (%)	ND	< 15%	---	< 15%	51,0	---	---
CD (%)	63	59	---	11	12, 34	---	---
NHHS Fe^{2+} (%)	14	7	---	28	18, 36	---	---
HS Fe^{2+} Heme (%)	7	9	---	~ 0	~ 0	---	---
nanoparticles (%)	ND	< 10%	---	57	27	---	---
S = 0 $[Fe_2S_2]^{2+}$ (%)	ND	12	---	ND	ND	---	---
S = ½ $[Fe_2S_2]^{1+}$ (%)	ND	12	---	ND	ND	---	---
[g = 4.3] (μM)	ND	ND	---	20	20	28	---
[Heme *a*] (μM)	30	30	---	24, 43	27	13	23
[Heme *b*] (μM)	70	72	---	64, 58	78	21	40
[Heme *c*] (μM)	120	120	---	110, 129	130	40	97

conditions using minimal medium supplemented with 40 μM ^{57}Fe [119]. The Fe content (i.e. the types of Fe centers and percentages of each type) of those cells was essentially indistinguishable from that of cells grown on glycerol, a respiration-only carbon source. Thus, at the resolution of our experiments, respirofermentation essentially mirrors respiration. Growing cells on galactose is more convenient than growing them on glycerol, and so galactose-grown cells were used here. We will refer to BPS-treated fermenting and respirofermenting cells as *BPS-F* and *BPS-RF* cells, respectively.

Harvested BPS-F cells were rinsed with distilled and deionized water to remove $[Fe^{II}(BPS)_3]^{4-}$, and then packed into Mössbauer cups. The low-temperature, (6 ± 1 K) low-field (0.05 T) Mössbauer spectrum of these pinkish cells (see Appendix II, Figure A13, A) exhibited poor S/N due to the low concentration of ^{57}Fe. An unresolved resonance in the center of the spectrum dominated. Authentic $[Fe^{II}(BPS)_3]^{4-}$ exhibited a similar feature (Figure A13, B), suggesting that the BPS-F sample contained $[Fe^{II}(BPS)_3]^{4-}$ despite having been rinsed extensively. We subtracted the $[Fe^{II}(BPS)_3]^{4-}$ spectrum from that of the BPS-F cells, at 35% intensity, resulting in the spectrum of Figure 4-1B. Thus, only *ca.* 65% of the total Fe in the packed sample (Table 4-1; 240 μM × 0.65 = 156 μM) was due to Fe contained in the BPS-F cells. Parenthetically, the concentration of $[Fe^{II}(BPS]_3]^{4-}$ in the packed sample was substantially higher than the maximum possible concentration of $[Fe^{II}(BPS]_3]^{4-}$ in the medium (i.e. ~ 0.1 μM),

Figure 4-1. Mössbauer spectra (5 – 7 K, 0.05 T parallel field) of ^{57}Fe-enriched yeast cells at various $[Fe]_{med}$. A, BPS-RF; B, BPS-F; C, 1-F; D, 10-F; E, 100-F; F, 1000-F; and G, 10,000-F. Red lines are simulations assuming percentages given in Table 4-1. Spectrum B was obtained by subtracting a contribution of the $[Fe^{II}(BPS)_3]^{4-}$ spectrum from the raw spectrum (shown in Figure A13 A). Spectrum C has been published [172]. Red lines in B – F are four-term simulations assuming the CD (δ= 0.45 mm/sec, ΔEq = 1.15 mm/sec) and NHHS Fe^{II} doublets (δ= 1.3 mm/sec, ΔEq = 3.1 mm/sec), a mononuclear HS Fe^{III} sextet, and a nanoparticle doublet (δ= 0.5 mm/sec, ΔEq = 0.6 mm/sec). The HS Fe^{III} sextet was simulated using D = 0.5 cm^{-1}, E/D = 0.33, ΔE_Q = 0.10 - 0.14 mm/s, η =2.8, $A_0/g_N \cdot \beta_N$ = -238 kG, δ = 0.54 mm/s, Γ = 0.9 mm/s. Assumed temperature in C – G was 5, 6, 5, 7, and 6 K, respectively.

Figure 4-1 (Continued)

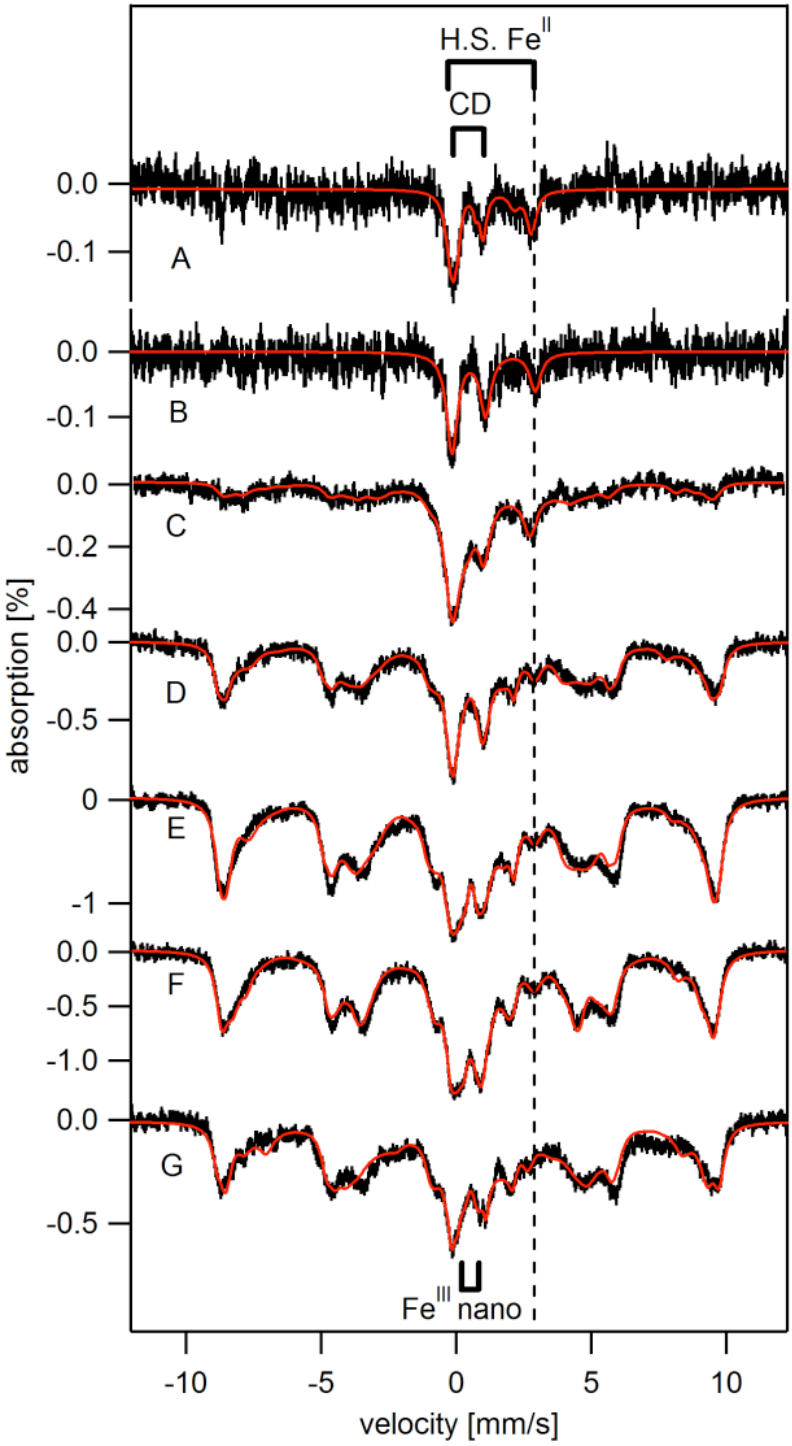

suggesting that $[Fe^{II}(BPS)_3]^{4-}$ collected on the cell's exterior. In principle, BPS could have penetrated the cell, but the charge on the complex probably discouraged this. Our packed pellets contain 70% cells and 30% buffer [172]. The concentrations in Table 4-1 have been corrected for this 0.7 packing efficiency.

The corrected BPS-F whole-cell Mössbauer spectrum was dominated by a quadruple doublet (δ = 0.45 mm/s, ΔE_Q = 1.15 mm/s) indistinguishable from the *Central Doublet* (CD) identified previously [116]. This doublet arises from S = 0 $[Fe_4S_4]^{2+}$ clusters and LS Fe^{II} heme centers [116]. A second prominent feature was a quadrupole doublet with parameters typical of nonheme high-spin (NHHS) Fe^{II} (δ = 1.2 mm/s and ΔE_Q = 3.1 mm/s). Percentages of these and all other spectral components are given in Table 4-1. We estimate that the CD- and NHHS Fe^{II} –associated species in BPS-F cells are present at *ca*. 90 and 60 μM Fe, respectively. No other features, including those from Fe^{III} oxyhydroxide (phosphate) nanoparticles or mononuclear HS Fe^{III} species, were evident, though minor contributions could have escaped detection due to the poor S/N ratio.

The corresponding Mössbauer spectrum of BPS-RF cells also exhibited poor S/N. In this case a 12% contribution of the $[Fe^{II}(BPS)_3]^{4-}$ spectrum was subtracted, affording the corrected spectrum shown in Figure 4-1A. The spectrum was similar to that of BPS-F cells, including major contributions from CD and NHHS Fe^{II} features. The absolute concentrations of these features were also similar (73 and 66 μM, respectively). A minor feature arising from HS Fe^{II} hemes may be evident in the BPS-RF spectrum, but the low S/N makes this assignment uncertain. In any event, the Mössbauer spectra of the

two BPS-treated samples were very similar despite the fact that cells were grown in different metabolic modes.

EPR spectra of BPS-F and BPS-RF cells were also similar. Both exhibited low-intensity signals in the g = 2 region from Mn^{II} ions, as evidenced by the hyperfine splitting arising from the I = 5/2 Mn nucleus (Figure 4-2, A and B). Such signals were observed in all whole-cell spectra (Figure 4-2, A - F) with similar intensities regardless of [Fe_{med}]. Also evident in the EPR spectra of BPS-F and BPS-RF cells were features at g ≈ 2.01, g ≈ 4.3, and minor features in the g = 6 region. The g = 4.3 signal is due to mononuclear HS Fe^{III} ions with E/D ~ 1/3. The features at g = 6.4, 6.0 and 5.4 originate from a partially-oxidized state of cytochrome *c* oxidase [116, 119, 231]. No signals from Cu ions were observed, despite the relatively high concentration of Cu in all 3 BPS-F samples examined. Most Cu ions in these cells are probably in the diamagnetic Cu^{I} state, though there may be other reasons for the EPR silence.

Mitochondria from Fe-Deficient Cells

The pinkish color of the BPS-treated cells was absent in the corresponding isolated mitochondria, indicating that the BPS-Fe complex that adhered to the cell exterior was removed during this process. The 6 K, 0.05 T Mössbauer spectrum of mitochondria isolated from BPS-F cells – called "*BPS-F mitochondria*" (Figure 4-3B) – was dominated by the CD. Also present was a feature exhibiting magnetic hyperfine interactions that probably arose from S = ½ $[Fe_2S_2]^{1+}$ clusters, e.g. the cluster in the Rieske protein associated with cytochrome bc_1 [232]. HS heme and nonheme Fe^{II} species

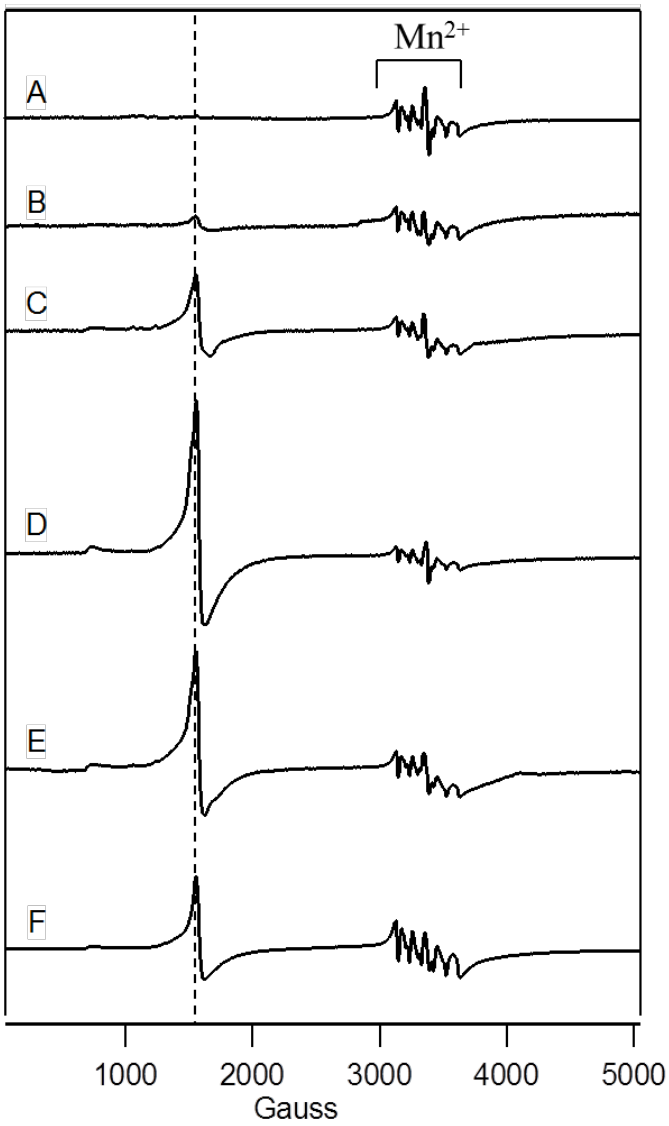

Figure 4-2. 10 K X-band EPR spectra of unenriched fermenting whole cells. A, BPS-RF; B, BPS-F; C, 10-F; D, 100-F; E, 1000-F; and F, 10,000-F. Other EPR conditions were: microwave frequency, 9.46 GHz; microwave power, 0.2 mW; modulation amplitude, 10 G; modulation frequency, 100 kHz; time constant, 335 sec; sweep time, 165 sec. The dashed line indicates g = 4.3.

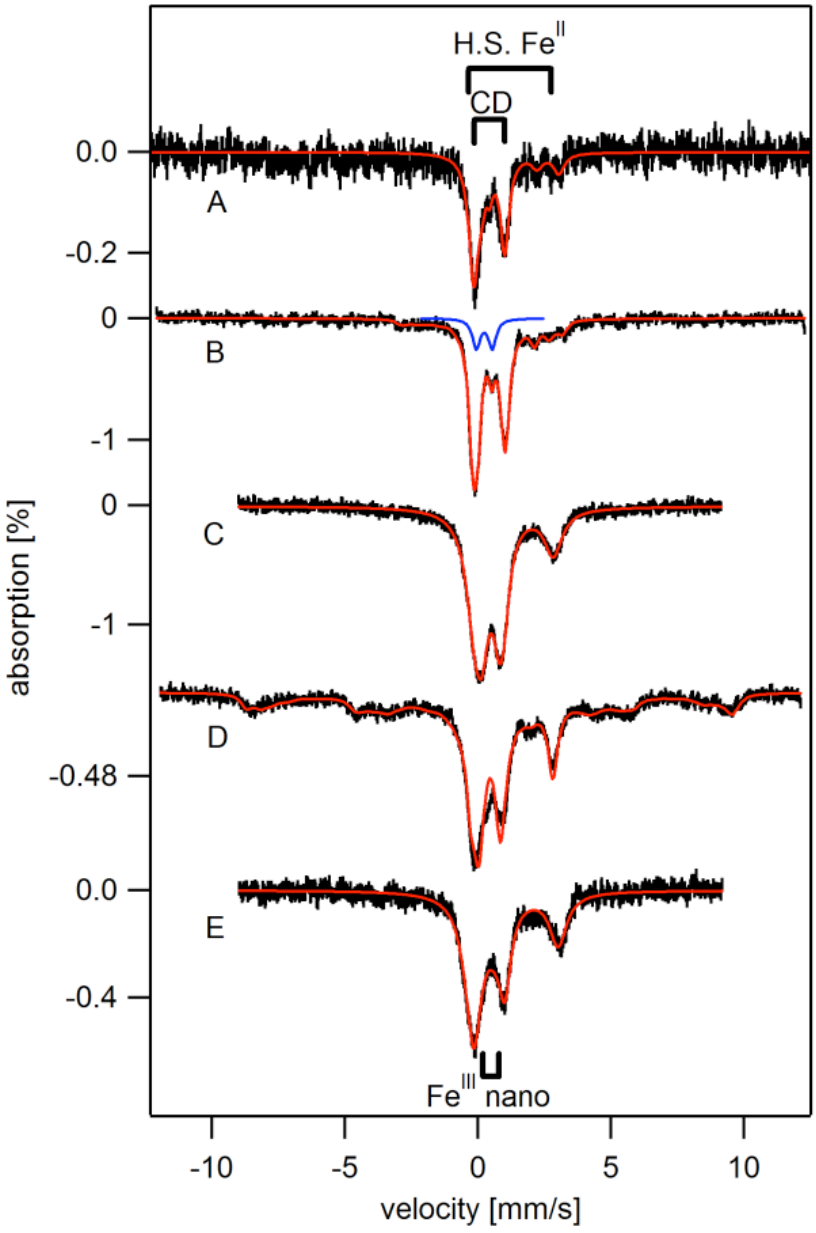

Figure 4-3. 6 K, 0.05 T Mössbauer spectra of isolated mitochondria. A, from BPS-RF cells; B, BPS-F cells; C, 10-F cells; D, 100-F cells; E, 100-F cells with 1 mM dithionite added in 0.6 M sorbitol and 0.1M Tris, pH 8.5. Red lines are simulations using percentages listed in Table 4-1. The blue line is a quadrupole doublet (δ = 0.3 mm/s; ΔE_Q = 0.6mm/s) typical of S = 0 $[Fe_2S_2]^{2+}$ clusters.

were also present, as evidenced by the high-energy lines of the associated quadrupole doublets in the spectra.

BPS-F mitochondria were largely devoid of Fe^{III} oxyhydroxide nanoparticles, as the doublet due to this species falls between the well-resolved lines of the CD. Indeed, the resolution between the CD lines was sufficient to discern a resonance near ~ 0.6 mm/s that was assigned to the high-energy line of a quadrupole doublet arising from S = 0 $[Fe_2S_2]^{2+}$ clusters. The blue line in Figure 4-3B is a simulation of that doublet. Such clusters in the oxidized diamagnetic 2+ state have not been observed previously in any Mössbauer spectra of mitochondria, perhaps because previous spectra inevitably included contributions from nanoparticles [118, 119] which absorb in the same region. The absence of intense NHHS Fe^{II} and nanoparticle doublets rendered the BPS-F spectrum more reminiscent of that obtained from 40-RF mitochondria [119], which also lacked these doublets, than from the spectrum of 40-F mitochondria which included them. However, even in 40-RF mitochondria, no feature arising from S = 0 $[Fe_2S_2]^{2+}$ clusters was discerned. Percentages used to fit the Figure 4-3B spectrum are given in Table 4-1.

The UV-vis spectrum of BPS-RF and BPS-F mitochondria (Figure 4-4, A and B) exhibited features due to Fe^{II} heme centers. The concentrations of reduced hemes *a*, *b*, *c* (Table 4-1) were similar to those reported for 40-R mitochondria [119]. The 10 K X-band EPR spectrum of BPS-RF and BPS-F mitochondria (Figure 4-5, A and B) exhibited low-intensity signals at g = 6.5, 5.4, and 4.3. The first two signals probably arose from the a_3:Cu_b site of cytochrome *c* oxidase [231], while the g = 4.3 signal arose from a rhombic HS Fe^{III} species in BPS-F mitochondria. The g = 2 region lacked the Mn^{II} signal that was

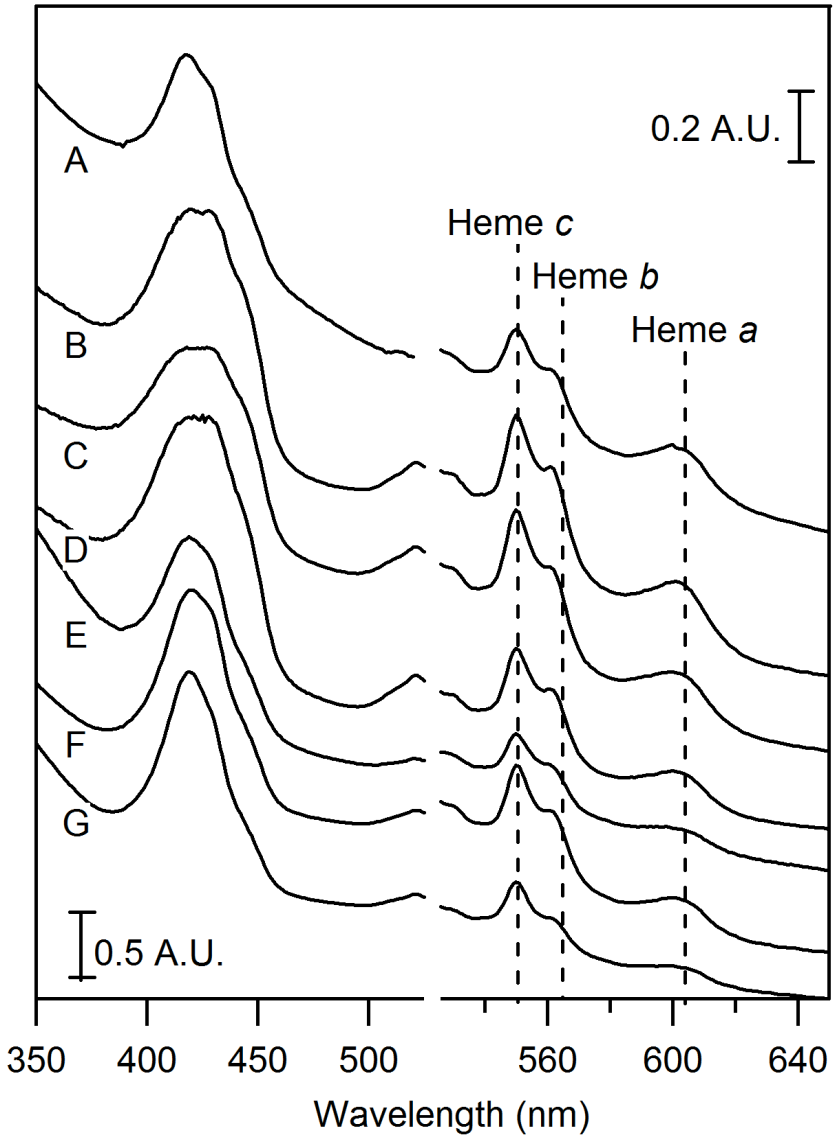

Figure 4-4. UV-vis spectra of isolated mitochondria. A, BPS-RF; B, BPS-F; C, 10-F; D, 100-F; E, 1000-F; F, 10-F from a second batch; G, 10000-F from the second batch.

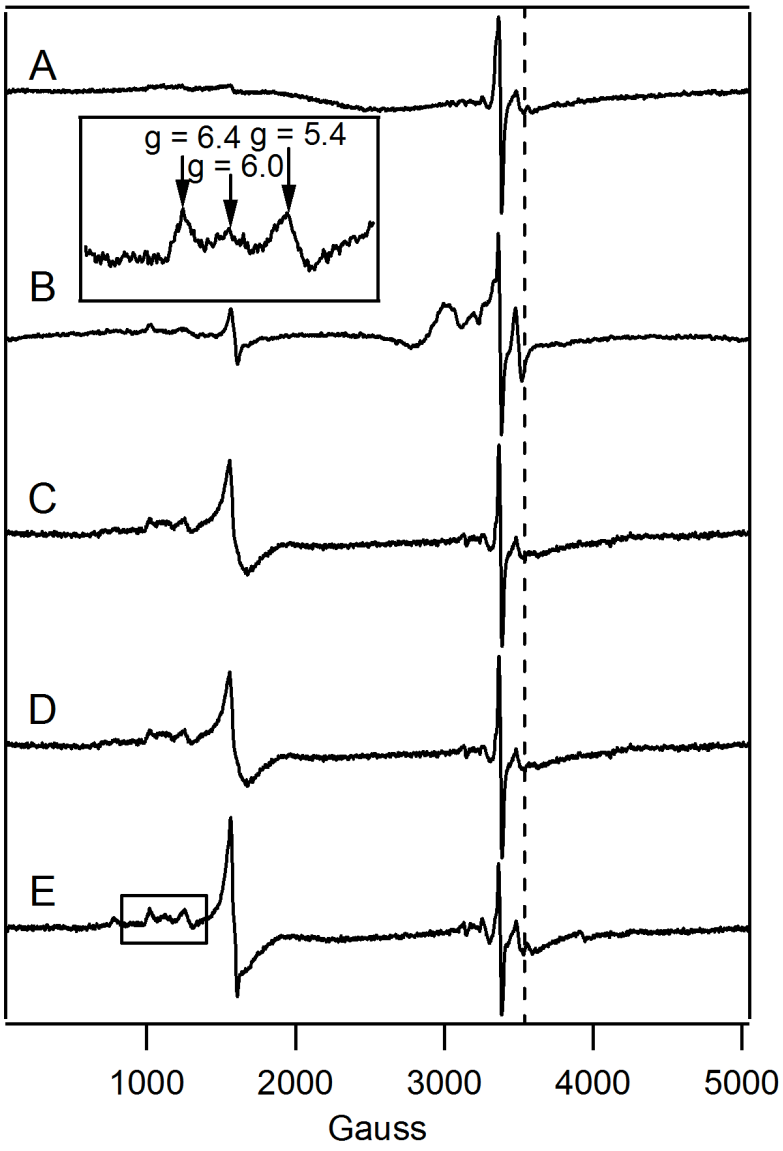

Figure 4-5. EPR of isolated mitochondria. A, BPS-RF; B, BPS-F cells; C, 10-F cells; D, 100-F cells; and E, 1000-F cells. Spectrum A is matched to Figure 4-3A; spectrum B is matched to spectrum 3B. EPR conditions were as in Figure 4-2. The dashed line indicated g = 1.94.

evident in whole-cell spectra, indicating that the ions affording that signal are not located in mitochondria.

Fe-Sufficient Cells and Mitochondria

For comparison, we examined fermenting cells grown on medium supplemented with 1 μM (with no BPS) and 10 μM ^{57}Fe. Mössbauer spectra of *1-F* and *10-F* cells (Figure 4-1, C and D) exhibited features due to mononuclear HS Fe^{III}, the CD, NHHS Fe^{II}, and Fe^{III} oxyhydroxide nanoparticles (percentages given in Table 4-1). The main difference in these spectra was in the percentage of the HS Fe^{III} sextet. For 10-F cells, this percentage was more than *double* that in the 1-F spectrum. This feature undoubtedly arose from Fe within isolated vacuoles [120], indicating that vacuolar Fe is essentially absent in BPS-F and BPS-RF cells and that it starts to accumulates as cells grow in medium containing 1 - 10 μM Fe. ICP-MS analysis indicated that ~100 μM of the Fe in 1-F cells and ~300 μM Fe in 10-F cells were associated with vacuoles. This corresponded to 40% and 76% of cellular Fe, respectively.

EPR spectra of 10-F cells (Figure 4-2C) were generally similar to those of BPS-RF and BPS-F cells (Figure 4-2, A and B), except for a more pronounced $g \approx 4.3$ signal. This is consistent with an increased concentration of the vacuolar mononuclear HS Fe^{III} species in the 10-F cells.

Interestingly, the absolute concentration of NHHS Fe^{II} ions in the cells (obtained by multiplying the cellular Fe concentration by the fractional Mössbauer intensity) *declined significantly* (3-fold) as [Fe_{med}] *increased* from 1 → 10 μM. The average

NHHS Fe^{II} concentration was 64 ± 2 μM in the BPS-F, BPS-RF and 1-F samples, and 24 ± 2 μM in the 10-F, 100-F, 1000-F and 10,000-F cells (Table 4-1).

The low-temperature, low-field Mössbauer spectrum of 10-F mitochondria (Figure 4-3C) was nearly indistinguishable from that of 40-F mitochondria [118]. Relative to BPS-RF and BPS-F mitochondria, 10-F mitochondria exhibited considerably more Fe^{III} oxyhydroxide nanoparticles (Table 4-1). UV-Vis (Figure 4-4C) and EPR (Figure 4-5C) spectra of 10-F mitochondria were also similar to those of 40-F mitochondria [119]. The UV-Vis spectrum exhibited Fe^{II} heme concentrations similar to those seen in the BPS-F sample (Table 4-1). The concentration of Fe in the 10-F sample was reduced relative to in the 40-F sample.

Fe-Overload Conditions

The Fe concentrations in 100-F, 1000-F and 10,000-F cells were similar to each other and to that of cells grown on 10 μM Fe (Table 4-1), despite the 1000-fold range of [Fe_{med}]. The Mössbauer spectra of these cells (Figure 4-1, E - G) were also remarkably similar to each other and to spectra of 40-F cells; they exhibited similar contributions of the CD, the NHHS Fe^{II} doublet and Fe^{III} nanoparticles. 100-F cells contained a slightly lower concentration of Fe^{III} nanoparticles relative to the other two samples. However, no general trend was apparent, in that the 1000-F sample exhibited a higher concentration of Fe^{III} nanoparticles than did 10,000-F cells. The main point is that *a 250-fold change in [Fe_{med}] (from 40 → 10,000 μM) had little effect on the concentration or distribution of*

Fe within fermenting cells. The only noticeable exception was a gradual but significant decline of the CD intensity as [Fe_{med}] increased (Table 4-1).

100-F, 1000-F and 10,000-F cells exhibited EPR spectra (Figure 4-2, C - E) similar to those of 10-F cells, except for more intense g ≈ 4.3 signals. Spin concentrations of the g = 4.3 signal (Table 4-1) represented ~70% of the Fe concentration associated with the HS Fe^{III} sextet in the corresponding Mössbauer spectra. Although not a perfect match, this percentage indicates an acceptable congruence between the two types of measurements.

The 5K, low-field Mössbauer spectra of isolated 10-F (Figure 4-3C), 40-F [118], and 100-F mitochondria (Figure 4-3D) all included the CD, a HS Fe^{II} doublet, and a doublet due to Fe^{III} nanoparticles in approximately the same relative amounts. The 100-F sample also exhibited a sextet due to mononuclear HS Fe^{III} species representing *ca*. 40% of the spectral intensity. 40-F mitochondria exhibited a similar feature but representing just 15% of spectral intensity [118].

The greater intensity of the sextet in the 100-F mitochondria spectrum prompted us to consider whether the additional HS Fe^{III} ions were located in the mitochondria or whether they were an artifact of purification and bound on the exterior of the organelle. To address this, we isolated a second batch of 100-F mitochondria including the reductant dithionite in the buffer. Dithionite does not appear to penetrate mitochondrial membranes [118]. The resulting spectrum (Figure 4-3E) showed no evidence of the sextet, suggesting that most or all of the Fe associated with this feature in first sample was

artifactual. The expense associated with preparing ^{57}Fe-enriched 100-F mitochondria from 24 L of cells prohibited us from exploring this issue further.

100-F and (unenriched) 1000-F mitochondria exhibited the same EPR signals with about the same relative intensities (Figure 4-5, D and E). 10-F (Figure 4-5C) and 40-F [119] mitochondria exhibited very similar spectra. Importantly, the intensities of the g = 4.3 signal in the 100-F and 1000-F spectra were not higher than those in the 10-F or 40-F spectra. This is further evidence that the more intense HS Fe^{III} sextet observed in Mössbauer spectra of one batch of 100-F mitochondria was an artifact of that particular preparation. We conclude that the Fe content of 10-F, 40-F and 100-F mitochondria is approximately the same.

A 100-F mitochondria sample exhibited a UV-Vis spectrum (Figure 4-4D) similar to that of 10-F mitochondria (Figure 4-4C) while a 1000-F sample (Figure 4-4E) showed diminished intensities (heme concentrations are given in Table 4-1). To address whether this decline reflected a cellular response to toxic levels of Fe in the growth medium, we isolated two batches of mitochondria, from cells grown with 10 (control) and 10,000 μM [Fe_{med}] in the growth medium. Both batches of cells grew at nearly the same rate; i.e. the 10,000 μM sample showed essentially no sign of toxicity. Oxyblot analysis of extracts of the two organelles (Appendix II, Figure A14) indicated just 10% more ROS damage in the 10,000-F sample relative to the 10-F sample. ICP-MS analysis indicated insignificant differences in the concentration of Fe in the organelles (Table 4-1). However, corresponding UV-vis spectra indicated a decline in reduced heme intensities (Figure 4-4, F and G, and Table 4-1). The decline of heme intensity in Figure

4-4 E and G appears to be real. We conclude that Fe concentrations in the growth medium as high as 10,000 μM Fe^{III} citrate have insignificant effects on the growth rate of the cell, the level of ROS damage, and the Fe concentration of cells and their mitochondria and vacuoles. However, there does appear to be a decline in the level of $[Fe_4S_4]^{2+}$ clusters Fe^{II} hemes at very high $[Fe_{med}]$.

Fet3-GFP Expression Levels in Fermenting and Respirofermenting Cells

The DY150, FET3-GFP::KanMX strain biosynthesizes the green fluorescent protein (GFP) fused to Fet3p [228]. We used this strain to perform a Western blot using an antibody against GFP as a reporter for Fet3p expression. The analysis was performed on cells grown under fermenting (and BPS-RF) conditions and supplemented with various concentrations of Fe in the growth medium. Fet3p was detected only in the BPS-F sample (Figure 4-6, right-most lane). Three bands were observed, with the middle band displaying the highest density and the upper band ~ 7-times less intense but visible nevertheless. Since bands were not visible in any other lane, the concentration of Fet3-GFP in the BPS-F sample appears to have been *at least* 10-times greater than in the other samples, assuming no threshold effects. This suggests that the Aft1-controlled Fe regulon was effectively shut down when cells were grown in medium containing > *ca*. 1 μM of Fe. Fe-deficient respirofermenting cells do not appear to utilize the Fe regulon, as no Fet3p expression was observed.

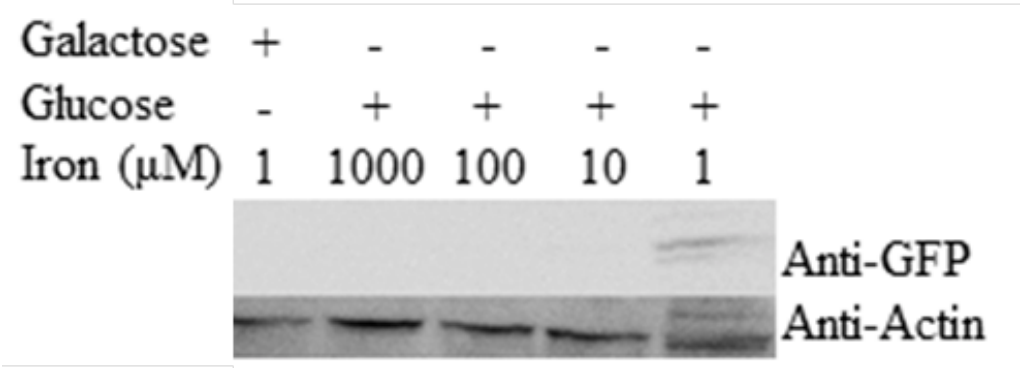

Figure 4-6. Western blot of Fet3-GFP cells grown at various conditions. Actin was added as a loading control. BPS was added to all samples.

Discussion

The Fe-Deficient State

Fermenting WT yeast cells grown under Fe-deficient conditions prioritize their use of Fe for essential functions. Such cells were devoid of vacuolar HS Fe^{III}, a storage form of Fe that is not essential, and were largely devoid of Fe^{III} oxyhydroxide (phosphate) nanoparticles, which do not seem to function in cellular Fe metabolism. Fe-deficient cells had a total Fe concentration of *ca*. 150 μM, distributed into two major groups. About 80 μM was present as S = 0 $[Fe_4S_4]^{2+}$ clusters and LS Fe^{II} hemes (the two types of Fe cannot be distinguished by Mössbauer), most of which are undoubtedly associated with mitochondria and respiration. About 60 μM cellular Fe corresponded to NHHS Fe^{II} species. About the same distribution of Fe was observed in both fermenting and respirofermenting Fe-deficient cells.

Mitochondria from Fe-deficient fermenting and respirofermenting cells also prioritize their use of Fe; they contained similar levels of respiratory complexes relative to Fe-sufficient mitochondria, but lower concentrations of nanoparticles and NHHS Fe^{II}/Fe^{III} species. This distribution was more typical of Fe-sufficient mitochondria from *respiring* cells [119]. We previously proposed that the NHHS Fe^{II} and Fe^{III} species in mitochondria are in equilibrium with each other and with the nanoparticles contained therein, and that the NHHS Fe^{II} species constitutes a pool of Fe used for heme and Fe/S cluster biosynthesis [118]. This size of this pool declines in respiring mitochondria, which is consistent with the higher rates of Fe/S cluster and heme biosynthesis. The lower

concentrations of this pool observed in Fe-deficient mitochondria might arise instead from a diminished rate of Fe *import* from the cytosol into mitochondria due to Fe-deficient conditions.

A Non-Mitochondrial NHHS Fe^{II} Pool

The concentration of NHHS Fe^{II} in isolated Fe-deficient mitochondria was ~ 40 μM. What proportion of the NHHS Fe^{II} pool observed in whole cells is due to the NHHS Fe^{II} species in mitochondria? Mitochondria in fermenting cells occupy between 3% and 10% of cell volume [233]. This means that the concentration of mitochondrially-associated NHHS Fe^{II} species in Fe-deficient cells is 1.2 - 4 μM (i.e. 40 μM × (0.03 to 0.1)). Since the observed concentration of NHHS Fe^{II} in Fe-deficient whole cells was ~ 60 μM, we conclude that > 90% of the NHHS Fe^{II} in whole cells is *not* located in mitochondria. Nor does this non-mitochondrial pool appear to be located in vacuoles [120]. As a working hypothesis, we propose that the pool of NHHS Fe^{II} in Fe-deficient cells is located in the cytosol.

Decrease in Non-Mitochondrial NHHS Fe^{II} as $[Fe_{med}]$ Increases

Under Fe-sufficient and Fe-overload conditions, mitochondria contained ~ 150 μM NHHS Fe^{II} – a 3-fold increase relative to under Fe-deficient conditions. Under these high-Fe conditions, our calculations suggest that as much as 60% of the NHHS Fe^{II} species present in whole cells is now located in mitochondria. Thus, the decline of non-mitochondrial NHHS Fe^{II} as cells transition from being Fe-deficient to Fe-sufficient (60

→ 25 μM) is more dramatic than implied by the ratio 60:25. These results suggest that during the transition from 1 → 10 μM [Fe_{med}], most of the non-mitochondrial (probably cytosolic) NHHS Fe^{II} species of whole Fe-deficient cells moves into the mitochondria where they contribute to the NHHS Fe^{II} pool (and ultimately nanoparticles) in this organelle.

Occurring in approximately the same transition period was a decline in the expression of the Fe regulon as reported by Fet3p, confirming previous studies that Aft1-dependent expression of the Fe regulon is effectively abolished at > 1 μM [Fe_{med}] [203, 234]. The low-affinity pathways play the major role in regulating cellular Fe beyond this transition. The transition of non-mitochondrial NHHS Fe^{II} into the mitochondria (or vacuoles) might be related to the switch from high- to low-affinity Fe regulatory mechanisms or to the activation of CCC1.

Accumulation of Vacuolar Fe

The lack of vacuolar Fe in Fe-deficient cells is probably due to the lack of Ccc1p on the vacuole membrane caused by destabilization of CCC1 mRNA by Cth1p/2p under Fe-deficient conditions (the process also requires Aft1p/2p) [235]. Cth1p/2p also destabilize the mRNA of genes involved in Fe/S cluster and heme biosynthesis and the mRNA of numerous Fe/S-containing and heme-containing proteins. Our results support previous studies regarding the effects of Cth1p/2p on CCC1p, but do *not* indicate lower concentrations of Fe/S cluster or heme centers in Fe-deficient cells or mitochondria. This is probably because we supplemented the BPS-treated medium with 1 μM ^{57}Fe (to allow

Mössbauer analysis), which rendered our cells less rigorously Fe-deficient than the BPS-treated cells of Thiele and coworkers [213]. We suspect that their Fe-*starved* cells shut down Fe/S cluster and heme assembly in a final attempt to survive.

CCC1 gene expression increases dramatically between [Fe_{med}] = 5 - 50 μM [213], consistent with the increased level of vacuole Fe that we observed as [Fe_{med}] increased. In this case, the increased CCC1 expression level is probably due to Yap5p, an Fe-inducible transcription factor. As the concentration of Ccc1p on the vacuolar membrane increases, vacuoles import Fe such that the vacuoles in cells grown on 1, 10 and 40 μM Fe are ca. 0, 40%, and 100% filled.

The concentration of Fe that can be associated with vacuoles maximizes between 300 - 350 μM. We have previously estimated that the Fe concentration in vacuoles in cells grown on 40 μM Fe is ~ 1.2 mM, based on the assumption that these organelles occupy *ca*. 25% of cell volume [118, 172]. Our results indicate that cells limit the storage of HS Fe^{III} in vacuoles to this cellular Fe concentration, regardless of the concentration of Fe in the growth medium. Whether they do this by limiting the percentage volume of vacuoles in the cell and/or the concentration of mononuclear HS Fe^{III} contained therein is uncertain.

The total Fe concentration in fermenting cells is also limited, with a minimum of ca. 160 μM in Fe-deficient cells. This concentration gradually increasing as vacuoles fill and other changes occur, maximizing at *ca*. 450 μM in cells grown in Fe-overloaded medium. The increase in cellular Fe concentration is largely (but not entirely) due to the vacuoles filling with Fe, suggesting that the [Fe] of all *non-vacuolar* Fe components of

the cell are roughly invariant (at ~ 160 μM) during this process. The majority of this invariant portion of cellular Fe is mitochondrial.

Modest Changes in the Fe Distribution in the Cells Grown on Fe-Overloaded Medium

The concentration of Fe in cells and the distribution of that Fe into different groups is roughly invariant over a 250-fold range of [Fe_{med}] (40 → 10,000 μM). In this region, Fe is being imported via low-affinity pathways. The invariant Fe concentration suggests that the low-affinity pathway must be saturated throughout this 250-fold interval. The Fe import velocity might be saturable, in which case a Michaelis-Menten-like expression with $K_{m\text{-}app}$ ~ 15 μM Fe could simulate this effect. This is within a factor of 2 of previous estimates of the apparent K_m for the low-affinity transporter [206, 211, 212]. Our results also reveal why WT yeast cells grow well under high-Fe (5 – 10 mM) conditions – namely because they prevent excess environmental Fe from being imported (rather than, for example, having special mechanisms to detoxify excess imported Fe).

Two modest but noticeable changes in the Fe distribution of such cells were a decline in the concentration of Fe associated with the Mössbauer central doublet and heme centers as [Fe_{med}] increased. Under Fe-deficient conditions, the cellular CD concentration was ca. 80 μM whereas with [Fe_{med}] = 1, 10, 100, 1000 and 10,000 μM, it was 55, 71, 47, 22 and 14 μM, respectively. UV-Vis spectra also showed some decline in heme features at high medium Fe concentration. These declines might reflect a decline in the fractional cellular volume occupied by mitochondria or a decline in the

concentration of Fe-rich respiratory complexes. More extreme declines of these centers under even higher medium Fe concentrations might be responsible for the Fe-associated toxicity that is eventually observed.

Cellular Manganese

Comparing the ICP-MS-detected Mn concentrations to the spin concentrations of the Mn-associated EPR signal (Table 4-1, "g = 2.0 region") indicates that the majority of Mn ions in the cells are mononuclear Mn^{II} species that exhibit(s) the EPR signal. This differs from the study of Chang and Kosman [236] who reported that the majority of cellular Mn is EPR-silent. McNaughton et al. used ENDOR spectroscopy to investigate the species affording this signal [237] and determined that > 70% of the contributing species are Mn^{II} ions coordinated with phosphate and/or polyphosphate anions. The absence of these signals in isolated mitochondria and vacuoles [120] suggests that these Mn^{II}(phosphate/polyphosphate) species are *not* located in either of these organelles. The concentration of Mn^{II}(phosphate/polyphosphate) species in our fermenting yeast cells appears to be 10 – 30 μM, regardless of $[Fe_{med}]$.

Summary Model

The major results of this study can be summarized by the model of Figure 4-7. The high-affinity Fe import pathway operates when $[Fe_{med}] \leq$ *ca*. 1 μM (BPS-treated plus 1 μM ^{57}Fe). Under these conditions, the cell is Fe-deficient and must prioritize its use of Fe. Most of this precious commodity goes to the mitochondria where it is

assembled into Fe/S clusters and heme centers, prosthetic groups that are critical for cellular metabolism. Little Fe is stored in vacuoles and little is present as Fe^{III} nanoparticles. A significant portion of cellular Fe in Fe-deficient cells is in the form of NHHS Fe^{II} and is probably located in the cytosol. At $[Fe_{med}] \sim 10$ μM, the high-affinity pathway is shut-down and Fe is regulated by low-affinity pathways. The mitochondria remain the site where much imported Fe is sent for Fe/S cluster and heme synthesis. Additional Fe is imported (perhaps from the cytosolic pool of NHHS Fe^{II}), increasing the pool of mitochondrial NHHS Fe^{II} and Fe^{III} oxyhydroxide nanoparticles. Cytosolic NHHS Fe^{II} species declines as some becomes stored in vacuoles as nonheme HS Fe^{III} species. When $[Fe_{med}] = 40 – 10{,}000$ μM, the vacuoles are filled with Fe, and little else changes in terms of Fe content and distribution. The low-affinity import pathways are saturated in accordance with apparent K_m 15 - 30 μM, limiting Fe import at this $[Fe_{med}]$ concentration and higher. This prevents high concentrations of environmental Fe from entering the cell and causing toxicity. These regulatory properties allow fermenting yeast cells to grow on medium with Fe concentrations that *vary over 4 orders of magnitude*, an impressive feat by any standard!

Figure 4-7. Model of Fe distribution and regulation in fermenting yeast cells. Top, Fe-deficient; middle, Fe-sufficient; bottom, Fe-loaded. The concentration of Fe^{III} citrate in the growth medium (in μM) is indicated by the brown squares. Two import pathways are shown, including the high-affinity pathway (Aft1 regulating the iron regulon including Fet3p) and the low-affinity pathway (Fet4p-based). Also shown are mitochondria (blue rectangular shape) and vacuoles (red sphere). Under *Fe-deficient* conditions, Fe is imported via the high-affinity pathway; a portion is imported into mitochondria where Fe/S clusters (brown cube) and heme centers (disks) are predominantly made. Most of the rest of the imported Fe is present as a non-mitochondrial NHHS Fe^{II} pool (shown here in the cytosol, but this is not known). Aft1p is sensing a small portion of this pool. The vacuoles are empty because Cth2 working with Aft1p is activated by the absence of cytosolic Fe to degrade CCC1 mRNA. Under *Fe-sufficient* conditions, the high-affinity pathway is shut-down and the majority of Fe is imported via the low-affinity pathway. The concentration of nonmitochondrial NHHS Fe^{II} is reduced 3-fold, perhaps because a portion is imported into mitochondria and converted to nanoparticles (clumps of brown circles) and NHHS Fe^{II} and Fe^{III}. The vacuoles are partially filled with mononuclear HS Fe^{III} species, due to the absence of the Cth2 effect and the presence of Yap5p-dependent expression of CCC1. Under *Fe-overload* conditions, the Fe content is similar to that under Fe-sufficient conditions except that the vacuoles are filled completely. The low-affinity import pathway is saturable such that a 250-fold change in the Fe concentration of the medium does not significantly impact the cellular Fe content.

Figure 4-7 (Continued)

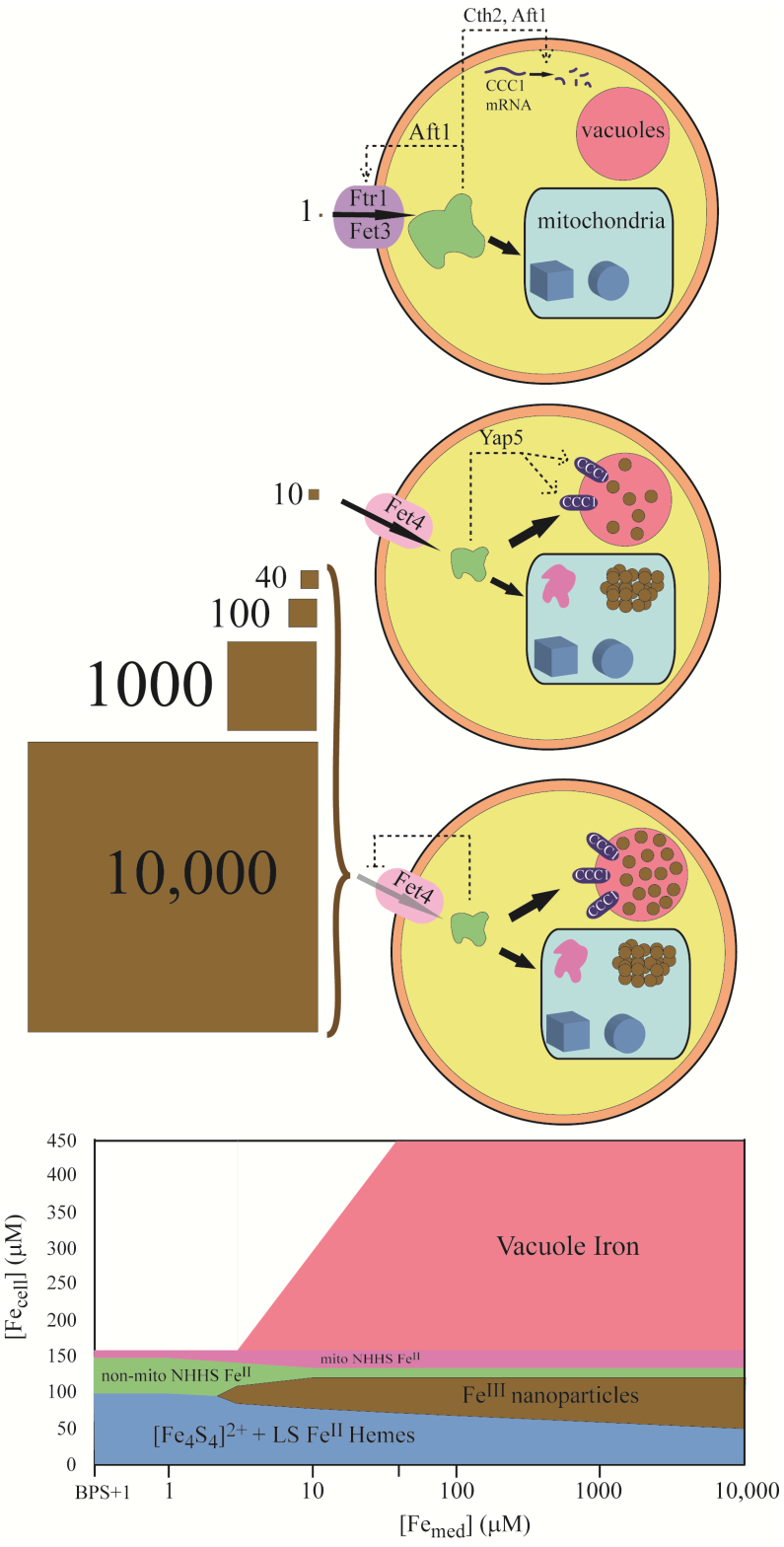

CHAPTER V

SUMMARY AND FUTURE STUDIES

Summary

The major objective of this dissertation has been to study iron trafficking, distribution, and speciation in Jurkat cells and *Saccharomyces cerevisiae.* An integrative biophysical and bioanalytical approach, centered on Mössbauer spectroscopy has been successfully adopted, for the first time, in the detailed study of iron in Jurkat whole cells and isolated mitochondria. The first objective of this dissertation, described in Chapter II, was to characterize the iron distribution and speciation in wild-type Jurkat cells and isolated mitochondria grown in glucose-containing medium, supplemented with 10 μM ferric citrate. Procedures were established and optimized for the large-scale (up to 24 liters) growth of Jurkat cells in a bioreactor, and the anaerobic isolation of 'pure' and intact mitochondria from Jurkat cells. Isolated mitochondria were analyzed by transmission electron microscopy and Western blot analysis for intactness and purity. The packing efficiencies (defined as the percentage of a packed sample due to the sample only, excluding interstitial buffer) of whole cells and isolated mitochondria were also determined by use of a fluorescent dye. Packing efficiencies allowed us to calculate the absolute concentration of Fe in samples in μM, rather than having to rely on ratios of [Fe]: [protein] for quantification of cellular iron.

Mössbauer spectroscopy revealed that, in whole intact cells, the majority of Fe was associated with ferritin or the Central Doublet (CD), which consists of $[Fe_4S_4]^{2+}$ clusters and low-spin hemes. A significant amount of ferric nanoparticles was also found to accumulate in Jurkat cells under the growth conditions studied, and the large majority of the nanoparticles appeared to accumulate in the mitochondria. The presence of these ferric nanoparticles was confirmed using EPR and high-field Mössbauer spectroscopies, and was indicative of iron overload. The Mössbauer spectra of isolated mitochondria were dominated by the CD and the ferric nanoparticles, and were largely devoid of ferritin-bound Fe. A significant level of NHHS Fe^{II} (~5-10 fold greater than previously reported) was also detected in whole Jurkat cells and isolated mitochondria. UV-Vis spectroscopy revealed significant levels of reduced hemes *a*, *b*, and *c* in intact Jurkat cells and in anaerobically isolated mitochondria. EPR spectroscopy of isolated mitochondria allowed us to quantify the amount of Fe present in various respiratory complexes, such as succinate dehydrogenase, cytochrome bc_1, and cytochrome *c* oxidase, whereas ICP-MS provided absolute concentrations of Fe and other metals, such as Mn, Cu, and Zn. By integrating all the information provided by our biophysical and bioanalytical methods, a 'snapshot' of the iron distribution and speciation in Jurkat cells was obtained (Figure 2-7), whereby the iron-containing species associated with the mitochondria were distinguished from those found in cellular compartments outside the mitochondria.

We were intrigued by the presence of ferric nanoparticles in our samples, since such a form of iron was never before found to accumulate in mammalian cells. Our next

objective, described in Chapter III, was to study, in more detail, the conditions of growth that affected the formation of ferric nanoparticles. We again relied heavily on Mössbauer spectroscopy to study the formation of these ferric nanoparticles. We observed that cells grown on increasing concentrations of ferric citrate (FC) accumulated significant amounts of iron, mainly in the form of ferric nanoparticles. Mitochondria isolated from these cells did not accumulate more than ~1000 μM Fe, and the additional ferric nanoparticles, which were found to be ferric phosphate, accumulated mostly in the cytoplasm, as suggested by EDX EM images. The concentrations of other iron-containing species, such as ferritin, Fe/S clusters, and hemes did not vary significantly with increase in FC in the growth medium. Furthermore, ferritin in cells accumulating ferric phosphate nanoparticles was only partially loaded with Fe. We grew cells with galactose instead of glucose to study the effect of switching to a carbon source that favors mitochondrial respiration. Galactose-grown cells were found to suffer more ROS damage, and also accumulate more ferric phosphate nanoparticles than glucose-grown cells. However, the level of ROS damage, under either carbon source, did not increase with increased nanoparticle formation, suggesting that there was no correlation between nanoparticle formation and ROS damage. The increased nanoparticle formation in galactose vs. glucose grown cells could be a result of metabolic differences, and possibly differences in growth rate.

Cells grown on increasing concentrations of transferrin-bound iron (TBI) accumulated significantly less iron than cells grown with FC. The large majority of the iron was either associated with ferritin, or with the Central Doublet of the Mössbauer

spectra, even when we overexpressed the transferrin receptor (TfRC1) in Jurkat cells. This is because TBI uptake is a lot more tightly regulated than FC uptake. TfRC1-overexpressing cells only started accumulating significant levels of ferric nanoparticles when grown on higher concentration of TBI. Cytosolic labile Fe is presumably sensed by the IRP1/2 system (for ferritin regulation), and also by PCBP1/2 (for Fe loading into ferritin). Fe uptake via the TBI pathway appeared to favor excess Fe storage in ferritin whereas FC uptake tended to lead to more ferric nanoparticle formation. However, even in TBI grown cells, ferritin was still only partially loaded. Furthermore, ferritin protein upregulation, in response to increased intracellular Fe, appeared to be more sensitive to iron originating from TBI uptake than from FC uptake. These results suggest that the cytosolic labile form of Fe that accumulates in Jurkat cells through TBI pathway may differ chemically (in terms of ligands bound) from the labile form of Fe that accumulates through the FC pathway. We also knocked-down frataxin protein in Jurkat cells, and observed an increase in ferric nanoparticle formation in frataxin-deficient cells. We developed a mathematical model centered on parameters and processes depicted in Figure 3-11, to simulate the accumulation of various Fe-containing species in Jurkat cells grown under the various conditions studied. Using the model, we were able to predict the time-dependence of Fe accumulation in frataxin-deficient cells (Figure 3-12).

Iron content of fermenting *Saccharomyces cerevisiae* cells under iron-deficient and iron-overload conditions was also studied as described in Chapter IV. The high-affinity Fe import pathway was active only in Fe-deficient cells, indicating that Aft1-dependent expression of the Fe regulon was essentially non-existent at > 1 μM Fe in the

medium. At higher [Fe] in the medium, low-affinity iron transporters are presumed to play a greater role in iron import than the high-affinity Fe import pathway. Fe-deficient cells contained primarily nonheme high-spin (NHHS) Fe^{II} species (most of which was not located in the mitochondria) and mitochondrial Fe. Mitochondria isolated from Fe-deficient cells contained $[Fe_4S_4]^{2+}$ clusters, low- and high-spin hemes, S=½ $[Fe_2S_2]^{1+}$ clusters, NHHS Fe^{II} species, and $[Fe_2S_2]^{2+}$ clusters. The presence of $[Fe_2S_2]^{1+}$ clusters was not observed in previous *Saccharomyces cerevisiae* samples [117-119, 139, 172] since the Mössbauer spectra were obscured by the presence of Fe^{III} nanoparticles. The absence of nanoparticles allowed such clusters to be observed in Fe-deficient cells.

Fe-deficient cells were found to prioritize their use of Fe to essential forms, and were devoid of nanoparticles and vacuolar Fe. As iron concentration was increased in the growth medium 250-fold, fermenting cells accumulated no more than 400 – 450 μM Fe. However, the concentration of non-mitochondrial NHHS Fe^{II} declined, whereas the concentration of vacuolar NHHS Fe^{III} increased to a limiting cellular concentration of ~ 300 μM. On the other hand, isolated mitochondria from cells grown in Fe-sufficient conditions contained more NHHS Fe^{II} ions and significant amounts of Fe^{III} nanoparticles. The lower NHHS Fe^{II} pool in Fe-deficient mitochondria was attributed to a decreased rate of import of Fe from the cytosol into the mitochondria due to Fe deficiency. The transition of non-mitochondrial NHHS Fe^{II} into the mitochondria (or vacuoles) upon Fe increase in the medium might be a result of the switch from high- to low-affinity Fe regulatory mechanisms or the upregulation of CCC1 (a vacuolar Fe import protein).

Future Studies

A topic that has remained of central interest to the field of iron metabolism for more than three decades is elucidation of the nature of the labile iron pool (LIP) present in cells and organelles. The LIP is hypothesized to be low-molecular-weight (LMW), 'loosely' coordinated by various organic ligands [197], and believed to play a role in Fe sensing and trafficking by the cells. Over the past five years, our lab has developed the capability to separate low-molecular-weight metal complexes found in cells [238]. This is achieved by exploiting anaerobic liquid chromatography, interfaced with an on-line ICP-MS. The system has been successfully tested on mouse brain homogenates. We may now use this set-up to characterize, and potentially identify, the ligands associated with the LMW Fe-containing species (which may form part of the LIP) present in Jurkat cells and isolated mitochondria. This can potentially provide great insight in understanding how these LMW species are sensed and trafficked within the cell.

Disruptions in iron homeostasis are linked to a variety of human diseases, most of which are a result of mutations and deficiencies in proteins involved in iron metabolism and trafficking. For example, depletion of the frataxin protein leads to Friedreich's ataxia, and depletion of ABCB7 leads to X-linked Sideroblastic anemia, both leading to mitochondrial iron overload, and mitochondrial dysfunction. Frataxin is involved in mitochondrial Fe/S biogenesis, and one of its hypothesized functions is that of an iron chaperone that delivers Fe into the Fe/S biogenesis machinery. ABCB7 is a mitochondrial membrane transporter that is hypothesized to export an unidentified

species, X, from the mitochondria into the cytosol, where X may be sensed by cytosolic proteins that are involved in cellular iron homeostasis. It would be of great interest to examine the LMW Fe profiles of cells depleted of frataxin or ABCB7, using our LC-ICP-MS set-up, and compare them to the profiles of normal Jurkat cells. Differences in the LMW Fe profiles upon depletion of these proteins of interest may point to the Fe-species that are involved in the processes controlling iron homeostasis inside the cell. These studies may, for example, provide insight into the nature of the species 'X', which is presumably exported by ABCB7.

One major challenge of studying the effects of disrupting iron homeostasis is teasing apart primary effects from secondary effects of depleting any protein involved in iron homeostasis, thus making it difficult to elucidate protein function. This is because disruption of iron metabolism most often results in similar ultimate phenotypes, namely, ferric nanoparticle accumulation, increase in oxidative stress, damage to Fe/S clusters and hemes, and mitochondrial dysfunction. Our ability to perform tetracycline-inducible knockdown of proteins in Jurkat cells implies that we can knock down proteins to various extents by varying the concentration of tetracycline added to the medium. The effect of 'dialing' down the levels of proteins such as frataxin and ABCB7 on the iron distribution of cells and isolated mitochondria can be studied using our biophysical and bioanalytical methods, as well as our LC-ICP-MS separation set-up. The primary effects of protein depletion may be potentially distinguished from secondary effects by the chronology of how oxidative stress, Fe distribution and Fe concentration of cells are affected.

Another avenue that may be worthwhile pursuing is the study of other organelles that are crucial for iron metabolism. After the mitochondrion, which is considered the 'hub' of iron metabolism, the organelle that comes to mind is the lysosome. The iron distribution of the vacuole, which is the yeast equivalent of the lysosome, has been studied in detail by our lab [120]. Vacuoles and lysosomes are similar in that they are both involved in degradation and recycling of macromolecules. However, vacuoles also have the added function of storing excess cellular iron in yeast, whereas that function is performed by ferritin (a 24-mer protein) in mammalian cells. On the other hand, autophagic events, namely the degradation of ferritin and mitochondria, may lead to an iron-rich environment in lysosomes, which increases their sensitivity to oxidative stress [239], leads to lysosomal instability, and impairs further autophagy. During the past decade, iron was found to be the major cause of lysosomal instability in the presence of hydrogen peroxide, leading to lysosomal rupture and apoptosis/necrosis, while hydrogen peroxide alone was harmless. Lipofuscin (the poorly characterized 'ageing pigment') and hemosiderin (the presumed breakdown product of ferritin) are two iron-rich, non-degradable materials most commonly found to accumulate in lysosomes. These lysosomal Fe-rich species are correlated with increased sensitivity of lysosomes to oxidative stress, and postmitotic ageing of cells [38, 239]. It would be of interest to examine and compare the iron content and speciation of lysosomes in 'young' vs. 'old' cells to elucidate the type of iron that might have a role in cellular ageing processes. It may also be of interest to see how the addition of an anti-oxidant (preferably one that does not

participate in redox chemistry with Fe) might affect the iron speciation of lysosomes and their sensitivity to oxidative stress.

Jurkat cells are easily scaled up in bioreactors by virtue of being a suspension cell line. However, other cell types that are more directly involved in systemic iron homeostasis, such as liver cells, macrophages, and enterocytes. These cell lines, although ordinarily grown as adherent cultures, may be adapted to grow in suspension, scaled up, and studied by our Mössbauer-centered biophysical techniques. Iron may be metabolized differently by these cells, and hence lead to varied iron distribution and speciation in these cells. Diseased states may also be studied by genetically modifying these cells. For example, hereditary hemochromatosis is one of the most common iron overload diseases, and involves a mutation in the HFE gene, which is expressed primarily in liver cells. The HFE gene product is believed to modulate (decrease) the affinity of the transferrin receptor for Fe in liver cells, and a dysfunctional HFE protein potentially leads to increased Fe binding to the transferrin receptor and increased Fe uptake, resulting in severe liver iron overload [240]. It would be of interest to study the effect of HFE depletion on the iron distribution of liver cells (whether we would observe more ferritin-bound Fe or more ferric nanoparticles).

The field of iron metabolism has witnessed tremendous breakthroughs in the past decade. However, numerous challenges remain in identifying the basic species involved in iron trafficking and sensing in the cell, and our understanding of the iron speciation and distribution in mammalian cells is still quite preliminary. Our biophysical methods,

teamed with our LC-ICP-MS separation methods, promise to be quite powerful in probing some of those challenges.

REFERENCES

1. Pantopoulos, K., Porwal, S. K., Tartakoff, A., and Devireddy, L. (2012) Mechanisms of Mammalian Iron Homeostasis, *Biochemistry 51*, 5705-5724.
2. Fanelli, A. R., Antonini, E., and Caputo, A. (1964) Hemoglobin and Myoglobin, *Adv Prot Chem 19*, 73-222.
3. Ingraham, L. L., and Meyer, D. L. (1985) Catalases and Peroxidases, In *Biochemistry of Dioxygen* 1st. ed., pp. 91-105, Plenum Press, NY.
4. Yonetani, T. (1970) Cytochrome *c* Peroxidase, *Adv Enzymol RAMB 33*, 309-335.
5. Carroll, J., Fearnley, I. M., Skehel, J. M., Shannon, R. J., Hirst, J., and Walker, J. E. (2006) Bovine Complex I is a Complex of 45 Different Subunits, *J. Biol. Chem. 281*, 32724-32727.
6. Cecchini, G. (2003) Function and Structure of Complex II of the Respiratory Chain, *Ann. Rev. 72*, 77-109.
7. Crofts, A. R. (2004) The Cytochrome *bc1* Complex: Function in the Context of Structure, *Annu. Rev. Physiol. 66*, 689-733.
8. Lanne, B., and Väangård, T. (1978) Redox Titrations of Cytochrome *c* Oxidase: An Analysis of a Multi-Electron System, *Biochim Biophys Acta 501*, 449-457.
9. Hall, R. E., Henriksson, K. G., Lewis, S. F., Haller, R. G., and Kennaway, N. G. (1993) Mitochondrial Myopathy with Succinate Dehydrogenase and Aconitase Deficiency-Abnormalities of Several Iron-Sulfur Proteins, *J. Clin. Invest. 92*, 2660-2666.

10. Atkin, C. L., Thelander, L., Reichard, P., and Lang, G. (1973) Iron and Free Radical in Ribonucleotide Reductase Exchange of Iron and Mössbauer Spectroscopy of the Protein B2 Subunit of the *Escherichia coli* Enzyme, *J. Biol. Chem. 248*, 7464-7472.

11. Theil, E. C. (1987) Ferritin: Structure, Gene Regulation, and Cellular Function in Animals, Plants and Microorganisms, *Ann. Rev. Biochem. 56*, 289-315.

12. Lloyd, R. V., Hanna, P. M., and Mason, R. P. (1997) The Origin of the Hydroxyl Radical Oxygen in the Fenton Reaction, *Free Radic. Biol. Med. 22*, 885-888.

13. Winterbourn, C. C. (1995) Toxicity of Iron and Hydrogen Peroxide: The Fenton Reaction, *Toxicol. Lett. 82*, 969-974.

14. Sun, H., Li, H., and Sadler, P. J. (1999) Transferrin as a Metal Ion Mediator, *Chem. Rev. 99*, 2817-2842.

15. Evans, P., Cindrova-Davies, T., Muttukrishna, S., Burton, G. J., Porter, J., and Jauniaux, E. (2011) Hepcidin and Iron Species Distribution Inside the First-Trimester Human Gestational Sac, *Mol. Human Reprod. 17*, 227-232.

16. Laurell, C.-B. (1952) Plasma Iron and the Transport of Iron in the Organism, *Pharmacol. Rev. 4*, 371-395.

17. Breuer, W., Hershko, C., and Cabantchik, Z. I. (2000) The Importance of Non-Transferrin Bound Iron in Disorders of Iron Metabolism, *Transfus Sci 23*, 185-192.

18. Robb, A. D., and Wessling-Resnick, M. (2004) Transferrin Receptor 2 Mediates a Biphasic Pattern of Transferrin Uptake Associated with Ligand Delivery to Multivesicular Bodies, *Am. J. Physiol. Cell. Physiol. 287*, 1769-1775.

19. Aisen, P. (2004) Transferrin Receptor 1, *Int. J. Biochem. 36*, 2137-2143.

20. Fleming, R. E., Migas, M. C., Holden, C. C., Waheed, A., Britton, R. S., Tomatsu, S., Bacon, B. R., and Sly, W. S. (2000) Transferrin Receptor 2: Continued Expression in Mouse Liver in The Face of Iron Overload and in Hereditary Hemochromatosis, *Proc. Natl. Acad. Sci. 97*, 2214-2219.

21. Dautry-Varsat, A., Ciechanover, A., and Lodish, H. F. (1983) pH and the Recycling of Transferrin During Receptor-Mediated Endocytosis, *Proc. Natl. Acad. Sci. 80*, 2258-2262.

22. Lambe, T., Simpson, R. J., Dawson, S., Bouriez-Jones, T., Crockford, T. L., Lepherd, M., Latunde-Dada, G. O., Robinson, H., Raja, K. B., and Campagna, D. R. (2009) Identification of a Steap3 Endosomal Targeting Motif Essential for Normal Iron Metabolism, *Blood 113*, 1805-1808.

23. Aisen, P. (1992) Entry of Iron Into Cells: A New Role for the Transferrin Receptor in Modulating Iron Release From Transferrin, *Ann. Neurol. 32*, S62-S68.

24. Huebers, H., Josephson, B., Huebers, E., Csiba, E., and Finch, C. (1981) Uptake and Release of Iron from Human Transferrin, *Proc. Natl. Acad. Sci. 78*, 2572-2576.

25. Sturrock, A., Alexander, J., Lamb, J., Craven, C. M., and Kaplan, J. (1990) Characterization of a Transferrin-independent Uptake System for Iron in HeLa cells, *J. Biol. Chem. 265*, 3139-3145.

26. Loreal, O., and Hider, R. C. (2000) Determination of Non-Transferrin-Bound Iron in Genetic Hemochromatosis Using a New HPLC-Based Method, *J Hepatol 32*, 727-733.

27. Breuer, W., Ghoti, H., Shattat, A., Goldfarb, A., Koren, A., Levin, C., Rachmilewitz, E., and Cabantchik, Z. I. (2012) Non-Transferrin Bound Iron in Thalassemia: Differential Detection of Redox Active Forms in Children and Older Patients, *Am J Hematol 87*, 55-61.

28. Oudit, G. Y., and Backx, P. H. (2003) L-Type Ca2+ Channels Provide a Major Pathway for Iron Entry into Cardiomyocytes in Iron-Overload Cardiomyopathy, *Nat. Med. 9*, 1187-1194.

29. Tabuchi, M., and Kishi, F. (2000) Human NRAMP2/DMT1, Which Mediates Iron Transport across Endosomal Membranes, Is Localized to Late Endosomes and Lysosomes in HEp-2 Cells, *J. Biol. Chem. 275*, 22220-22228.

30. Liuzzi, J. P., and Cousins, R. J. (2006) Zip14 (Slc39A14) Mediates Non-Transferrin-Bound Iron Uptake into Cells, *Proc. Natl. Acad. Sci. 103*, 13612-13617.

31. Devireddy, L. R., Gazin, C., Zhu, X., and Green, M. R. (2005) A Cell-Surface Receptor for Lipocalin 24p3 Selectively Mediates Apoptosis and Iron Uptake, *Cell 123*, 1293-1305.

32. Gelvan, D., Fibach, E., Meyron-Holtz, E. G., and Konijn, A. (1996) Ferritin Uptake by Human Erythroid Precursors is a Regulated Iron Uptake Pathway, *Blood 88*, 3200-3207.

33. Smith, A., and Morgan, W. (1984) Hemopexin-Mediated Heme Uptake by Liver-Characterization of the Interaction of Heme-Hemopexin with Isolated Rabbit Liver Plasma Membranes, *J. Biol. Chem. 259*, 12049-12053.

34. McKie, A. T., Barrow, D., Latunde-Dada, G. O., Rolfs, A., Sager, G., Mudaly, E., Mudaly, M., Richardson, C., Barlow, D., and Bomford, A. (2001) An Iron-Regulated Ferric Reductase Associated with the Absorption of Dietary Iron, *Science 291*, 1755-1759.

35. Lane, D. J. R., and Lawen, A. (2008) Non-Transferrin Iron Reduction and Uptake are Regulated by Transmembrane Ascorbate Cycling in K562 Cells, *J. Biol. Chem. 283*, 12701-12708.

36. Sohn, Y.-S., Ghoti, H., Breuer, W., Rachmilewitz, E. A., Attar, S., Weiss, G., and Cabantchik, Z. I. (2011) The Role of Endocytic Pathways in Cellular Uptake of Plasma Non-Transferrin Iron, *Haematologica 97*, 670-678.

37. Kakhlon, O., and Cabantchik, Z. I. (2002) The Labile Iron Pool: Characterization, Measurement, and Participation in Cellular Processes, *Free Radical Biol Med 33*, 1037-1046.

38. Kurz, T., Eaton, J., and Brunk, U. T. (2011) The Role of Lysosomes in Iron Metabolism and Recycling, *Int. J. Biochem., 43*, 1686-1697.

39. Esposito, B. P., Epsztejn, S., Breuer, W., and Cabantchik, Z. I. (2002) A Review of Fluorescence Methods for Assessing Labile Iron in Cells and Biological Fluids, *Anal. Biochem. 304*, 1-18.

40. Chitambar, C. R. (2005) Cellular Iron Metabolism: Mitochondria in the Spotlight, *Blood 105*, 1844-1845.

41. Shaw, G. C., Cope, J. J., Li, L., Corson, K., Hersey, C., Ackermann, G. E., Gwynn, B., Lambert, A. J., Wingert, R. A., Traver, D., Trede, N. S., Barut, B. A., Zhou, Y., Minet, E., Donovan, A., Brownlie, A., Balzan, R., Weiss, M. J., Peters, L. L., Kaplan, J., Zon, L. I., and Paw, B. (2006) Mitoferrin is Essential for Erythroid Iron Assimilation, *Nature Letters 440*, 96-100.

42. Paradkar, P. N., Zumbrennen, K. B., Paw, B. H., Ward, D. M., Kaplan, J. K. . (2009) Regulation of Mitochondrial Iron Import through Differential Turnover of Mitoferrin 1 and Mitoferrin 2, *Mol. Cell. Biol. 29*, 1007-1016.

43. Chen, W., Paradkar, P. N., Li, L., Pierce, E. L., Langer, N. B., Takahashi-Makise, N., Hyde, B. B., Shirihai, O. S., Ward, D. M., and Kaplan, J. (2009) Abcb10 Physically Interacts with Mitoferrin-1 (Slc25A37) to Enhance its Stability and Function in the Erythroid Mitochondria, *Proc. Natl. Acad. Sci. 106*, 16263-16268.

44. Devireddy, L. R., Hart, D. O., Goetz, D., and Green, M. R. (2010) A Mammalian Siderophore Synthesized by an Enzyme with a Bacterial Homologue Involved in Enterobactin Production, *Cell 141*, 1006-1017.

45. Sheftel, A. D., Zhang, A.-S., Brown, C., Shirihai, O. S., and Ponka, P. (2007) Direct Interorganellar Transfer of Iron from Endosome to Mitochondrion, *Blood 110*, 125-132.

46. Drysdale, J., Arosio, P., Ivernizzi, R., Cazzola, M., Volz, A., Corsi, B., Biasiotto, G., and Levi, S. (2002) Mitochondrial Ferritin: A New Player in Iron Metabolism, *Blood Cell Mol Dis, 29*, 376-383.

47. Rouault, T. A. (2012) Biogenesis of Iron-Sulfur Clusters in Mammalian Cells: New Insights and Relevance to Human Disease, *Dis. Models Mech. 5*, 155-164.

48. Biederbick, A., Stehling, O., Rösser, R., Niggemeyer, B., Nakai, Y., Elsässer, H.-P., and Lill, R. (2006) Role of Human Mitochondrial Nfs1 in Cytosolic Iron-Sulfur Protein Biogenesis and Iron Regulation, *Mol. Cell. Biol. 26*, 5675-5687.

49. Shi, R., Proteau, A., Villarroya, M., Moukadiri, I., Zhang, L., Trempe, J.-F., Matte, A., Armengod, M. E., and Cygler, M. (2010) Structural Basis for Fe–S Cluster Assembly and tRNA Thiolation Mediated by IscS Protein–Protein Interactions, *PLoS Biol. 8*, 1-18.

50. Lill, R. (2009) Function and Biogenesis of Iron–Sulphur Proteins, *Nature 460*, 831-838.

51. Agar, J. N., Krebs, C., Frazzon, J., Huynh, B. H., Dean, D. R., and Johnson, M. K. (2000) IscU as a Scaffold for Iron-Sulfur Cluster Biosynthesis: Sequential Assembly of [2Fe-2S] and [4Fe-4S] Clusters in IscU, *Biochemistry 39*, 7856-7862.

52. Yoon, T., and Cowan, J. (2003) Iron-Sulfur Cluster Biosynthesis. Characterization of Frataxin as an Iron Donor for Assembly of [2Fe-2S] Clusters in Isu-Type Proteins, *J. Am. Chem. Soc. 125*, 6078-6084.

53. Qi, W., and Cowan, J. (2011) Mechanism of Glutaredoxin—ISU [2Fe–2S] Cluster Exchange, *Chem. Commun. 47*, 4989-4991.

54. Tsai, C.-L., and Barondeau, D. P. (2010) Human Frataxin Is an Allosteric Switch That Activates the Fe-S Cluster Biosynthetic Complex, *Biochemistry 49*, 9132-9139.

55. Wiedemann, N., Urzica, E., Guiard, B., Müller, H., Lohaus, C., Meyer, H. E., Ryan, M. T., Meisinger, C., Mühlenhoff, U., and Lill, R. (2005) Essential Role of Isd11 in Mitochondrial Iron–Sulfur Cluster Synthesis on Isu Scaffold Proteins, *The EMBO Journal 25*, 184-195.

56. Lillig, C. H., Berndt, C., and Holmgren, A. (2008) Glutaredoxin Systems, *BBA-General Subjects, 1780*, 1304-1317.

57. Shi, Y., Ghosh, M., Kovtunovych, G., Crooks, D. R., and Rouault, T. A. (2012) Both Human Ferredoxins 1 and 2 and Ferredoxin Reductase are Important for Iron-Sulfur Cluster Biogenesis, *BBA-Mol Cell Res, 1823*, 484-492.

58. Uhrigshardt, H., Singh, A., Kovtunovych, G., Ghosh, M., and Rouault, T. A. (2010) Characterization of the Human Hsc20, an Unusual DnaJ Type III Protein, Involved in Iron–Sulfur Cluster Biogenesis, *Hum. Mol. Genet. 19*, 3816-3834.

59. Kampinga, H. H., and Craig, E. A. (2010) The Hsp70 Chaperone Machinery: J Proteins as Drivers of Functional Specificity, *Nat. Rev. Mol. Cell. Biol., 11*, 579-592.

60. Land, T., and Rouault, T. A. (1998) Targeting of a Human Iron–Sulfur Cluster Assembly Enzyme, NifS, to Different Subcellular Compartments Is Regulated through Alternative AUG Utilization, *Mol. Cell 2*, 807-815.

61. Ajioka, R. S., Phillips, J. D., and Kushner, J. P. (2006) Biosynthesis of Heme in Mammals, *BBA-Mol Cell Res 1763*, 723-736.

62. Zhang, J., and Ferreira, G. C. (2002) Transient State Kinetic Investigation of 5-Aminolevulinate Synthase Reaction Mechanism, *J. Biol. Chem. 277*, 44660-44669.

63. Kaya, A. H., Plewlnska, M., Wong, D. M., Desnick, R. J., and Wetmur, J. G. (1994) Human δ-aminolevulinate Dehydratase (ALAD) Gene: Structure and Alternative Splicing of the Erythroid and Housekeeping mRNAs, *Genomics 19*, 242-248.

64. Jordan, P. M., Thomas, S. D., and Warren, M. J. (1988) Purification, Crystallization and Properties of Porphobilinogen Deaminase from a Recombinant Strain of *Escherichia coli* K12, *Biochem. J. 254*, 427.

65. Frydman, R. B., and Feinstein, G. (1974) Studies on Porphobilinogen Deaminase and Uroporphyrinogen III Cosynthase from Human Erythrocytes, *BBA-Enzymol 350*, 358-373.

66. De Verneuil, H., Sassa, S., and Kappas, A. (1983) Purification and Properties of Uroporphyrinogen Decarboxylase from Human Erythrocytes. A Single Enzyme Catalyzing the Four Sequential Decarboxylations of Uroporphyrinogens I And III, *J. Biol. Chem. 258*, 2454-2460.

67. Sano, S., and Granick, S. (1961) Mitochondrial Coproporphyrinogen Oxidase and Protoporphyrin Formation, *J. Biol. Chem. 236*, 1173-1180.

68. Poulson, R., and Polglase, W. (1975) The Enzymic Conversion of Protoporphyrinogen IX To Protoporphyrin Ix. Protoporphyrinogen Oxidase Activity in Mitochondrial Extracts of *Saccharomyces cerevisiae*, *J. Biol. Chem. 250*, 1269-1274.

69. Porra, R., and Jones, O. (1963) Studies on Ferrochelatase. 2. An Investigation of the Role of Ferrochelatase in the Biosynthesis of Various Haem Prosthetic Groups, *Biochem. J. 87*, 186-192.

70. Donovan, A., Lima, C. A., Pinkus, J. L., Pinkus, G. S., Zon, L. I., Robine, S., and Andrews, N. C. (2005) The Iron Exporter Ferroportin/Slc40A1 is Essential for Iron Homeostasis, *Cell Metab 1*, 191-200.

71. Curtis, A. R., Fey, C., Morris, C. M., Bindoff, L. A., Ince, P. G., Chinnery, P. F., Coulthard, A., Jackson, M. J., Jackson, A. P., and McHale, D. P. (2001) Mutation in the Gene Encoding Ferritin Light Polypeptide Causes Dominant Adult-Onset Basal Ganglia Disease, *Nat. Genet. 28*, 350-354.

72. Arosio, P., and Levi, S. (2010) Cytosolic and Mitochondrial Ferritins in the Regulation of Cellular Iron Homeostasis and Oxidative Damage, *Biochim Biophys Acta 1800*, 783-792.

73. Bauminger, E. R., Harrison, P., Nowik, I., and Treffry, A. (1988) Composition and Dynamics of Iron in Iron-Poor Ferritin, *Hyperfine Interact 42*, 873-876.

74. Watt, R. K. (2013) A Unified Model for Ferritin Iron Loading by the Catalytic Center: Implications for Controlling "Free Iron" during Oxidative Stress, *ChemBioChem 14*, 415-419.

75. Shi, H., Bencze, K. Z., Stemmler, T. L., and Philpott, C. C. (2008) A Cytosolic Iron Chaperone that Delivers Iron to Ferritin, *Science 320*, 1207-1209.

76. Zhang, Y., Mikhael, M., Xu, D., Li, Y., Soe-Lin, S., Ning, B., Li, W., Nie, G., Zhao, Y., and Ponka, P. (2010) Lysosomal Proteolysis is the Primary Degradation Pathway for Cytosolic Ferritin and Cytosolic Ferritin Degradation is Necessary for Iron Exit, *Antioxid. Redox Signal. 13*, 999-1009.

77. Weir, M. P., Gibson, J. F., and Peters, T. J. (1984) Hemosiderin and Tissue Damage, *Cell Biochem. Funct. 2*, 186-194.

78. Casey, J. L., Hentze, M. W., Koeller, D. M., Caughman, S. W., Rouault, T. A., Klausner, R. D., and Harford, J. B. (1988) Iron-Responsive Elements: Regulatory RNA Sequences that Control mRNA Levels and Translation, *Science 240*, 924-928.

79. Anderson, C. P., Shen, M., Eisenstein, R. S., and Leibold, E. A. (2012) Mammalian Iron Metabolism and its Control by Iron Regulatory Proteins, *BBA-Mol Cell Res 1863*, 1468-83.

80. Schalinske, K. L., Anderson, S. A., Tuazon, P. T., Chen, O. S., Kennedy, M. C., and Eisenstein, R. S. (1997) The Iron-Sulfur Cluster of Iron Regulatory Protein 1 Modulates the Accessibility of RNA Binding and Phosphorylation Sites, *Biochemistry 36*, 3950-3958.

81. Varghese, S., Tang, Y., and Imlay, J. A. (2003) Contrasting Sensitivities of *Escherichia coli* Aconitases A And B to Oxidation and Iron Depletion, *J. Bacteriol. 185*, 221-230.

82. Drapier, J.-C., and Hibbs Jr, J. B. (1986) Murine Cytotoxic Activated Macrophages Inhibit Aconitase in Tumor Cells. Inhibition Involves the Iron-Sulfur Prosthetic Group and is Reversible, *J. Clin. Invest. 78*, 790-797.

83. Eisenstein, R. S., Tuazon, P., Schalinske, K., Anderson, S., and Traugh, J. (1993) Iron-Responsive Element-Binding Protein. Phosphorylation by Protein Kinase C, *J. Biol. Chem. 268*, 27363-27370.

84. Vashisht, A. A., Zumbrennen, K. B., Huang, X., Powers, D. N., Durazo, A., Sun, D., Bhaskaran, N., Persson, A., Uhlen, M., and Sangfelt, O. (2009) Control of Iron Homeostasis by an Iron-Regulated Ubiquitin Ligase, *Science Signal. 326*, 718-721.

85. Salahudeen, A. A., Thompson, J. W., Ruiz, J. C., Ma, H.-W., Kinch, L. N., Li, Q., Grishin, N. V., and Bruick, R. K. (2009) An E3 Ligase Possessing an Iron-

Responsive Hemerythrin Domain is a Regulator of Iron Homeostasis, *Science Signal. 326*, 722-726.

86. Chollangi, S., Thompson, J. W., Ruiz, J. C., Gardner, K. H., and Bruick, R. K. (2012) Hemerythrin-like Domain within F-box and Leucine-Rich Repeat Protein 5 (FBXL5) Communicates Cellular Iron and Oxygen Availability by Distinct Mechanisms, *J. Biol. Chem. 287*, 23710-23717.

87. Muckenthaler, M. U., Galy, B., and Hentze, M. W. (2008) Systemic Iron Homeostasis and the Iron-Responsive Element/Iron-Regulatory Protein (IRE/IRP) Regulatory Network, *Annu. Rev. Nutr. 28*, 197-213.

88. Kim, H.-Y., LaVaute, T., Iwai, K., Klausner, R. D., and Rouault, T. A. (1996) Identification of a Conserved and Functional Iron-Responsive Element in the 5′-Untranslated Region of Mammalian Mitochondrial Aconitase, *J. Biol. Chem. 271*, 24226-24230.

89. Bayeva, M., Khechaduri, A., Puig, S., Chang, H.-C., Patial, S., Blackshear, P. J., and Ardehali, H. (2012) mTOR Regulates Cellular Iron Homeostasis through Tristetraprolin, *Cell Metab., 16,* 645-647.

90. Gordeuk, V. R., Caleffi, A., Corradini, E., Ferrara, F., Jones, R. A., Castro, O., Onyekwere, O., Kittles, R., Pignatti, E., and Montosi, G. (2003) Iron Overload in Africans and African-Americans and a Common Mutation in the Scl40A1 (Ferroportin 1) Gene, *Blood Cells Mol Dis, 31*, 299-304.

91. Canonne-Hergaux, F., Donovan, A., Delaby, C., Wang, H.-j., and Gros, P. (2006) Comparative Studies of Duodenal and Macrophage Ferroportin Proteins, *Am J Physiol Gastrointest Liver Physiol 290*, G156-G163.

92. Pignatti, E., Mascheroni, L., Sabelli, M., Barelli, S., Biffo, S., and Pietrangelo, A. (2006) Ferroportin is a Monomer in Vivo in Mice, *Blood Cells Mol Dis, 36*, 26-32.

93. Rice, A. E., Mendez, M. J., Hokanson, C. A., Rees, D. C., and Björkman, P. J. (2009) Investigation of the Biophysical and Cell Biological Properties of Ferroportin, a Multipass Integral Membrane Protein Iron Exporter, *J. Mol. Biol. 386*, 717-732.

94. De Domenico, I., Ward, D. M., Musci, G., and Kaplan, J. (2007) Evidence for the Multimeric Structure of Ferroportin, *Blood 109*, 2205-2209.

95. Han, O., and Kim, E. Y. (2007) Colocalization of Ferroportin-1 with Hephaestin on the Basolateral Membrane of Human Intestinal Absorptive Cells, *J. Cell. Biochem. 101*, 1000-1010.

96. Milman, N. (2011) Anemia—Still a Major Health Problem in Many Parts of the World!, *Ann Hematol 90*, 369-377.

97. Killip, S., Bennett, J. M., and Chambers, M. D. (2000) Iron Deficiency Anemia, *Am Fam Physician 75*, 671-678.

98. Weiss, G., and Goodnough, L. T. (2005) Anemia of Chronic Disease, *New Engl. J. Med. 352*, 1011-1023.

99. Finberg, K. E. (2009) Iron-Refractory Iron Deficiency Anemia, *Seminars in hematology 46,* 378-386.

100. Livrea, M., Tesoriere, L., Pintaudi, A., Calabrese, A., Maggio, A., Freisleben, H., D'arpa, D., D'anna, R., and Bongiorno, A. (1996) Oxidative Stress and Antioxidant Status in β-Thalassemia Major: Iron Overload and Depletion of Lipid-Soluble Antioxidants, *Blood 88*, 3608-3614.

101. Cooksey, R. C., Jouihan, H. A., Ajioka, R. S., Hazel, M. W., Jones, D. L., Kushner, J. P., and McClain, D. A. (2004) Oxidative Stress, β-cell Apoptosis, and Decreased Insulin Secretory Capacity in Mouse Models of Hemochromatosis, *Endocrinology 145*, 5305-5312.

102. Alexander, J., and Kowdley, K. V. (2005) Hereditary Hemochromatosis: Genetics, Pathogenesis, and Clinical Management, *Ann Hepatol 4*, 240-247.

103. Galanello, R., and Origa, R. (2010) Review: β-Thalassemia, *Orphanet J Rare Dis 5*, 1-15.

104. Campuzano, V., Montermini, L., Moltò, M. D., Pianese, L., Cossée, M., Cavalcanti, F., Monros, E., Rodius, F., Duclos, F., and Monticelli, A. (1996) Friedreich's Ataxia: Autosomal Recessive Disease Caused by an Intronic GAA Triplet Repeat Expansion, *Science 271*, 1423-1427.

105. Pondarre, C., Campagna, D. R., Antiochos, B., Sikorski, L., Mulhern, H., and Fleming, M. D. (2007) Abcb7, the Gene Responsible for X-Linked Sideroblastic Anemia with Ataxia, is Essential for Hematopoiesis, *Blood 109*, 3567-3569.

106. Tangerås, A., Flatmark, T., Bäckström, D., and Ehrenberg, A. (1980) Mitochondrial Iron not Bound in Heme and Iron-Sulfur Centers: Estimation, Compartmentation and Redox State, *Biochim Biophys Acta 589*, 162-175.

107. Tangerås, A. (1983) Iron Content and Degree of Lipid Peroxidation in Liver Mitochondria Isolated from Iron-Loaded Rats, *Biochim Biophys Acta 757*, 59-68.

108. Tangerås, A. (1985) Mitochondria Iron not Bound in Heme and Iron-Sulfur Centers and its Availability for Heme Synthesis *in vitro*, *Biochim Biophys Acta 843*, 199-207.

109. Petrat, F., Groot, H. D., Sustmann, R., and Rauen, U. (2002) The Chelatable Iron Pool in Living Cells: A Methodically Defined Quantity, *Biol. Chem. 383*, 489-502.

110. Fakih, S., Podinovskaia, M., Kong, X., Shaible, U. E., Collins, H. L., and Hider, R. C. (2008) Monitoring Intracellular Labile Iron Pools: A Novel Fluorescent Iron (III) Sensor as a Potential Non-Invasive Diagnosis Tool, *J. Pharm. Sci. 98*, 2212-2226.

111. Luo, W., Quinn, P. J., Hider, R. C., and Liu, Z. D. (2004) Design, Synthesis and Properties of Novel Iron(III)-Specific Fluorescent Probes, *J. Pharm. Pharmacol. 56*, 529-536.

112. Kruszewski, M. (2003) Labile Iron Pool: The Main Determinant of Cellular Response to Oxidative Stress, *Mutat. Res. 531*, 81-92.

113. Becker, J. S., Matusch, A., Palm, C., Salber, D., Morton, K. A., and Becker, J. S. (2010) Bioimaging of Metals in Brain Tissue by Laser Ablation Inductively

Coupled Plasma Mass Spectrometry (LA-ICP-MS) and Metallomics, *Metallomics 2*, 104-111.

114. Matusch, A., Depboylu, C., Palm, C., Wu, B., Höglinger, G. U., Schäfer, M. K.-H., and Becker, J. S. (2010) Cerebral Bioimaging of Cu, Fe, Zn, and Mn in the MPTP Mouse Model of Parkinson's Disease Using Laser Ablation Inductively Coupled Plasma Mass Spectrometry (LA-ICP-MS), *J. Am. Soc. Mass Spectrom. 21*, 161-171.

115. Greenwood, N. N., and Greatrex, R. (1971) Mössbauer Spectroscopy, In *Spectroscopic Properties of Inorganic and Organometallic Compounds 4,* pp. 478-575, Royal Society of Chemistry, London.

116. Hudder, B. N., Morales, J. G., Stubna, A., Münck, E., Hendrich, M. P., and Lindahl, P. A. (2007) Electron Paramagnetic Resonance and Mössbauer Spectroscopy of Intact Mitochondria from Respiring *Saccharomyces cerevisiae*, *J Biol Inorg Chem 12*, 1029-1053.

117. Miao, R., Martinho, M., Morales, J. G., Kim, H., Ellis, A., Lill, R., Hendrich, M. P., Münck, E., and Lindahl, P. A. (2008) EPR and Mössbauer Spectroscopy of Intact Mitochondria Isolated from Yah1p-Depleted *Saccharomyces cerevisiae*, *Biochemistry 47*, 9888-9899.

118. Holmes-Hampton, G., Miao, R., Morales, J. G., Guo, Y., Münck, E., and Lindahl, P. A. (2010) A Nonheme High-Spin Ferrous Pool in Mitochondria Isolated from Fermenting *Saccharomyces cerevisiae*, *Biochemistry 49*, 4227-4234.

119. Morales, J. G., Holmes-Hampton, G., Miao, R., Guo, Y., Münck, E., and Lindahl, P. A. (2010) Biophysical Characterization of Iron in Mitochondria Isolated from Respiring and Fermenting Yeast, *Biochemistry 49*, 5436-5444.

120. Cockrell, A. L., Holmes-Hampton, G. P., McCormick, S. P., Chakrabarti, M., and Lindahl, P. A. (2011) Mössbauer and EPR Study of Iron in Vacuoles from Fermenting *Saccharomyces cerevisiae*, *Biochemistry 50*, 10275-10283.

121. Goodman, B., and Hall, P. (1994) Electron Paramagnetic Resonance Spectroscopy, In *Clay Mineralogy: spectroscopic and chemical determinative methods*, pp. 173-225, Springer, Netherlands.

122. Williams, M., Thomas, B., Farrar, J., and Pollock, C. (1993) Visualizing the Distribution of Elements within Barley Leaves by Energy Dispersive X-Ray Image Maps (EDX Maps), *New Phytol. 125*, 367-372.

123. Williams Jr, J. (1964) A Method for the Simultaneous Quantitative Estimation of Cytochromes *a, b, c1*, and *c* in Mitochondria, *Arch Biochem Biophys 107*, 537-543.

124. Jhurry, N. D., Chakrabarti, M., McCormick, S. P., Holmes-Hampton, G., and Lindahl, P. A. (2012) Biophysical Investigation of the Ironome of Human Jurkat Cells and Mitochondria, *Biochemistry 51*, 5276-5284.

125. Anderson, G. J., and Vulpe, C. D. (2009) Mammalian Iron Transport, *Cell. Mol. Life Sci. 66*, 3241-3261.

126. Ned, R. M., Swat, W., and Andrews, N. C. (2003) Transferrin Receptor 1 is Differentially Required in Lymphocyte Development, *Blood 102*, 3711-3718.

127. Hider, R. C. (2002) Nature of Nontransferrin-Bound Iron, *Eur. J. Clin. Inv. 32*, 50-54.

128. Jordan, I., and Kaplan, J. (1994) The Mammalian Transferrin-Independent Iron Transport System May Involve a Surface Ferrireductase Activity, *Biochem. J. 302*, 875-879.

129. Richmond, V. S., Worwood, M., and Jacobs, A. (1972) The Iron Content of Intestinal Epithelial Cells and Its Subcellular Distribution: Studies on Normal, Iron-Overloaded and Iron-Deficient Rats, *Br. J. Haematol. 23*, 605-614.

130. Pandolfo, M., and Pastore, A. (2009) The pathogenesis of Friedreich ataxia and the structure and function of frataxin, *J Neurol 256*, 9-17.

131. Ye, H., and Rouault, T. A. (2010) Human Iron-Sulfur Cluster Assembly, Cellular Iron Homeostasis, and Disease, *Biochemistry 49*, 4945-4956.

132. Tsukihara, T., H., A., Yamashita, E., Tomizaki, T., Yamaguchi, H., Shinzawa-Itoh, K., Nakashima, R., Yaono, R., and Yoshikawa, S. (1996) The Whole Structure of the 13-Subunit Oxidized Cytochrome *c* Oxidase at 2.8 Å., *Science 272*, 1136-1144.

133. Dubiel, S. M., Zablotna-Rypien, B., Mackey, J. B., and Williams, J. M. (1999) Magnetic Properties of Human Liver and Brain Ferritin, *Eur Biophys J 28*, 263-267.

134. Papaefthymiou, G. C. (2010) The Mössbauer and Magnetic Properties of Ferritin Cores, *Biochim Biophys Acta 1800*, 886-897.

135. Baader, S. L., Bill, E., Trautwein, A. X., Bruchelt, G., and Matzanke, B. F. (1996) Mobilization of Iron from Cellular Ferritin by Ascorbic Acid in Neuroblastoma SK-N-SH Cells: An EPR Study, *FEBS Lett. 381*, 131-134.

136. Glickstein, H., B., E. R., Shvartsman, M., and Cabantchik, Z. I. (2005) Intracellular Labile Iron Pools as Direct Targets of Iron Chelators: A Fluorescence Study of Chelator Action in Living Cells, *Blood 106*, 3242-3250.

137. Wiley, S. E., Rardin, M. J., and Dixon, J. E. (2009) Localization and Function of The 2Fe-2S Outer Mitochondrial Membrane Protein MITONEET, *Methods Enzymol. 456*, 233-246.

138. Ellis, E. A. Poststaining Grids for Transmission Electron Microscopy, *Methods Mol Biol 369*, 97-106.

139. Miao, R., Kim, H., Koppolu, M. K., Ellis, A., Scott, R. A., and Lindahl, P. A. (2009) Biophysical Characterization of the Iron in Mitochondria from Atm1p-Depleted *Saccharomyces cerevisiae*, *Biochemistry 48*, 9556-9568.

140. Beinert, H. (1978) EPR Spectroscopy of Components of Mitochondrial Electron-Transfer System, *Methods Enzymol. LIV*, 133-150.

141. Hunt, C., Pankhurst, Q. A., and Dickson, D. P. E. (1994) Applied Field Mössbauer Studies of the Iron Storage Proteins Ferritin and Haemosiderin *Hyperfine Interact 91*, 821-826.

142. Kim, Y.-M., Chung, H.-T., Simmons, R. L., and Billiar, T. R. (2000) Cellular Non-Heme Iron Content Is a Determinant of Nitric Oxide-mediated Apoptosis, Necrosis, and Caspase Inhibition, *J. Biol. Chem. 275*, 10954-10961.

143. Chapman, E. H., Kurec, A. S., and Davey, F. R. (1981) Cell Volumes of Normal and Malignant Mononuclear Cells, *J Clin Pathol 34*, 1083-1090.

144. Ekmekcioglu, C., Prohaska, C., Pomazal, K., Steffan, I., Schernthaner, G., and Marktl, W. (2001) Concentrations of Seven Trace Elements in Different Hematological Matrices in Patients with Type 2 Diabetes as Compared to Healthy Controls, *Biol. Trace Elem. Res. 79*, 205-219.

145. Carpentieri, U., Myers, J., Thorpe, L., Daeschner III, C. W., and Haggard, M. E. (1986) Copper, Zinc, and Iron in Normal and Leukemic Lymphocytes from Children, *Cancer Res. 46*, 981-984.

146. Weibel, E. R., Stäubli, W., Gnägi, H. R., and Hess, F. A. (1969) Correlated Morphometric and Biochemical Studies on the Liver Cell, *J Cell Biol 42*, 68-91.

147. Leary, S. C., Winge, D. R., and Cobine, P. A. (2009) "Pulling the Plug" on Cellular Copper: The Role of Mitochondria in Copper Export, *Biochim Biophys Acta 1793*, 146-153.

148. Jancura, D., Berka, V., Antalik, M., Bagelova, J., Gennis, R. B., Palmer, G., and Fabian, M. (2006) Spectral and Kinetic Equivalence of Oxidized Cytochrome *c* Oxidase as Isolated and "Activated" by Reoxidation, *J. Biol. Chem. 281*, 30319-30325.

149. Kaila, V. R. I., Verkhovsky, M. I., and Wikström, M. (2010) Proton-Coupled Electron Transfer in Cytochrome Oxidase, *Chem. Rev. 110*, 7062-7081.

150. Lenaz, G., and Genova, M. L. (2010) Structure and Organization of Mitochondrial Respiratory Complexes: A New Understanding of an Old Subject, *Antioxid. Redox Signal. 12*, 961-1008.

151. Epsztejn, S., Kakhlon, O., Glickstein, H., Breuer, W., and Cabantchik, Z. I. (1997) Fluorescence Analysis of the Labile Iron Pool of Mammalian Cells, *Anal. Biochem. 248*, 31-40.

152. Petrat, F., Rauen, U., and Groot, H. D. (1999) Determination of the Chelatable Iron Pool of Isolated Rat Hepatocytes by Digital Fluorescence Microscopy Using the Fluorescent Probe, Phen Green SK, *Hepatology 29*, 1171-1179.

153. Petrat, F., Groot, H. D., and Rauen, U. (2002) Selective Determination of Mitochondrial Chelatable Iron in Viable Cells with a New Fluorescent Sensor, *Biochem. J. 362*, 137-147.

154. Breuer, W., Epsztejn, S., and Cabantchik, Z. I. (1995) Iron Acquired from Transferrin by K562 Cells is Delivered into a Cytoplasmic Pool of Chelatable Iron (II), *J. Biol. Chem. 270*, 24209-24215.

155. Gackowski, D., Kruszewski, M., Banaszkiewicz, Z., Jawien, A., and Olinski, R. (2002) Lymphocyte Labile Iron Pool, Plasma Iron, Transferrin Saturation and Ferritin Levels in Colon Cancer Patients, *Acta Biochim. Pol. 49*, 269-272.

156. Petrat, F., Groot, H. D., and Rauen, U. (2001) Subcellular Distribution of Chelatable Iron: A Laser Scanning Microscopic Study in Isolated Hepatocytes and Liver Endothelial Cells, *Biochem. J. 356*, 61-69.

157. Bauminger, E. R., Cohen, S. G., Dickson, D. P. E., Levy, A., Ofer, S., and Yariv, J. (1979) Mössbauer Spectroscopy of *Escherichia coli* and its Iron-Storage Protein *Biochim Biophys Acta 623*, 237-242.

158. St. Pierre, T. G., Bell, S. H., Dickson, D. P. E., Mann, S., Webb, J., Moore, G. R., and Williams, R. J. P. (1985) Mössbauer Spectroscopic Studies of the Cores of Human, Limpet and Bacterial Ferritins, *Biochim Biophys Acta 870*, 127-134.

159. Seguin, A., Sutak, R., Bulteau, A.-L., Garcia-Serres, R., Oddou, J.-L., Lefevre, S., Santos, R., Dancis, A., Camadro, J.-M., Latour, J.-M., and Lesuisse, E. (2010) Evidence that Yeast Frataxin is not an Iron Storage Protein *in vivo*, *Biochim Biophys Acta 1802*, 531-538.

160. Brissot, P., Ropert, M., Le Lan, C., and Loreal, O. (2012) Non-Transferrin Bound Iron: A Key Role in Iron Overload and Iron Toxicity, *Biochim Biophys Acta 1820*, 403-410.

161. Evans, R. W., Rafique, R., Zarea, A., Rapisarda, C., Cammack, R., Evans, P. J., Porter, J. B., and Hider, R. C. (2008) Nature of Non-Transferrin-Bound Iron: Studies on Iron Citrate Complexes and Thalassemic Sera, *J Biol Inorg Chem 13*, 57-74.

162. Picard, V., Govoni, G., Jabado, N., and Gros, P. (2000) Nramp2 (DCT1/DMT1) Expressed at the Plasma Membrane Transports Iron and Other Divalent Cations into a Calcein-accessible Cytoplasmic Pool, *J. Biol. Chem. 275*, 35738-35745.

163. Grootveld, M., Bells, J. D., Halliwell, B., Aruoma, O. I., Bomford, A., and Sadler, P. J. (1989) Non-Transferrin-Bound Iron in Plasma or Serum from Patients with Idiopathic Hemochromatosis, *J. Biol. Chem. 264*, 4417-4422.

164. Bernstein, S. E. (1987) Hereditary Hypotransferrinemia with Hemosiderosis, A Murine Disorder Resembling Human Atransferrinemia, *J Lab Clin Med 110*, 690-705.

165. Valk, B. D., and Marx, J. J. M. (2000) Non-Transferrin-Bound Iron is Present in Serum of Hereditary Haemochromatosis Heterozygotes, *Eur. J. Clin. Inv. 30*, 248-251.

166. SanMartín, C., Paula-Lima, A., Hidalgo, C., and Núñez, M. (2012) Sub-Lethal Levels of Amyloid β-Peptide Oligomers Decrease Non-Transferrin-Bound Iron Uptake and do not Potentiate Iron Toxicity in Primary Hippocampal Neurons, *BioMetals 4,* 805-813.

167. Baker, E., Baker, S. M., and Morgan, E. H. (1998) Characterisation of Non-Transferrin-Bound Iron (Ferric Citrate) Uptake by Rat Hepatocytes in Culture, *Biochim Biophys Acta 1380*, 21-30.

168. Brissot, P., Wright, T. L., Ma, W. L., and Weisiger, R. A. (1985) Efficient Clearance of Non-transferrin-bound Iron by Rat Liver, *J. Clin. Invest. 76*, 1463-1470.

169. Kaplan, J., Jordan, I., and Sturrock, A. (1991) Regulation of the Transferrin-Independent Iron Transport System in Cultured Cells, *J. Biol. Chem. 266*, 2997-3004.

170. Inman, R. S., and Wessling-Resnick, M. (1993) Characterization of Transferrin-Independent Iron Transport in K562 Cells, *J. Biol. Chem. 268*, 8521-8528.

171. Holmes-Hampton, G., Jhurry, N. D., McCormick, S. P., and Lindahl, P. A. (2013) Iron Content of *Saccharomyces cerevisiae* Cells Grown under Iron-Deficient and Iron-Overload Conditions, *Biochemistry 52*, 105-114.

172. Miao, R., Holmes-Hampton, G., and Lindahl, P. A. (2011) Biophysical Investigation of the Iron in Aft1-1up and Gal-YAH1 *Saccharomyces cerevisiae*, *Biochemistry 50*, 2660-2671.

173. Whitnall, M., Rahmanto, Y. S., Huang, M. L. H., Saletta, F., Lok, H. C., Gutiérrez, L., Lázaro, F. J., Fleming, A. J., Pierre, T. G. S., and Mikhael, M. R. (2012) Identification of Nonferritin Mitochondrial Iron Deposits in a Mouse Model of Friedreich Ataxia, *Proc. Natl. Acad. Sci.109*, 20590-20595.

174. Stemmler, T. L., Lesuisse, E., Pain, D., and Dancis, A. (2010) Frataxin and mitochondrial FeS cluster biogenesis, *J. Biol. Chem. 285*, 26737-26743.

175. Larrick, J. W., and Cresswell, P. (1979) Modulation of Cell Surface Iron Transferrin Receptors by Cellular Density and State of Activation, *J Supramol Str 11*, 579-586.

176. Gohil, V. M., Sheth, S. A., Nilsson, R., Wojtovich, A. P., Lee, J. H., Perocchi, F., Chen, W., Clish, C. B., Ayata, C., Brookes, P. S., and Mootha, V. K. (2010) Nutrient-Sensitized Screening for Drugs that Shift Energy Metabolism from Mitochondrial Respiration to Glycolysis, *Nat. Biotechnol. 28*, 249-255.

177. Williams, J. M., Danson, D. P., and Janot, C. (1978) A Mössbauer Determination of the Iron Core Particle Size Distribution in Ferritin, *Phys. Med. Biol. 23*, 835-851.

178. Bovell, E., Buckley, C. E., Chua-anusorn, W., Cookson, D., Kirby, N., Saunders, M., and St. Pierre, T. G. (2009) Dietary Iron-Loaded Rat Liver Haemosiderin and Ferritin: In Situ Measurement of Iron Core Nanoparticle Size and Cluster Structure Using Anomalous Small-Angle X-Ray Scattering, *Phys Med Biol 54*, 1209-1221.

179. Campanella, A., Rovelli, E., Santambrogio, P., Cozzi, A., Taroni, F., and Levi, S. (2009) Mitochondrial Ferritin Limits Oxidative Damage Regulating Mitochondrial Iron Availability: Hypothesis for a Protective Role in Friedreich Ataxia, *Hum. Mol. Genet. 18*, 1-11.

180. Surovstev, I. V., Morgan, J. J., and Lindahl, P. A. (2007) Whole-Cell Modeling Framework in Which Biochemical Dynamics Impact Aspects of Cellular Geometry, *J. Theor. Biol. 244*, 154-166.

181. Seguin, A., Santos, R., Pain, D., Dancis, A., Camadro, J.-M., and Lesuisse, E. (2011) Co-Precipitation of Phosphate and Iron Limits Mitochondrial Phosphate Availability in *Saccharomyces* c*erevisiae* Lacking the Yeast Frataxin Homologue (Yfh1), *J. Biol. Chem. 286*, 6071-6079.

182. Lu, C., and Cortopassi, G. (2007) Frataxin Knockdown Causes Loss of Cytoplasmic Iron-Sulfur Cluster Functions, Redox Alterations and Induction of Heme Transcripts, *Arch Biochem Biophys 457*, 111-122.

183. Nandal, A., Ruiz, J. C., Subramanian, P., Ghimire-Rijal, S., Sinnamon, R. A., Stemmler, T. L., Bruick, R. K., and Philpott, C. C. (2011) Activation of the HIF Prolyl Hydroxylase by the Iron Chaperones PCBP1 and PCBP2, *Cell Metab 14*, 647-657.

184. Rothen, A. (1944) Ferritin and Apoferritin in the Ultracentrifuge, *J. Biol. Chem. 152*, 679-693.

185. Dickson, D. P. E., Reid, N. M. K., Mann, S., Wade, V. J., Ward, R. J., and Peters, T. J. (1988) Mössbauer Spectroscopy, Electron Microscopy and Electron Diffraction Studies of The Iron Cores in Various Human and Animal Haemosiderins, *Biochim Biophys Acta 957*, 81-90.

186. Macara, I. G., Hoy, T. G., and Harrison, P. M. (1972) The Formation of Ferritin from Apoferritin: Kinetics and Mechanism of Iron Uptake, *Biochem. J. 126*, 151-162.

187. Crichton, R. R., and Paques, E. (1977) A Kinetic Study of the Mechanism of Ferritin Formation, *Biochem. Soc. Trans 5*, 1130-1131.

188. St. Pierre, T. G., Tran, K. C., Webb, J., Macey, D. J., Pootrakul, P., and Dickson, D. P. E. (1992) Core Structures of Haemosiderins Deposited in Various Organs in β-thalassemia/Haemoglobin E Disease, *Hyperfine Interact 71*, 1279-1282.

189. Bell, S. H., Weir, M. P., Dickson, D. P. E., Gibson, J. F., Sharp, G. A., and Peters, T. J. (1984) Mössbauer Spectroscopic Studies of Human Haemosiderin and Ferritin, *Biochim Biophys Acta 787*, 227-236.

190. Michel, F. M., Hosein, H.-A., Hausner, D. B., Debnath, S., Parise, J. B., and Strongin, D. R. (2010) Reactivity of Ferritin and the Structure of Ferritin-Derived Ferrihydrite, *Biochim Biophys Acta 1800*, 871-885.

191. Hartwig, A., and Schlepegrell, R. (1995) Induction of Oxidative DNA Damage by Ferric Iron in Mammalian Cells, *Carcinogenesis 16*, 3009-3013.

192. Hartwig, A., Klyszcz-Nasko, H., Schlepegrell, R., and Beyersmann, D. (1993) Cellular Damage by Ferric Nitrilotriacetate and Ferric Citrate in V79 Cells: Interrelationship between Lipid Peroxidation, DNA Strand Breaks and Sister Chromatid Exchanges, *Carcinogenesis 14*, 107-112.

193. Ames, B. N., Shigenaga, M. K., and Hagen, T. M. (1993) Oxidants, Antioxidants, and the Degenerative Diseases of Aging, *Proc. Natl. Acad. Sci. 90*, 7915-7922.

194. Ye, H., and Rouault, T. A. (2010) Human Iron-Sulfur Cluster Assembly, Cellular Iron Homeostasis, and Disease, *Biochemistry 49*, 4945-4956.

195. Lill, R. (2009) Function and biogenesis of iron-sulphur proteins, *Nature 460*, 831-838.

196. Kaplan, C. D., and Kaplan, J. (2009) Iron Acquisition and Transcriptional Regulation, *Chem Rev 109*, 4536-4552.

197. Jacobs, A. (1977) Low Molecular Weight Intracellular Iron Transport Compounds, *Blood 50*, 433-439.

198. Casas, C., Aldea, M., Espinet, C., Gallego, C., Gil, R., and Herrero, E. (1997) The AFT1 Transcriptional Factor is Differentially Required for Expression of

High-Affinity Iron Uptake Genes in *Saccharomyces cerevisiae*, *Yeast 13*, 621-637.

199. Rutherford, J. C., Jaron, S., and Winge, D. R. (2003) Aft1p and Aft2p Mediate Iron-Responsive Gene Expression in Yeast through Related Promoter Elements, *J. Biol. Chem. 278*, 27636-27643.

200. Philpott, C. C. (2006) Iron Uptake in Fungi: A System for Every Source, *BBA-Mol Cell Res 1763*, 636-645.

201. Davis-Kaplan, S. R., Ward, D. M., Shiflett, S. L., and Kaplan, J. (2004) Genome-wide Analysis of Iron-dependent Growth Reveals a Novel Yeast Gene Required for Vacuolar Acidification, *J. Biol. Chem. 279*, 4322-4329.

202. Eide, D., Daviskaplan, S., Jordan, I., Sipe, D., and Kaplan, J. (1992) Regulation of Iron Uptake in Saccharomyces-Cerevisiae - the Ferrireductase and Fe(II) Transporter Are Regulated Independently, *J. Biol. Chem. 267*, 20774-20781.

203. Yamaguchi-Iwai, Y., Stearman, R., Dancis, A., and Klausner, R. D. (1996) Iron-Regulated DNA Binding by the AFT1 Protein Controls the Iron Regulon in Yeast, *EMBO J. 15*, 3377-3384.

204. Courel, M., Lallet, S., Camadro, J. M., and Blaiseau, P. L. (2005) Direct Activation of Genes Involved in Intracellular Iron Use by the Yeast Iron-Responsive Transcription Factor Aft2 without its Paralog Aft1, *Mol. Cell. Biol. 25*, 6760-6771.

205. Dancis, A., Roman, D. G., Anderson, G. J., Hinnebusch, A. G., and Klausner, R. D. (1992) Ferric Reductase of *Saccharomyces cerevisiae* - Molecular

Characterization, Role in Iron Uptake, and Transcriptional Control by Iron, *Proc Natl Acad Sci USA 89*, 3869-3873.

206. Dix, D., Bridgham, J., Broderius, M., and Eide, D. (1997) Characterization of the FET4 Protein of Yeast - Evidence for a Direct Role in the Transport of Iron, *J. Biol. Chem. 272*, 11770-11777.

207. Askwith, C., Eide, D., Van Ho, A., Bernard, P. S., Li, L., Davis-Kaplan, S., Sipe, D. M., and Kaplan, J. (1994) The FET3 Gene of *S. cerevisiae* Encodes a Multicopper Oxidase Required for Ferrous Iron Uptake, *Cell 76*, 403-410.

208. Desilva, D. M., Askwith, C. C., Eide, D., and Kaplan, J. (1995) The Fet3 Gene-Product Required for High-Affinity Iron Transport in Yeast is a Cell-Surface Ferroxidase, *J. Biol. Chem. 270*, 1098-1101.

209. Puig, S., Vergara, S. V., and Thiele, D. J. (2008) Cooperation of Two mRNA-Binding Proteins Drives Metabolic Adaptation to Iron Deficiency, *Cell Metab 7*, 555-564.

210. Chen, X.-Z., Peng, J.-B., Cohen, A., Nelson, H., Nelson, N., and Hediger, M. A. (1999) Yeast SMF1 Mediates H+-coupled Iron Uptake with Concomitant Uncoupled Cation Currents, *J. Biol. Chem. 274*, 35089-35094.

211. Hassett, R., Dix, D. R., Eide, D. J., and Kosman, D. J. (2000) The Fe(II) Permease Fet4p Functions as a Low Affinity Copper Transporter and Supports Normal Copper Trafficking in *Saccharomyces Cerevisiae*, *Biochem. J. 351 Pt 2*, 477-484.

212. Dix, D. R., Bridgham, J. T., Broderius, M. A., Byersdorfer, C. A., and Eide, D. J. (1994) The FET4 Gene Encodes the Low Affinity Fe (II) Transport Protein of *Saccharomyces Cerevisiae*, *J. Biol. Chem. 269*, 26092-26099.

213. Li, L., Bagley, D., Ward, D. A., and Kaplan, J. (2008) Yap5 is an Iron-Responsive Transcriptional Activator that Regulates Vacuolar Iron Storage in Yeast, *Mol. Cell. Biol. 28*, 1326-1337.

214. Li, L., Chen, O. S., Ward, D. M. V., and Kaplan, J. (2001) CCC1 is a Transporter that Mediates Vacuolar Iron Storage in Yeast, *J. Biol. Chem. 276*, 29515-29519.

215. Nishida, K., and Silver, P. A. (2012) Induction of Biogenic Magnetization and Redox Control by a Component of the Target of Rapamycin Complex 1 Signaling Pathway, *PLoS Biol 10*, 1-10.

216. Urbanowski, J. L., and Piper, R. C. (1999) The Iron Transporter Fth1p Forms a Complex with the Fet5 Iron Oxidase and Resides on the Vacuolar Membrane, *J. Biol. Chem. 274*, 38061-38070.

217. Portnoy, M. E., Liu, X. F., and Culotta, V. C. (2000) *Saccharomyces cerevisiae* Expresses Three Functionally Distinct Homologues of the Nramp Family of Metal Transporters, *Mol. Cell. Biol. 20*, 7893-7902.

218. Li, L. T., and Kaplan, J. (2004) A Mitochondrial-Vacuolar Signaling Pathway in Yeast that Affects Iron and Copper Metabolism, *J. Biol. Chem. 279*, 33653-33661.

219. Mühlenhoff, U., Stadler, J. A., Richhardt, N., Seubert, A., Eickhorst, T., Schweyen, R. J., Lill, R., and Wiesenberger, G. (2003) A Specific Role of the

Yeast Mitochondrial Carriers Mrs3/4p in Mitochondrial Iron Acquisition under Iron-Limiting Conditions, *J. Biol. Chem. 278*, 40612-40620.

220. Froschauer, E. M., Schweyen, R. J., and Wiesenberger, G. (2009) The Yeast Mitochondrial Carrier Proteins Mrs3p/Mrs4p Mediate Iron Transport across the Inner Mitochondrial Membrane, *BBA-Biomembranes 1788*, 1044-1050.

221. Foury, F., and Roganti, T. (2002) Deletion of The Mitochondrial Carrier Genes Mrs3 and Mrs4 Suppresses Mitochondrial Iron Accumulation in a Yeast Frataxin-Deficient Strain, *J. Biol. Chem. 277*, 24475-24483.

222. Jo, W. J., Loguinov, A., Chang, M., Wintz, H., Nislow, C., Arkin, A. P., Giaever, G., and Vulpe, C. D. (2008) Identification of Genes Involved in the Toxic Response of Saccharomyces Cerevisiae against Iron and Copper Overload by Parallel Analysis of Deletion Mutants *Toxicol. Sci. 102*, 205-205.

223. Kucej, M., and Foury, F. (2003) Iron Toxicity Protection by Truncated Ras2 GTPase in Yeast Strain Lacking Frataxin, *Biochem. Biophys. Res. Commun. 310*, 986-991.

224. Lee, A., Henras, A. K., and Chanfreau, G. (2005) Multiple RNA Surveillance Pathways Limit Aberrant Expression of Iron Uptake mRNAs and Prevent Iron Toxicity in *S. cerevisiae*, *Mol. Cell 19*, 39-51.

225. Bleackley, M. R., Young, B. P., Loewen, C. J. R., and MacGillivray, R. T. A. (2011) High Density Array Screening to Identify the Genetic Requirements for Transition Metal Tolerance In *Saccharomyces cerevisiae*, *Metallomics 3*, 195-205.

226. Peiter, E., Fischer, M., Sidaway, K., Roberts, S. K., and Sanders, D. (2005) The *Saccharomyces cerevisiae* Ca2+ Channel Cch1Pmid1P is Essential for Tolerance to Cold Stress and Iron Toxicity, *FEBS Lett. 579*, 5697-5703.

227. Holmes-Hampton, G. P., Chakrabarti, M., Cockrell, A. L., McCormick, S. P., Abbott, L. C., Lindahl, L. S., and Lindahl, P. A. (2012) Changing Iron Content of the Mouse Brain During Development, *Metallomics 8*, 761-770.

228. Felice, M. R., De Domenico, I., Li, L. T., Ward, D. M., Bartok, B., Musci, G., and Kaplan, J. (2005) Post-Transcriptional Regulation of the Yeast High Affinity Iron Transport System, *J. Biol. Chem. 280*, 22181-22190.

229. Thomas, B. J., and Rothstein, R. (1989) Elevated Recombination Rates in Transcriptionally Active DNA, *Cell 56*, 619-630.

230. Lindahl, P. A., Morales, J. G., Miao, R., and Holmes-Hampton, G. (2009) Isolation of Saccharomyces Cerevisiae Mitochondria for Mössbauer, EPR, and Electronic Absorption Spectroscopic Analyses, *Method Enzymol 456*, 267-285.

231. Aasa, R., Albracht, S. P. J., Falk, K.-E., Lanne, B., and Vänngård, T. (1976) EPR Signals from Cytochrome *c* Oxidase, *BBA - Enzymol 422*, 260-272.

232. Fee, J. A., Findling, K. L., Yoshida, T., Hille, R., Tarr, G. E., Hearshen, D. O., Dunham, W. R., Day, E. P., Kent, T. A., and Munck, E. (1984) Purification and Characterization of the Rieske Iron-Sulfur Protein from *Thermus thermophilus.* Evidence for a [2Fe-2S] Cluster Having Non-cysteine Ligands, *J. Biol. Chem. 259*, 124-133.

233. Stevens, B. J. (1977) Variation in Number and Volume of Mitochondria in Yeast According to Growth-Conditions - Study Based on Serial Sectioning and Computer Graphics Reconstitution, *Biologie Cellulaire 28*, 37-56.

234. Yamaguchi-Iwai, Y., Dancis, A., and Klausner, R. D. (1995) AFT1: A Mediator of Iron Regulated Transcriptional Control in *Saccharomyces cerevisiae*, *EMBO J 14*, 1231-1239.

235. Puig, S., Askeland, E., and Thiele, D. J. (2005) Coordinated Remodeling of Cellular Metabolism furing Iron Deficiency through Targeted mRNA Degradation, *Cell 120*, 99-110.

236. Chang, E. C., and Kosman, D. J. (1989) Intracellular Mn (II)-Associated Superoxide Scavenging Activity Protects Cu,Zn Superoxide Dismutase-Deficient *Saccharomyces cerevisiae* against Dioxygen Stress, *J Biol Chem 264*, 12172-12178.

237. McNaughton, R. L., Reddi, A. R., Clement, M. H. S., Sharma, A., Barnese, K., Rosenfeld, L., Gralla, E. B., Valentine, J. S., Culotta, V. C., and Hoffman, B. M. (2010) Probing *in vivo* Mn2+ Speciation and Oxidative Stress Resistance in Yeast Cells with Electron-Nuclear Double Resonance Spectroscopy, *Proc Natl Acad Sci USA 107*, 15335-15339.

238. McCormick, S. P., Chakrabarti, M., Cockrell, A. L., Park, J., Lindahl, L. S., and Lindahl, P. A. (2013) Low-Molecular-Mass Metal Complexes in the Mouse Brain, *Metallomics 5*, 232-241.

239. Kurz, T., Terman, A., Gustafsson, B., and Brunk, U. T. (2008) Lysosomes in Iron Metabolism, Ageing and Apoptosis, *Histochem. Cell. Biol. 129*, 389-406.

240. Giannetti, A. M., and Bjorkman, P. J. (2004) HFE and Transferrin Directly Compete for Transferrin Receptor in Solution and at the Cell Surface, *J. Biol. Chem. 279*, 25866-25875.

APPENDIX I

Table A1. Batches of cells analyzed.

Batch	Packing Expt.	Mössbauer Spectroscopy	EPR Spectroscopy	UV-Vis Spectroscopy	ICP-MS
C01-C05	*Whole cells in from C01-C05 were used solely for mitochondria isolation and Western Blot analysis for purity*				
C06	Yes	Weak	Table 2-1	-	Table A4
C07	-	Figure 2-3A, 2-3B, and 2-3C	Table 2-1	-	Table A4
C08	Yes	-	-	-	Table A4
C09	-	-	-	Table 2-1	-
C10	-	-	-	Figure 2-5C and 2-5D	-
C11	-	-	Figure 2-4A and 2-4B	-	Table A4
C12	-	-	-	Table 2-1	-
C13	-	Figure A1A and A1B	Table 2-1	Table 2-1	-
C14	Table A3	-	-	-	Table A4

Table A2. Batches of mitochondria analyzed

Batch	Cell batch used	Western Blot	EM	Packing Expt.	Mössbauer Spectroscopy	EPR	UV-Vis	ICP-MS
M01	C01	Yes	-	-	-	Table 2-1	Table 2-1	-
M02	C02	Yes	Yes	-	-	-	-	Table A4
M03	C06	Figure 2-1	Yes	-	Figure A1D	-	Table 2-1	-
M04	C08	-	-	-	Figure 2-2A, 2-2B, 2-2C	-	-	-
M05	C09	-	-	Yes	-	Figure 4C	Table 2-1	Table A4
M06	C10	-	Figure 2-1	Yes	Table 2-1	Figure 4A and 4B	Figure 2-5A and 2-5B	Table A4
M07	C11	-	-	Yes	-	Table 2-1	Table 2-1	Table A4
M08	C13	-	-	-	Figure A1C	Table 2-1	-	-
M09	C14	-	-	Table A3	-	-	-	Table A4

Table A3. Volumes of pellets of whole cells and isolated mitochondria determined from packing experiments and calculated packing efficiencies.

Sample (Run)	$C_{sup1,2}$ (μM)	$V_{sup1,2}$ (μL)	$V_{int1,2}$ (μL)	$V_{pellet\ 1,2}$ (μL)	Packing efficiency (%)
Whole cells					
C14.1 (1)	82	200	43	250	83
C14.1 (2)	18	200	57	250	77
C14.2 (1)	91	200	18	250	93
C14.2 (2)	20	210	59	225	74
C14.3 (1)	84	200	38	250	85
C14.3 (2)	19	210	61	250	76
C14.4 (1)	77	200	59	300	80
C14.4 (2)	15	200	48	275	83
Mean packing efficiency of whole cells					**81±6**
Mitochondria					
M09.1 (1)	65	151	80	175	55
M09.1 (2)	10	143	26	100	74
M09.2 (1)	67	151	73	150	51
M09.2 (2)	12	140	31	100	69
M09.3 (1)	76	149	48	150	68
M09.3 (2)	13	150	31	100	69
M09.4 (1)	64	149	85	175	51
M09.4 (2)	10	140	26	100	74
M09.5 (1)	64	200	112	225	50
M09.5 (2)	12	195	45	175	74
M09.6 (1)	82	195	45	200	77
M09.6 (2)	14	210	43	150	72
Mean packing efficiency of mitochondria					**65±10**

$V_{buffer1,2}$ for whole cell samples W, X, Y, and Z = 200 μL

$V_{buffer1,2}$ for mitochondria samples A, B, C and D = 150 μL

$V_{buffer1,2}$ for mitochondria samples E and F = 200 μL

Table A4. Metal concentrations from each batch

	[Fe] (μM)	[Cu] (μM)	[Mn] (μM)	[Zn] (μM)
Whole cell batch				
C06	336	22	6.7	323
C06	346	25	7.0	353
C07	341	25	7.4	385
C07	385	29	7.4	384
C08	469	30	7.4	574
C08	509	36	6.8	617
C11	447	33	7.4	665
C11	468	29	6.7	555
C14	325	27	8.6	630
Average ± SD	402 ±70	28±4	7.2±0.6	498±135
Mitochondria batch				
M02	1140	112	17	72
M05	1160	115	17	57
M06	1210	129	11	245
M07	1130	112	11	232
M09	960	108	16	227
Average ± SD	1120±95	115±8	14±3	167±94

Table A5. Analytical properties of isolated mitochondria from Jurkat cells. Replicates *n* are given in parentheses. Mössbauer percentages are denoted followed by absolute concentrations in μM.

Name	Total Fe [Fe_{cell}] (*n*)	NHHS Fe^{II} (%,μM)	Fe/S+LS Hemes (%,μM)	Ferritin-like (%,μM)	HS Fe^{II} hemes (%,μM)	Nano-particles (%,μM)
3FU, WT	282 ± 20 (*2*)	10,28	70,198	20,56	10,28	10,28
30FU, WT	1060±37 (*2*)	2,21	27,286	4,42	2,21	65,689
3TU, WT	296±50 (*1*)	---,---	70,207	20,60	---,---	10,30

Table A6. Concentrations of reduced hemes *a*, *b*, and *c* in Jurkat cells grown under various conditions and isolated mitochondria. Nomenclature is the same as described in the Table 3-1 legend. Concentrations are given in μM.

Growth conditions	[heme a]	[heme b]	[heme c]
	WHOLE CELLS		
3 FU, WT	8±1	5±2	12±2
30 FU, WT	7±1	5±2	14±2
100 FU, WT	4±1	4±1	10±2
3 FL, WT	5±1	5±1	13±2
10 FL, WT	8±2	5±2	10±2
30 FL, WT	4±1	4±1	10±2
3 TU, WT	5±1	6±2	12±2
3 TU, $TfRC^{+}$	6±1	6±2	12±2
	MITOCHONDRIA		
3 FU, WT	32±6	14±4	40±10
30 FU, WT	34±8	19±5	44±11
3 TU, WT	27±7	14±4	40±10

APPENDIX II

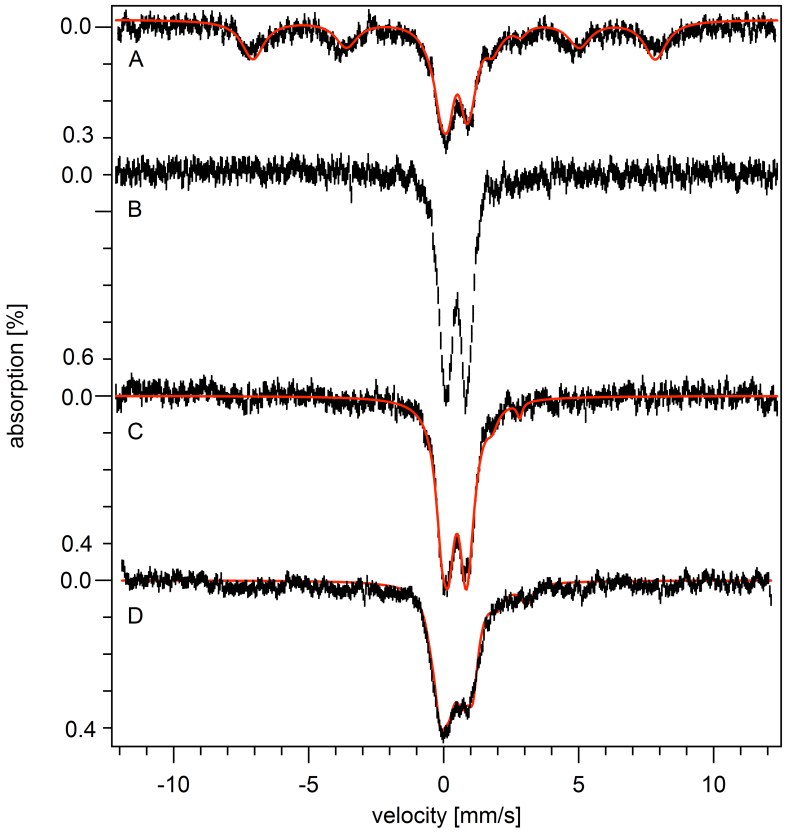

Figure A1. Low field (0.05 T) Mössbauer spectra of other batches. A, 5 K spectrum of whole cells, batch C13 (Table S1), with simulation in red (11% NHHS Fe^{II}, 28% CD, 3% HS Fe^{II} Hemes, 18% Fe^{III} oxyhydroxide nanoparticles, 40% ferritin). B, 70 K spectrum of the same batch of cells. C, 5 K spectrum of isolated mitochondria, batch M08 (Table S2), with simulation in red (7% NHHS Fe^{II}, 27% CD, 5% HS Fe^{II} Hemes, 40% Fe^{III} oxyhydroxide nanoparticles, 19% ferritin-like). D, 5 K spectrum of isolated mitochondria, batch M03 (Table S2), with simulation in red (9% NHHS Fe^{II}, 29% CD, 5% HS Fe^{II} Hemes, 37% Fe^{III} oxyhydroxide nanoparticles, 18% ferritin-like). For all spectra, the field was applied parallel to the radiation.

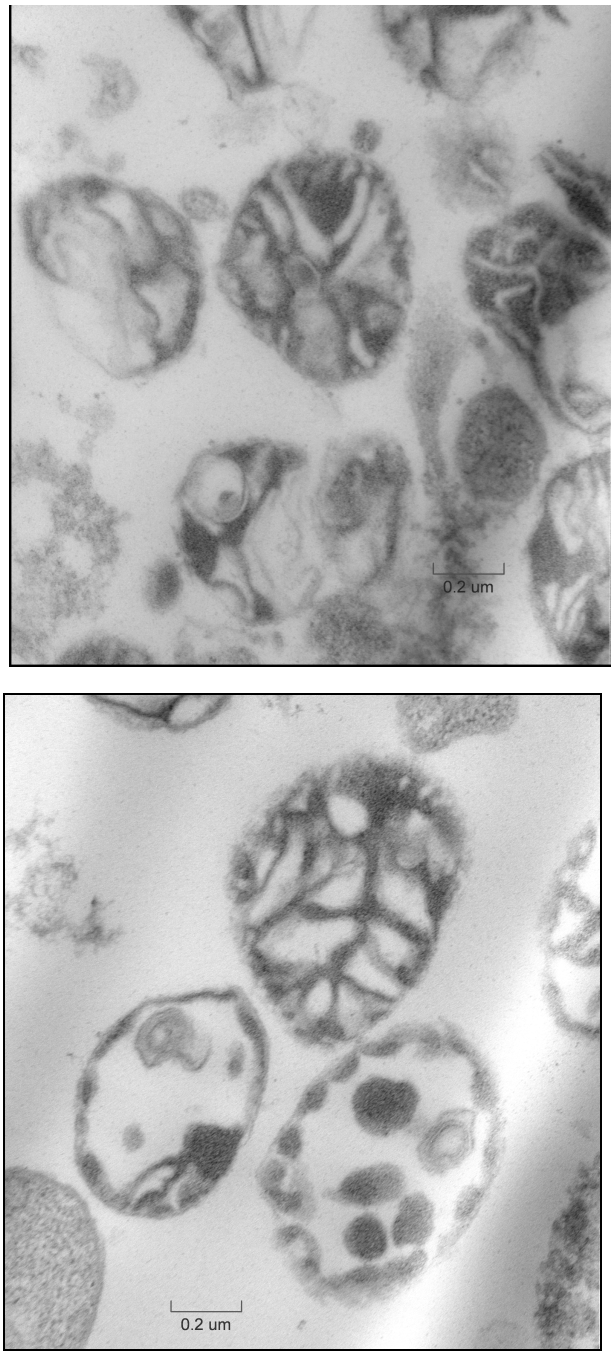

Figure A2. Additional electron micrographs of isolated mitochondria (X 40 000)

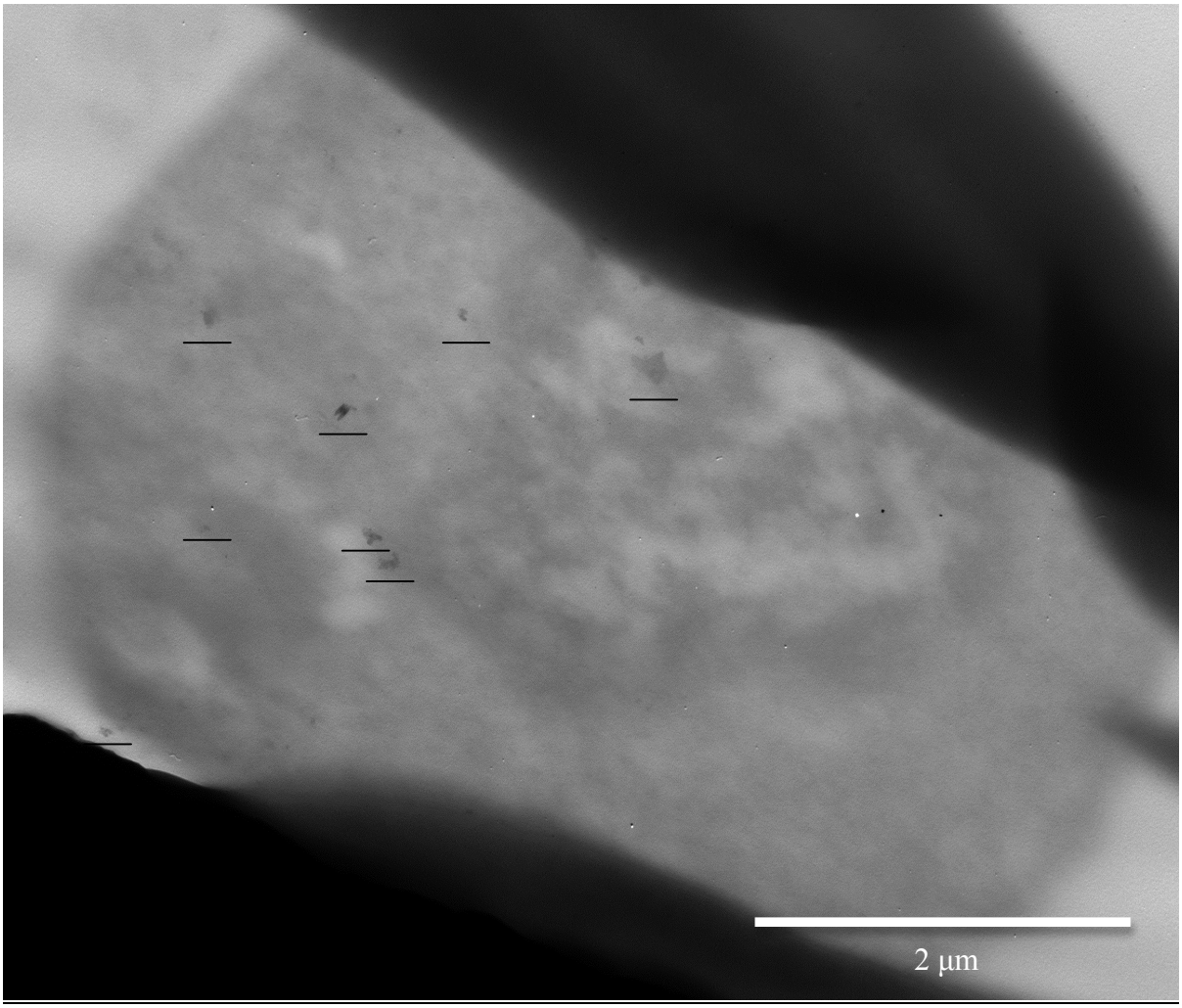

Figure A3. TEM image of Jurkat cell grown with 30 μM FC. Horizontal lines denote ferric nanoparticles.

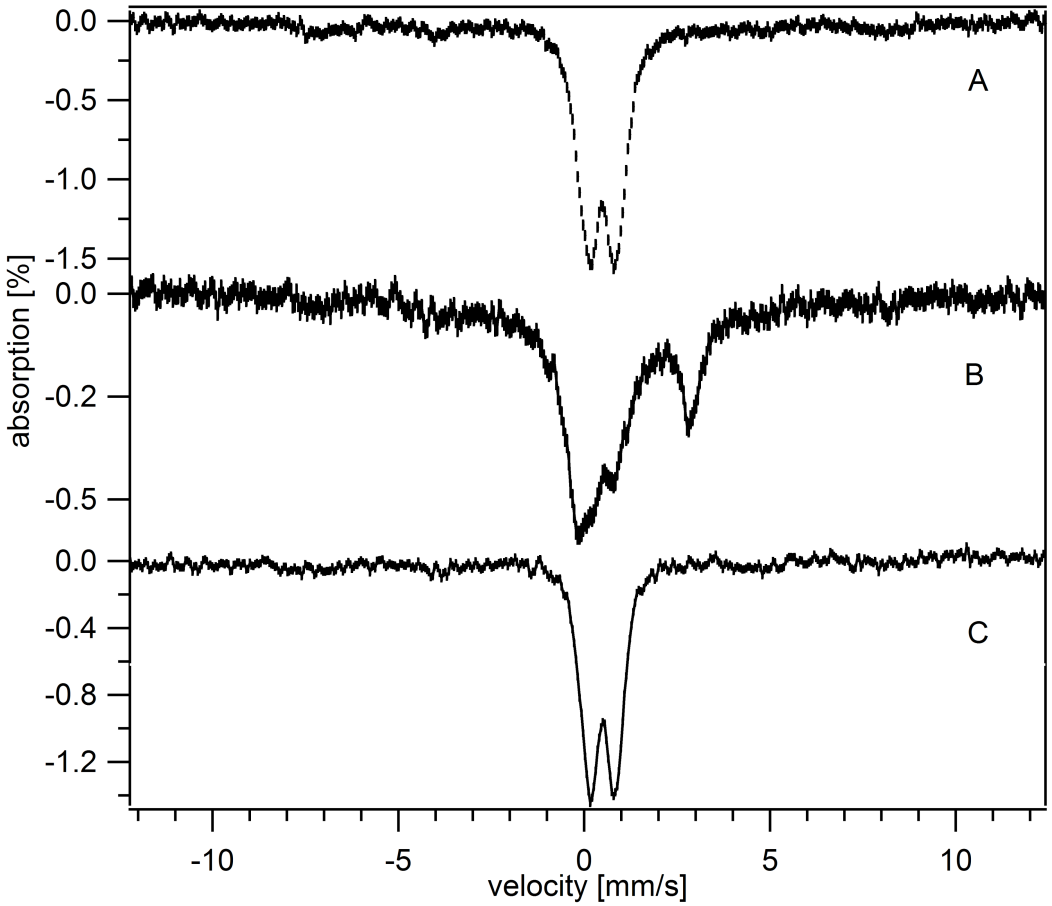

Figure A4. Test to distinguish low-loaded ferritin from nanoparticles. Mössbauer spectra of cells grown under 30 μM Ferric citrate. A. 5K, 0.05T spectrum. B. 5K, 0.05T spectrum of cell lysate after incubation with 6.25 mM ^{56}Ferrous sulfate in air. C. 5K, 0.05T of control cell lysate incubated in air without addition of ferrous sulfate.

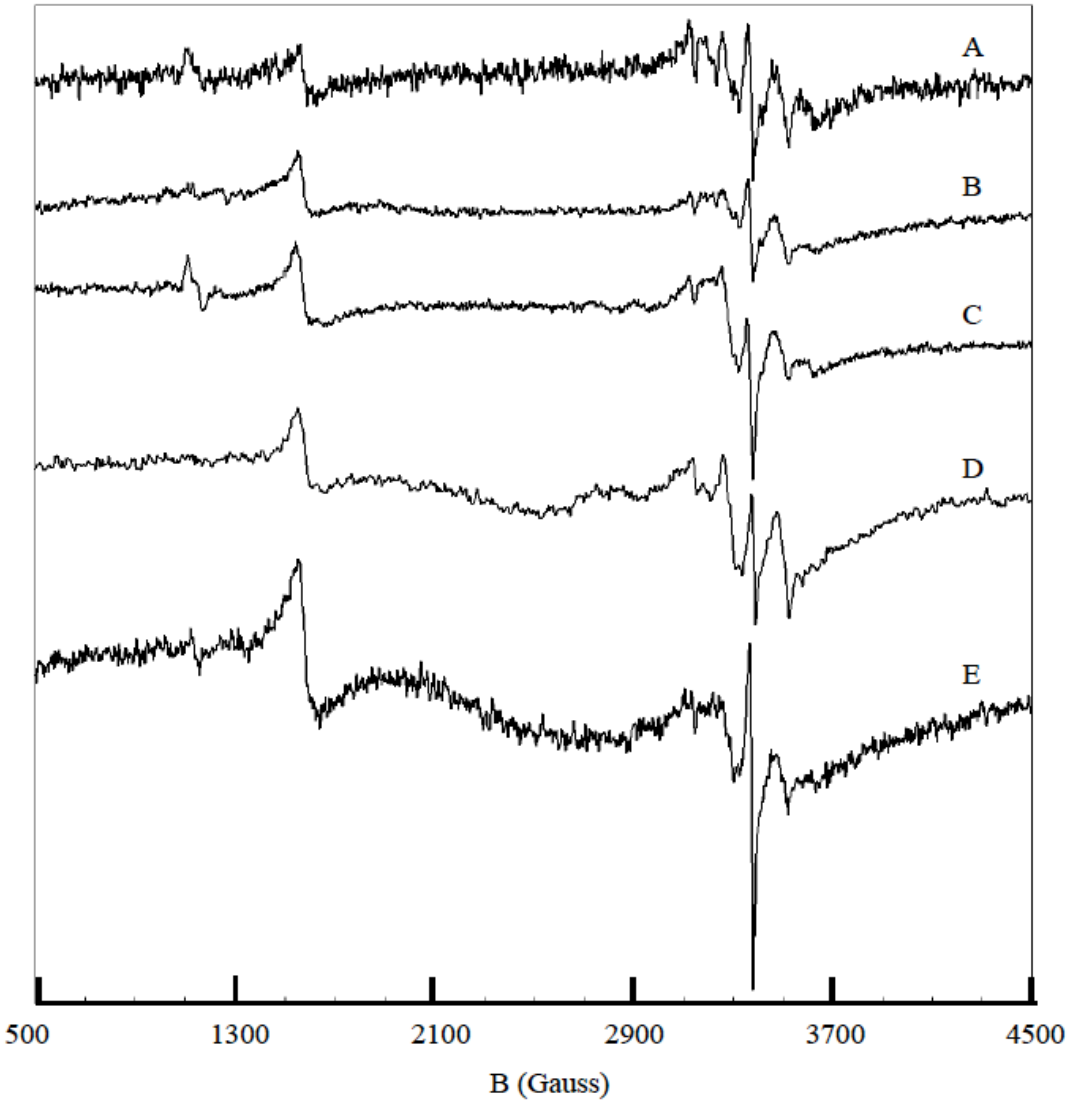

Figure A5. X-band EPR spectra of Jurkat cells. A, 3FU; B, 30FU; C, 3TU; D, 3TU $TfRC^{+}$ cells; E. 10FL. Spectra A-C and E were collected at frequency of 9.473 GHz. Spectrum D was collected at frequency of 9.642 GHz and normalized to 9.473 GHz. Temperature = 4 K, power = 0.2012 mW, modulation amplitude = 10 G, modulation frequency = 100 kHz, conversion time = 164 ms, and sweep time = 336 s.

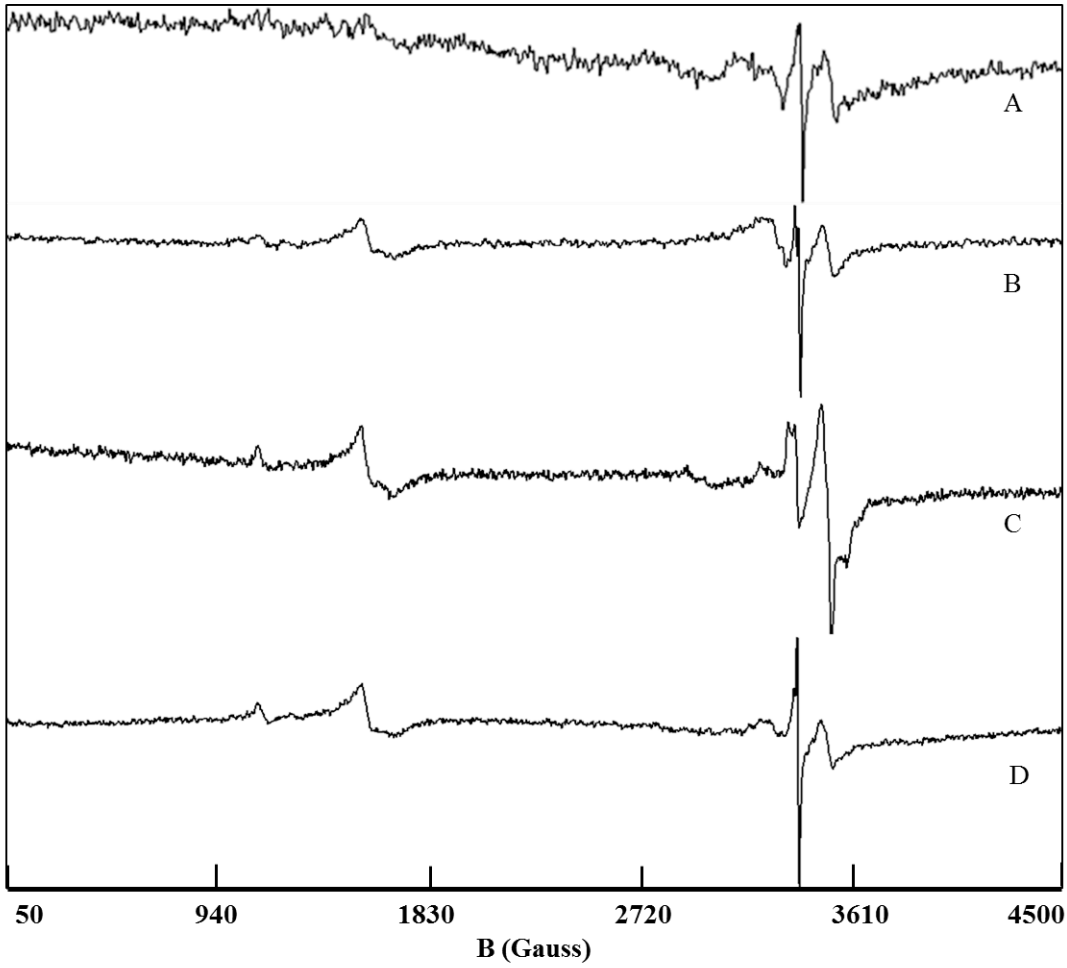

Figure A6. EPR spectra of isolated mitochondria from Jurkat cells. A, 3TU; B, 3FU; C, 10FU; and D, 30FU. Spectrum A was collected at frequency of 9.642 GHz and normalized to 9.473 GHz. Spectra B-D were collected at frequency of 9.473 GHz. Temperature = 4 K, power = 0.2012 mW, modulation amplitude = 10 G, modulation frequency=100 kHz, conversion time= 164 ms, and sweep time= 336 s.

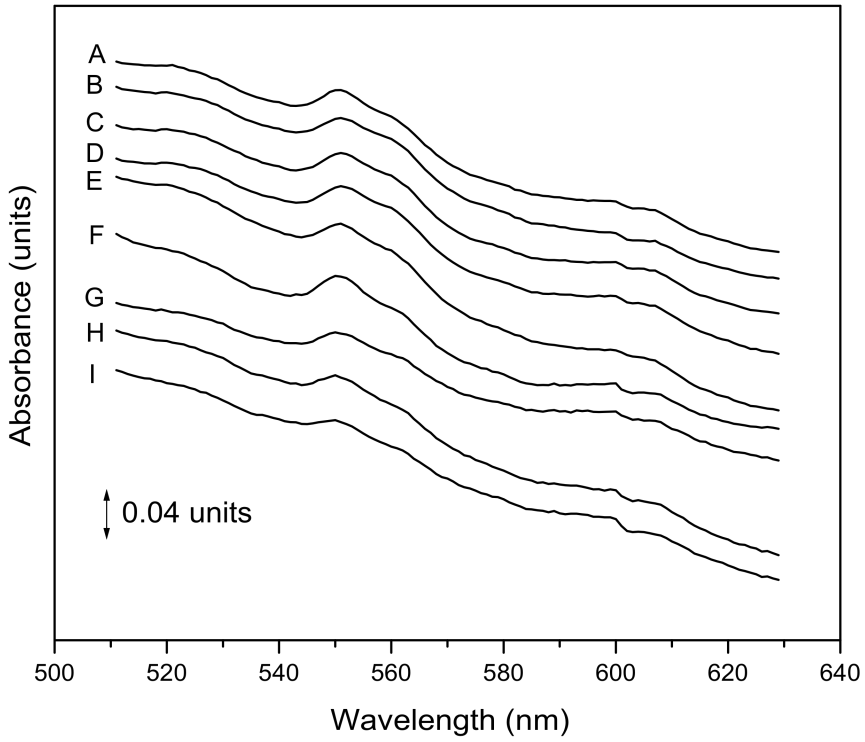

Figure A7. UV-Visible spectra of whole Jurkat cells. A, 3TU; B, 3TU $TfRC^{+}$ cells; C, 3FU; D, 10FU; E, 30FU; F, 100FU; G, 3FL; H, 10FL; I, 30FL.

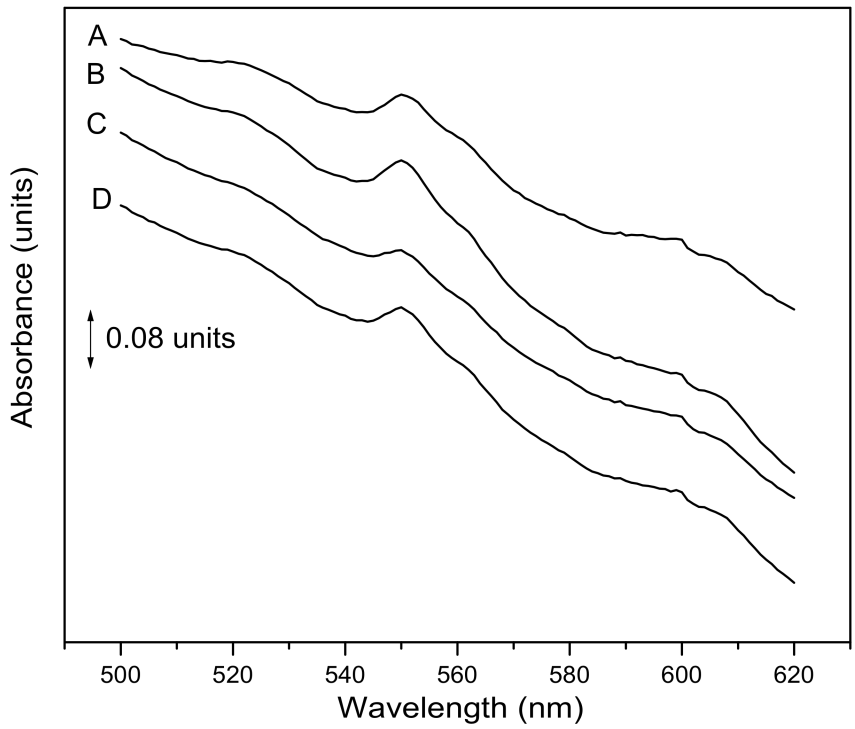

Figure A8. UV-Visible spectra of mitochondria isolated from Jurkat cells. A, 3TU; B, 3FU; C, 10FU; D, 30FU. Mitochondrial samples for UV-Vis were prepared anaerobically.

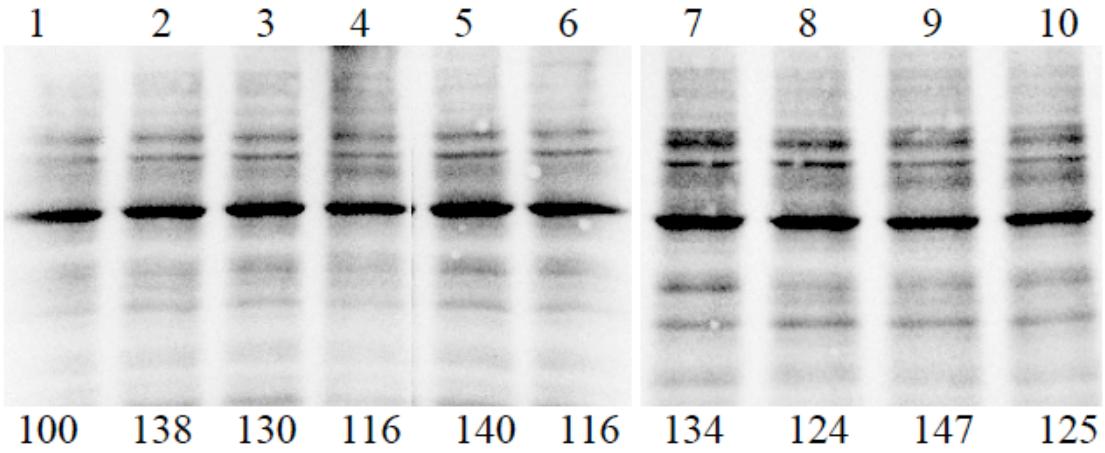

Figure A9. Oxyblot analysis of cells grown under different conditions. Samples include (with lanes in parentheses) (1) 3TU; (2) 10TU; (3) 30 TU; (4) 3TU TfRC^{+}'; (5) 10TU TfRC^{+}; (6) 30TU TfRC^{+}; (7) 3FU; (8) 10FU; (9) 30FU; and (10) 100FU. Percentages of band intensities relative to the standard (Lane 1) are designated below each lane. Twenty μg of protein was loaded per lane on a 12% polyacrylamide gel, and SDS-PAGE was carried out at 100 V.

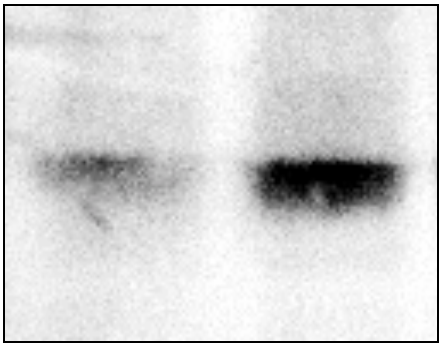

1 2

Figure A10. Western blot indicating overexpression of TfRC in genetically modified Jurkat cells. Lanes: 1. Normal cells, 2. $TfRC^{+}$ cells. Amount of protein loaded per lane = 60 μg.

1 2

Figure A11. Western blot indicating partial knockdown of frataxin protein in genetically modified Jurkat cells. Lanes: 1. Normal cells, 2. Frataxin-deficient cells. Amount of protein loaded per lane = 50 μg.

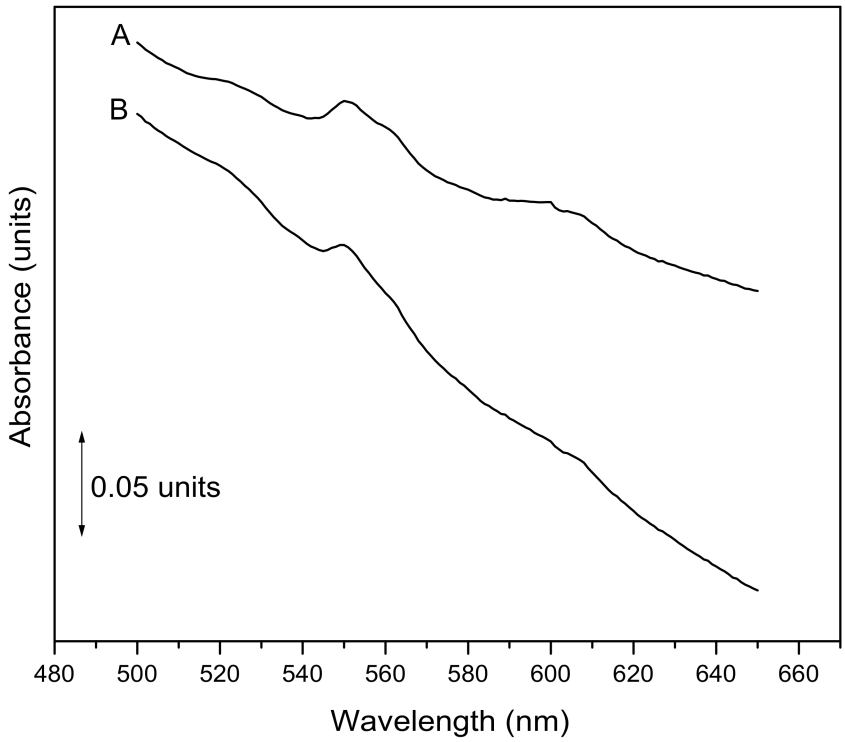

Figure A12. UV-Vis spectra of A. normal cells, and B. frataxin-deficient cells grown with 10 μM FC.

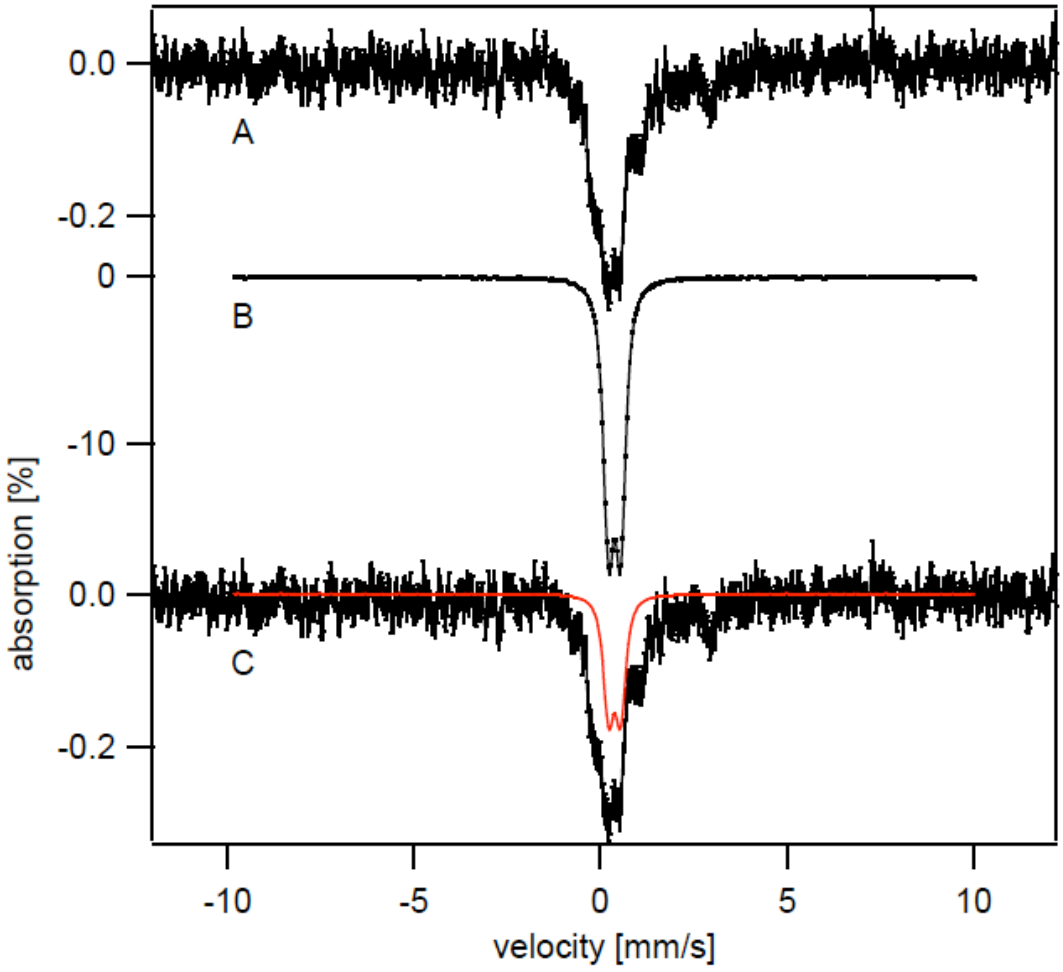

Figure A13. Mössbauer spectra (5K, 0.05T) showing the contribution of BPS in Fe-deficient fermenting cells. A, BPS-F cells; B, $[Fe^{2+}(BPS)_3]^{4-}$; C, overlay of A and B at 35% intensity.

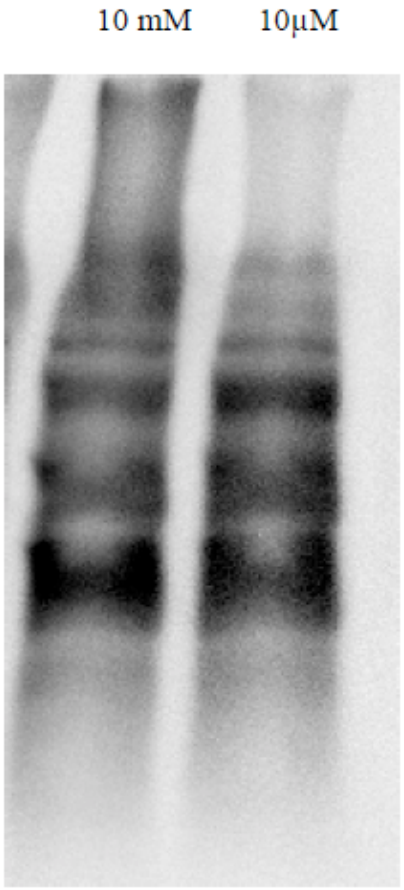

Figure A14. Oxyblot analysis of mitochondria isolated from WT fermenting yeast grown with 10 μM and 10,000 μM of Fe in the medium. Each lane contains 20 μg of protein.

APPENDIX III

NOMENCLATURE

BPS	Bathophenanthroline Sulfonate
CD	Central Quadrupole Doublet
DFO	Desferrioxamine
DDDI	Double-Distilled and Deionized
DMT1	Divalent Metal Transporter 1
δ	Isomer Shift
ΔE_Q	Quadruple Splitting
DT	Doubling Time
ECAR	Extracellular Acidification Rate
EDTA	Ethylenediaminetetraacetic Acid
EDX	Energy Dispersive X-ray
EM	Electron Microscopy
EPR	Electron Paramagnetic Resonance
FC	Ferric Citrate
Fe_{cell}	Overall Cellular Fe
Fe_c	Cytosolic Fe
Fe_f	Ferritin-bound Fe
Fe_m	Mitochondrial Fe, except for Fe found as nanoparticles

Fe_{mp}	Nanoparticles found in mitochondria
Fe_n	Cytosolic Nanoparticles Fe
Fe_s	Sensed Fe
HAADF	High-Angle-Annular-Dark-Field
HS	High Spin
ICP-MS	Inductively Coupled Plasma Mass Spectrometry
IRP1, IRP2	Iron Responsive Element binding proteins 1 and 2
LIP	Labile Iron Pool
LS	Low-Spin
MB	Mössbauer
NHHS	Non-Heme High Spin
NTBI	Non-Transferrin-Bound Iron
OCR	Oxygen Consumption Rate
ODE	Ordinary Differential Equation
PBS	Phosphate-Buffered Saline
RCI-RCIV	Mitochondrial Respiratory Complexes I-IV
Reg_-	Surrogate for regulation in which increasing Fe_s inhibits
Reg_+	Surrogate for regulation in which decreasing Fe_s stimulates
ROS	Reactive Oxygen Species
STEM	Scanning Tunneling Electron Microscopy
TBI	Transferrin-Bound Iron
TfRC1	Transferrin Receptor 1

$TfRC^{+}$	Cells genetically modified to overexpress TfRC1
TMG	Trace Metal Grade
UTR	Untranslated Region
UV-vis	Electronic Absorption Spectroscopy